WARSAW UNIVERSITY OF TECHNOLOGY

FACULTY OF PHYSICS

Ph.D. Thesis

Angelika Magdalena Tefelska, M.Sc.

$K^{*}(892)^{0}$ meson production in p+p collisions at the CERN SPS energies

Supervisor
Katarzyna Grebieszkow, Ph.D., D.Sc.

Co-supervisor
Marcin Słodkowski, Ph.D.

WARSAW 2020

For my husband

Acknowledgements

I would like to thank people who supported me and gave the opportunity to finish this thesis, especially:

Katarzyna Grebieszkow and Marek Gaździcki for opportunity to participate in the NA61/SHINE experiment and realize the $K^*(892)^0$ analysis.

Peter Seyboth, Katarzyna Grebieszkow, Marek Gaździcki, Marcin Słodkowski, Herbert Ströbele, Tatjana Šuša, Joanna Stepaniak and Antoni Marcinek for comments and suggestions during the online meetings to improve the results presented in this thesis.

Katarzyna Grebieszkow, Marek Gaździcki, Peter Seyboth, Joanna Stepaniak, Boris Popov, Szymon Puławski, Michael Unger for excellent common work during the Editorial Board meetings on the prepared NA61/SHINE paper, based on $K^*(892)^0$ results for p+p at 158 GeV/c, presented in this thesis.

Katarzyna Grebieszkow, Marcin Słodkowski, Maja Maćkowiak-Pawłowska, Tobiasz Czopowicz, Bartosz Maksiak, Viktor Begun, Justyna Cybowska and Wojciech Bryliński for a great atmosphere in the university office during realization of this work.

My husband Dariusz Tefelski and family for supporting and motivating me to finish this thesis.

This work was supported by the National Science Centre Poland (2017/25/N/ST2/02575).

Streszczenie

W niniejszej pracy doktorskiej przedstawiono pomiary mezonu $K^*(892)^0$ korzystając z kanału rozpadu $K^+\pi^-$ dla zderzeń p+p przy pędach wiązek 40–158 GeV/c. Dane zostały zebrane przez eksperyment NA61/SHINE zlokalizowany przy akceleratorze *Super Proton Synchrotron* w CERN. Po raz pierwszy sygnał $K^*(892)^0$ został wyznaczony z wykorzystaniem metody szablonów. Metoda ta została opracowana przez autorkę pracy doktorskiej jako alternatywa do znanej metody tzw. *coctail fit'u*, który nie sprawdza się przy analizie kanału rozpadu innego niż $\pi^+\pi^-$. Mezon $K^*(892)^0$ był badany w kanale rozpadu $K^+\pi^-$ i dlatego modyfikacja metody *coctail fit* była konieczna. W Rozdziale 4 opisano szczegółowo metodę analizy.

Wysoka statystyka danych dla oddziaływań p+p przy 158 GeV/c pozwoliła przygotować podwójnie różniczkowe widma pędu poprzecznego i pośpieszności. Średnia krotność mezonów $K^*(892)^0$ dla 158 GeV/c została obliczona na podstawie scałkowanego po p_T oraz ekstrapolowanego rozkładu pośpieszności. Wartość tę porównano z modelami gazu hadronowego (*Hadron Resonance Gas Models*, HGM), a także z modelem EPOS 1.99. Opublikowane wcześniej pomiary naładowanych kaonów wykorzystano do określenia stosunków krotności $K^*(892)^0$ do $K^\pm$, które pozwalają oszacować przedział czasowy między wymrożeniami chemicznym a kinetycznym. Otrzymaną masę i szerokość piku mezonów $K^*(892)^0$ przedstawiono i porównano z dostępnymi światowymi danymi eksperymentalnymi.

Z powodu mniejszej statystyki danych dla zderzeń p+p przy pędzie wiązki 40 GeV/c i 80 GeV/c, analiza mezonu $K^*(892)^0$ dla tych energii została wykonana tylko w przedziałach pośpieszności, podczas gdy zakres pędu poprzecznego ustalono na $0 < p_T < 1.5$ GeV/c. Ekstrapolowane rozkłady pośpieszności posłużyły do uzyskania średnich krotności mezonów $K^*(892)^0$. Wyniki porównano również z przewidywaniami HGM i EPOS 1.99. Analiza stosunków krotności $K^*(892)^0$ do $K^\pm$ została również przedstawiona dla niższych pędów wiązki. Więcej szczegółów na temat wyników znajduje się w Rozdziale 5.

Słowa kluczowe: produkcja rezonansów, $K^*(892)^0$, czas pomiędzy wymrożeniami, eksperyment NA61/SHINE.

Abstract

This thesis presents $K^*(892)^0$ meson measurements via $K^+\pi^-$ decay channel for p+p interactions at 40–158 GeV/c beam momenta. The data sets were recorded by the NA61/SHINE experiment located at the CERN Super Proton Synchrotron. For the first time, the $K^*(892)^0$ signal was obtained based on the template method. This method was developed by the thesis author as an alternative to the known coctail fit method, which does not work properly for decay channels different than $\pi^+\pi^-$. The $K^*(892)^0$ meson was studied in the $K^+\pi^-$ decay channel and therefore the modification of the coctail fit method was needed. The analysis methodology is described in details in Chapter 4.

The high statistics of data for p+p interactions at 158 GeV/c allowed to prepare the double-differential transverse momentum and rapidity spectra. For 158 GeV/c, the mean multiplicity of $K^*(892)^0$ mesons was calculated based on the p_T-integrated and extrapolated rapidity distribution. This value was compared with the Hadron Resonance Gas Models (HGM) as well as the EPOS 1.99 model. Previously published measurements of charged kaons were used to determine the $K^*(892)^0$ to $K^\pm$ multiplicity ratios, which allow to estimate time interval between chemical and kinetic freeze-outs. The obtained mass and width of $K^*(892)^0$ mesons peak were presented and compared with the available world experimental data.

Due to the lower statistics of 40 GeV/c and 80 GeV/c p+p data, the $K^*(892)^0$ analysis for those two energies was performed in rapidity bins only, whereas the transverse momentum range was fixed on $0 < p_T < 1.5$ GeV/c. The extrapolated rapidity distributions were used to obtain the mean multiplicities of $K^*(892)^0$ mesons. The results were also compared with the HGM and EPOS 1.99 predictions. The analysis of the $K^*(892)^0$ to $K^\pm$ multiplicity ratios was also presented for lower beam momenta. More details about the results are presented in Chapter 5.

Keywords: resonance production, $K^*(892)^0$, time between freeze-outs, NA61/SHINE experiment.

Contents

Chapter 1

Introduction

1.1 Constituents of matter

One of the oldest and still actual questions in nuclear physics is ”What is the matter made of?”. The concept of constituents of matter developed with a new discovery of particles, starting from discovery of electron by J. J. Thomson in 1897 and his model of atom called *The plum pudding model.* This model assumed that electrons are surrounded by positively charged volume [1, 2].

The next was discovery of the components of the nucleus (proton in 1919 and neutron in 1932), which influenced the idea of the new model proposed originally by N. Bohr in 1914. After 1932, only neutrons, protons and electrons were constituents of matter and atom had a simple structure based on positive core, made of protons and neutrons, and negatively charged electrons circling the core. But the next thirty years were dominated by the great ideas: Yukawa's meson, Dirac's positron and Pauli's neutrino, which affected the perception of the structure of matter [1, 2].

The model of atom caused new questions, one of them was ”What holds the nucleus together?”. The positively charged protons should repel each other. The first explanation was proposed by H. Yukawa in 1934 by introducing a new force called strong. The protons and neutrons are attracted to each other by a field which is quantized. The mediator of the strong interaction should be heavy due to a short range of the force. The first calculations showed that the mediator mass should be almost 300 times higher than electron mass. Hideki Yukawa called this particle a meson (meaning ”middle weight”). The first identification of a particle, which matched to the Yukawa's calculations, was made in 1937 by two separate groups (C. D. Anderson and S. Neddermeyer, J. C. Street and E. C. Stevenson) during studying the cosmic rays. The further studies showed that cosmic rays consist of two middle-weight particles: $\pi^{(1)}$ (consistent with Yukawa's calculation) and $\mu^{(2)}$ [1].

The second idea was developed on the basis of Klein-Gordon equation(3) which solution for free electron with energy (E), total momentum (p) and rest mass (m) is decribed as:

$$E^2 - p^2c^2 = m^2c^4 \rightarrow E = \pm\sqrt{p^2c^2 + m^2c^4}. \tag{1.1}$$

It means that energy can have positive or negative value. The interpretation was proposed by P. Dirac who suggested that the solution with $E > 0$ describes particle with $-e$ charge. The negative energy state describes particle with oppositive charge ($+e$). Therefore, the particle with the same mass as electron but $+e$ charge should exist. The matched positively charged particles, called positrons, were discovered by C. D. Anderson in 1931. The first explanation of the negative state was modified by E. Stückelberg and R. Feynman. They proposed that the positron is a particle (positively charged electron), traveling backwards in time. The idea of Feynman-Stückelberg interpretation is shown in Fig. 1.1. The consequence of the Klein-Gordon equation's solution for free particle is an existence of corresponding antiparticles for every kind of particles, with the same mass and opposite electric change (and baryon(4) number) [1, 3, 4], collectively called antimatter. But why is the Universe dominated by the matter? The possible explanation was proposed by F.Wilczek in 1980. He claimed that the CP symmetry(5) could be violated during decay of X (particles) and $\overline{X}$ (antiparticles) after the Big Bang. The lack of CP symmetry caused evolution of the Universe with equal number of X and $\overline{X}$ to the Universe with a positive baryon number. The baryon number is equal to +1 for baryons (e.g. proton, neutron) and -1 for antibaryons(6) (e.g. antiproton, antineutron) [5].

(1) Meson π (called pion) is defined in Fig. 1.4.

(2) Muon (μ) is elementary particle described in Table. 1.1.

(3) The Klein-Gordon equation is a relativistic wave equation which describes the free and spinless particle.

(4) The baryon is the type of particle which consists of the three valence quarks.

(5) The CP symmetry is a discrete symmetry given by charge conjugation (C) and parity (P). The charge conjugation is responsible for the transformation of matter to antimatter. The parity causes the flip in the sign of spatial coordinates.

(6) The antibaryon is the type of particle which consists of the three valence antiquarks.

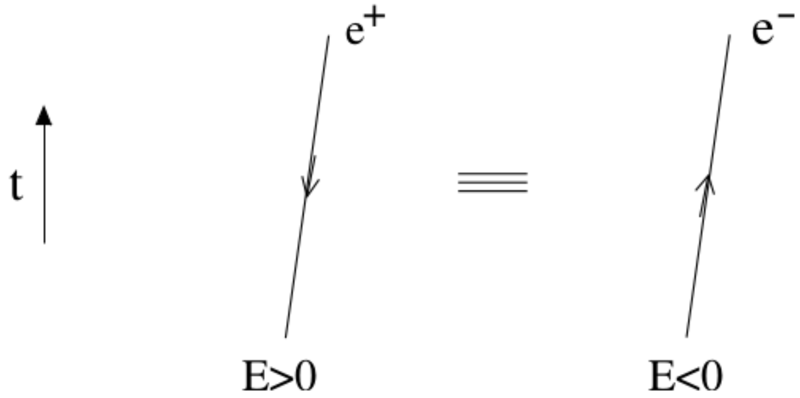

Figure 1.1: The idea of Feynman-Stückelberg interpretation: positron travelling backward in time is electron travelling forward in time. Figure taken from Ref. [4].

The third idea was developed on the basis of the beta decay observation ($^A_ZX \rightarrow ^A_{Z+1} Y + e^-$, where A and Z are mass and atomic numbers, respectively) in 1930. The energy of electron should have constant value for two-body decay process. But the experimental data showed that the emitted electrons have various energies. W. Pauli suggested that a third particle should be emitted during the beta decay, and called it a "neutron". The Pauli's explanation was received with a skepticism until the Seventh Solvay Conference in 1933, when E. Fermi showed his theory of the beta decay. He used the same approach as P. Dirac in the formulation of the theory of radiation. E. Fermi suggested that the third product of the beta decay is an extremely light particle and called it neutrino (in β^- decay it is called antineutrino now). The existence of a neutrino was confirmed by the experiment which was conducted at the Savannah River nuclear reactor in South Carolina in 1950 [1, 6].

The next 10 years were dominated by the search for new particles what caused the chaos in hadron(7) physics. The hadrons were divided in two groups: baryons and mesons, but without logical reason. The first attempt of classification of the particles was done in 1961 by Murray Gell-Mann who introduced geometrical patterns of dependence between different baryons and mesons based on their charge and strangeness(8). This methodology was called *the Eightfold Way* [7]. The example of baryon octet is shown in Fig. 1.2.

(7)Hadron – the particle which consists of three quarks (baryon), three antiquarks (antibaryon) or quark-antiquark pair (meson). They are held together by the strong force (see Table 1.1).

(8)Strangeness is a property (quantum number) of particles which can be defined as: $S = -(n_S - n_{\bar{S}})$, where n_S and $n_{\bar{S}}$ are the numbers of strange and antistrange quarks, respectively.

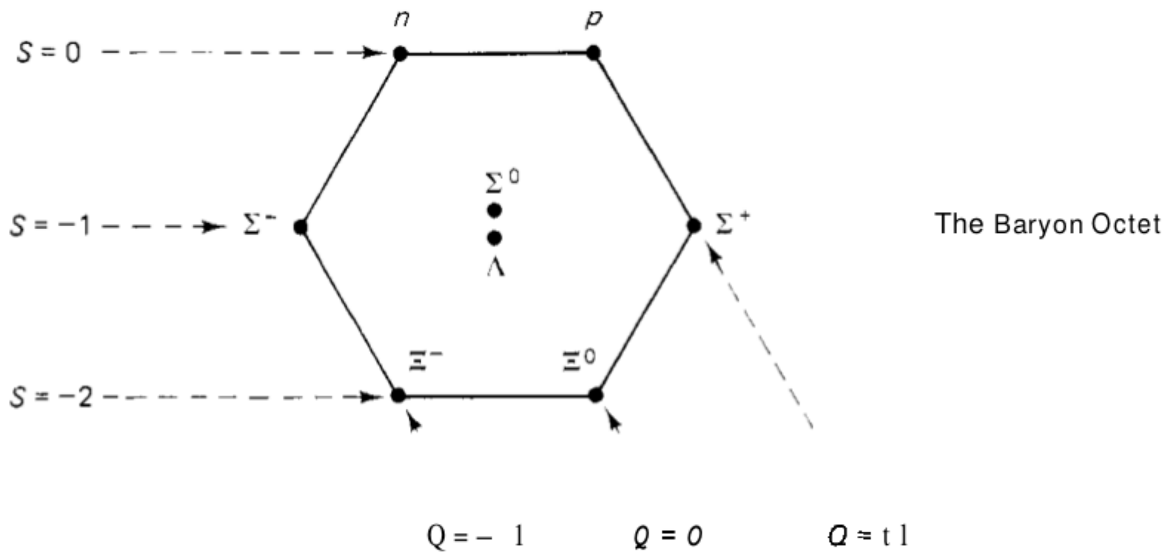

Figure 1.2: The baryon octet, where Q is electric charge and S is strangeness. Figure taken from Ref. [1].

The heavier baryons were grouped into decuplet. One of the predicted heavy baryons from the decuplet, with S=-3 and Q=-1, was discovered three years later and called Ω^-. This discovery convinced physicists to Eightfold Way method. But the question "Why do the hadrons fit into these patterns?" was still open. In 1964 M. Gell-Mann and G. Zweig independently suggested that all hadrons are made of elementary constituents called quarks. Originally, M. Gell-Mann proposed three types of quarks: u (up), d (down), s (strange), so-called flavours. They are shown in Fig. 1.3.

According to this theory, the baryons are composed of three quarks and the mesons are composed of a quark and an antiquark. The baryon decuplet and meson octet, expressed by the combination of quarks, are shown in Fig. 1.4. The quark model violated the Pauli exclusion principle, which means that two particles with half-integer spin cannot exist with the same state. The example of a violation of the Pauli exclusion principle is a Ω baryon which consists of three identical s quarks. The problem was resolved by introducing the new quantum number called *color*. The quarks can exist in three color states *red (R)*, *green (G)*, *blue (B)* and antiquarks in *anti-red* $(\overline{R})$, *anti-green* $(\overline{G})$, and *anti-blue* $(\overline{B})$, respectively. Only colorless particles are observed in nature [1,8]. More details about the physical meaning of color are available in Ref. [8].

One of the weaknesses of quark theory was the lack of quark existence evidence till 1974. During experiments with proton beams at the CERN (European Organization for

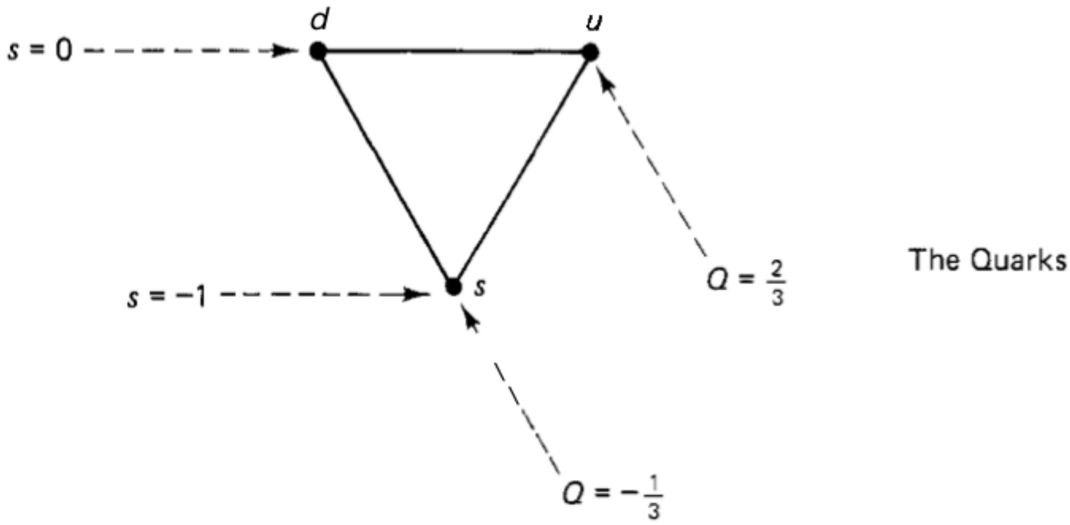

Figure 1.3: The quarks, suggested by M. Gell-Mann, formed in a triangle according to the *Eightfold Way* method. Figure taken from Ref. [1].

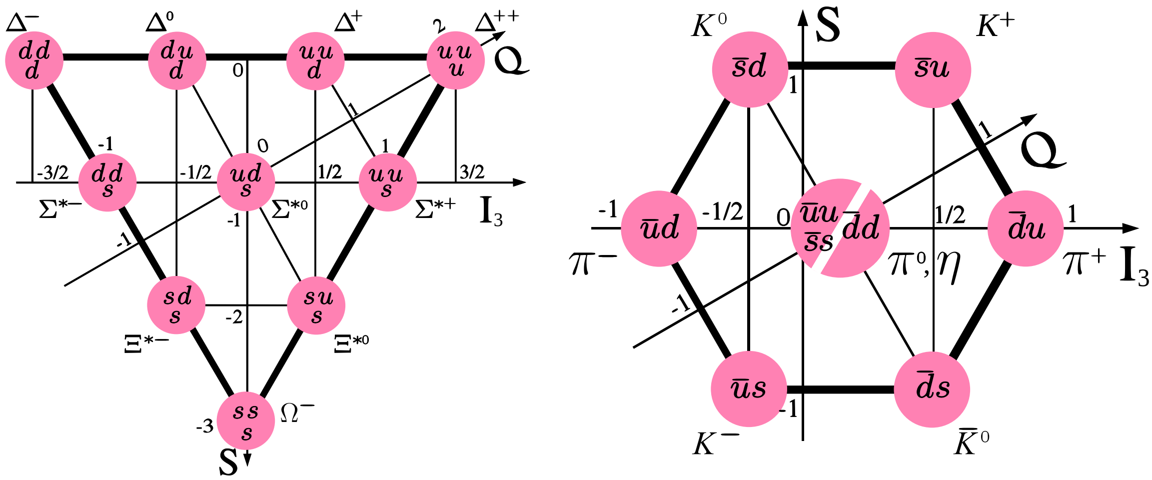

Figure 1.4: The baryon decuplet (left) and meson octet (right) expressed by the combination of quarks. The third component of the isospin (I_3) has $\frac{1}{2}(n_u - n_d - (n_{\bar{u}} - n_{\bar{d}}))$ value, where n_u, $n_{\bar{u}}$, n_d, and $n_{\bar{d}}$ are the numbers of up and down quarks or antiquarks, respectively. Figure taken from Ref. [9].

Nuclear Research), the number of particles deflected with large polar angles were observed. Similar phenomena were seen by E. Rutherford in 1911 and were used to prove the structure of an atom. During the next 10 years, the another three quarks were proposed: c (charm), b (beauty), and t (top) as explanation of discovered particles like $J/\psi(c\bar{c})$ or $\Upsilon(b\bar{b})$. The quark theory had another yet consequence. Namely, the Yukawa's meson cannot be a mediator of a strong force. The mediator, which is exchanged between two quarks, was called gluon [1, 8].

The evolution in perception of matter influenced on formulation of the *Standard Model*, which is used to explain experimental data nowadays. According to this model, the constituents of matter are: 6 leptons and antileptons, 6 quarks and 6 antiquarks (in fact 36 different quarks due to the color value) and 6 bosons (mediators in interactions). The quarks and leptons were divided into three generations. The stable particles (u, d, e, υ_e) are located in the first generation. The properties of particles are listed in the Table 1.1.

The Standard Model also focuses on four forces: electromagnetic, strong, weak and interaction with Higgs field. The most familiar electromagnetic force, with infinite range, is commonly associated with electricity but it also causes attraction between atomic nuclei and their electrons. The strong force was described above during the discussion about the Yukawa's meson and the weak force is responsible, for example, for β decay [3, 10]. The Higgs interaction is responsible for particle masses.

Although the Standard Model explains many of experimental data, it has limitations. The gravity theory still cannot be included in the model due to the problem with quantization of A. Einstein's theory of gravity. Additionally, in the Standard Model neutrinos are massless but the results of observed neutrinos oscillations prove that the neutrinos should have masses [12]. The Standard Model contains 19 free parameters which values should be taken from experimental results. It does not explain why there are six flavors of quarks and leptons. It does not explain the asymmetry between matter and antimatter either [3, 13]. The Standard Model is probably "the step" to better understand the constituents of matter and dependences between them. The future experimental data may help to develop the Standard Model to the new model with less questions and free parameters.

Quarks (fermions)							
Generation	I		II		III		
Name	Up	Down	Charm	Strange	Top	Bottom	
Symbol	u	d	c	s	t	b	
Electric charge (e)	$+\frac{2}{3}$	-$\frac{1}{3}$	$+\frac{2}{3}$	-$\frac{1}{3}$	$+\frac{2}{3}$	-$\frac{1}{3}$	
Mass (GeV/c^2)	∼0.0022	∼0.0047	1.3	∼0.1	173	4.2	
Discovered (year)	1964	1964	1974	1964	1995	1977	
Lifetime (s)	∞	∞	$\sim 10^{-12}$	$\sim 10^{-8}$	$\sim 10^{-24}$	$\sim 10^{-12}$	
Leptons (fermions)							
Name	Electron	Electron neutrino	Muon	Muon neutrino	Tau	Tau neutrino	
Symbol	e	υ_e	μ	υ_μ	τ	υ_τ	
Electric charge (e)	-1	0	-1	0	-1	0	
Mass (GeV/c^2)	∼0.0005	∼0	∼0.106	∼0	∼1.78	∼0	
Discovered (year)	1897	1956	1937	1962	1975	2000	
Lifetime (s)	∞	∞	$\sim 10^{-6}$	∞	$\sim 10^{-13}$	∞	
Force carriers (bosons)							
Force	Strong	Electro-magnetic		Weak		Gravity	Higgs interaction
Name	gluon	photon	Z^0	W^+	W^-	graviton	Higgs boson
Symbol	g	γ	Z^0	W^+	W^-	G	H^0
Electric charge (e)	0	0	0	+1	-1	0	0
Mass (GeV/c^2)	0	0	91.2	80.4	80.4	0	~ 125.1
Range (m)	$\sim 10^{-15}$	∞	$\sim 10^{-18}$	$\sim 10^{-18}$	$\sim 10^{-18}$	∞	
Discovered (year)	1979	1905	1983	1983	1983	No	2012
Particles affected	quarks, gluons	quarks, charged leptons		quarks, charged leptons, neutrinos		all	massive particles

Table 1.1: Names and characteristics of constituents of matter and force carriers in the Standard Model and Gravity. Table based on Refs. [10, 11].

1.2 Quark-Gluon Plasma

The strong potential between quarks can be described [3] by equation:

$$V(r) = -\frac{4}{3}\frac{\alpha_s}{r} + kr, \tag{1.2}$$

where α_s is the coupling constant of strong interactions, r is a distance, k is the strength of the linear term. The first part of Eq. 1.2 dominates for small distances between quarks. So that the potential between quarks behaves similarly to the Coulomb potential between electric charges. The second part of Eq. 1.2 dominates for large distances between quarks so that behavior of potential can be approximated by a string. The strong interactions potential will not increase to infinity with increasing distance because string will break and the quark-anti quark pair will be produced.

The virtual particles can be produced in vacuum according to the uncertainty principle ($\Delta E \Delta t \cong \hbar$). This process is called quantum fluctuation and causes that vacuum contains the sea of virtual particles. Another consequence of possibility of virtual particles production is a non constant value of the α_s (called *running coupling constant*). The α_s value depends on the number of virtual particles which lead to color charge screening (like electric charge screening in QED(9)) or antiscreening (dominates in QCD(10)). The α_s is decreasing logarithmically with increasing four-momentum transfer (Q^2), which causes that for large Q^2 quarks behave as free components of matter (*asymptotic freedom*). This behaviour of quarks motivated physicists to propose a new state of matter called *Quark-Gluon Plasma* (QGP) in which quarks and gluons are deconfined from their hadrons [13–18].

According to Ref. [20], the QGP occurs when the distance between hadrons is close to the size of a hadron. How can the quark-gluon plasma be produced in laboratory? The only possible way is a fast compression of hadrons which leads to a rise in temperature of the system e.g. by heavy-ion collision. In Fig. 1.5 two possible scenarios of heavy-ion collision, with and without the QGP state, are shown. After collision of the two Lorentz-contracted nuclei, the non-equilibrium state occurs. In this state the ”hard” processes (with large

(9) Quantum Electrodynamics (QED) is a branch of physics which describes quantum field theory of electromagnetic interactions.

(10) Quantum Chromodynamics (QCD) is a quantum theory which describes the strong interactions between quarks and gluons.

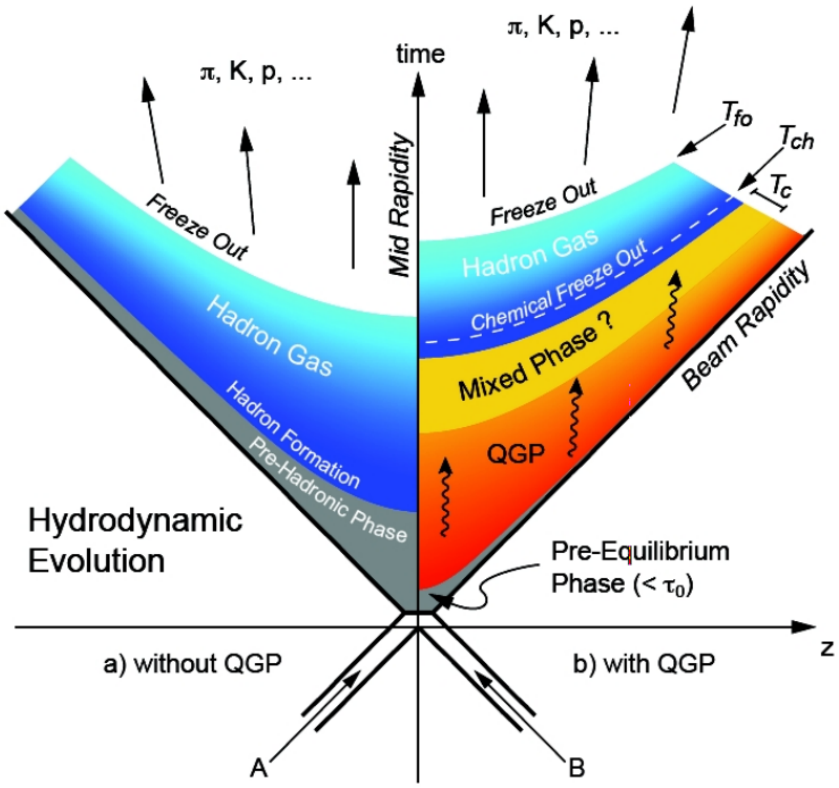

Figure 1.5: The space-time evolution of heavy-ion collision. Figure taken from Ref. [19].

momentum transfer) are possible. During further expansion of system, the "soft" processes (with small momentum transfer) lead to the local equilibrium state and thermalization ($\tau_0 \sim 0.6 - 1$ fm/c[(11)] after collision). If temperature of the system is high enough, the quark-gluon plasma is formed. During further expansion, temperature of the system is decreasing. The quarks and gluons couple in hadrons (hadronization) when temperature of the system is near the temperature for deconfinement. From Lattice QCD studies, this temperature (T_c), for baryon chemical potential[(12)] equal zero, is close to 156 MeV[(13)] [21]. The next step is *chemical freeze-out* when inelastic interactions are stopped and the composition of particles is fixed. The regeneration and rescattering of short-lifetime particles (*resonances*) are, however, still possible. When the temperature of the system drops to 90–130 MeV, the elastic interactions stop and the transverse momentum[(14)]

(11) 1 fm/c = $3.3 \cdot 10^{-24}$s

(12) Baryon chemical potential (μ_B) describes how the energy of the system changes when one baryon is added or removed from the system.

(13) 1 MeV = $1.2 \cdot 10^{10}$K.

(14) The transverse momentum is defined according to equation $p_T = \sqrt{p_x^2 + p_y^2}$, where p_x and p_y are particle momentum components perpendicular to the beam direction.

distribution of the produced particles is fixed (*kinetic/thermal freeze-out*). The resonances and other unstable particles can still decay after freeze-outs. It is estimated that more than half of produced pions come from resonance decays what affect calculations of kinetic freeze-out temperature [13, 19, 22]. More information about the resonance properties, and their role in high energy physics, are described in Chapter 2.

1.3 Phase diagram of strongly interacting matter

The phase diagram of strongly interacting matter (Fig. 1.6) allows to determine a state of matter depending on two parameters: temperature and baryon chemical potential (μ_B). In Fig. 1.6, the first order phase transition is marked, which separates hadron gas and quark-gluon plasma (described in Chapter 1.2) or color superconductor states. The color superconductivity is created by quark pairs (Cooper pairs) which condense. The QGP-hadron gas transition also separates regions with broken chiral symmetry(15) (hadron gas state) and restored chiral symmetry (QGP state). For many years, it was claimed that chiral transition and deconfinement occur at the same temperature and μ_B. The later papers (Ref. [24, 25]) showed that these two transitions may be separated in the phase diagram of strongly interacting matter [13, 26].

At the end of the line representing the first order phase transition a critical point (CP) is probably located (where the second order phase transition occurs) in which hadron gas and QGP can coexist and smoothly pass into each other. The big fluctuations of mean number of particles $\langle N \rangle$ and mean transverse momentum $\langle p_T \rangle$ are suspected [27] in the CP region due to the lack of energetic barrier between two states of matter. The prediction of critical point ($\mu_B \neq 0$) is technically problematic using lattice calculations only. The location of the critical point is estimated by extrapolation from $\mu_B = 0$ region. The more information is determined by adding models to lattice calculations. The most reliable predictions indicate critical point in region $200 < \mu_B < 500$ MeV which corresponds to the Super Proton Synchrotron (SPS) and Relativistic Heavy Ion Collider (RHIC) Beam Energy Scan (BES) energies ($6.5 < \sqrt{s_{NN}}$(16)< 17.3 GeV) [28].

(15)Chirality is a projection of spin to momentum vector of particle. Chiral symmetry refers to axial flavor transformation of the quark part of the QCD Langrangian density, which requires massless quarks (see Ref. [23]). The chiral symmetry is broken due to the existence of massive quarks (see Table. 1.1).
(16)$\sqrt{s_{NN}}$ is the energy available in the center-of-mass system for nucleon pair.

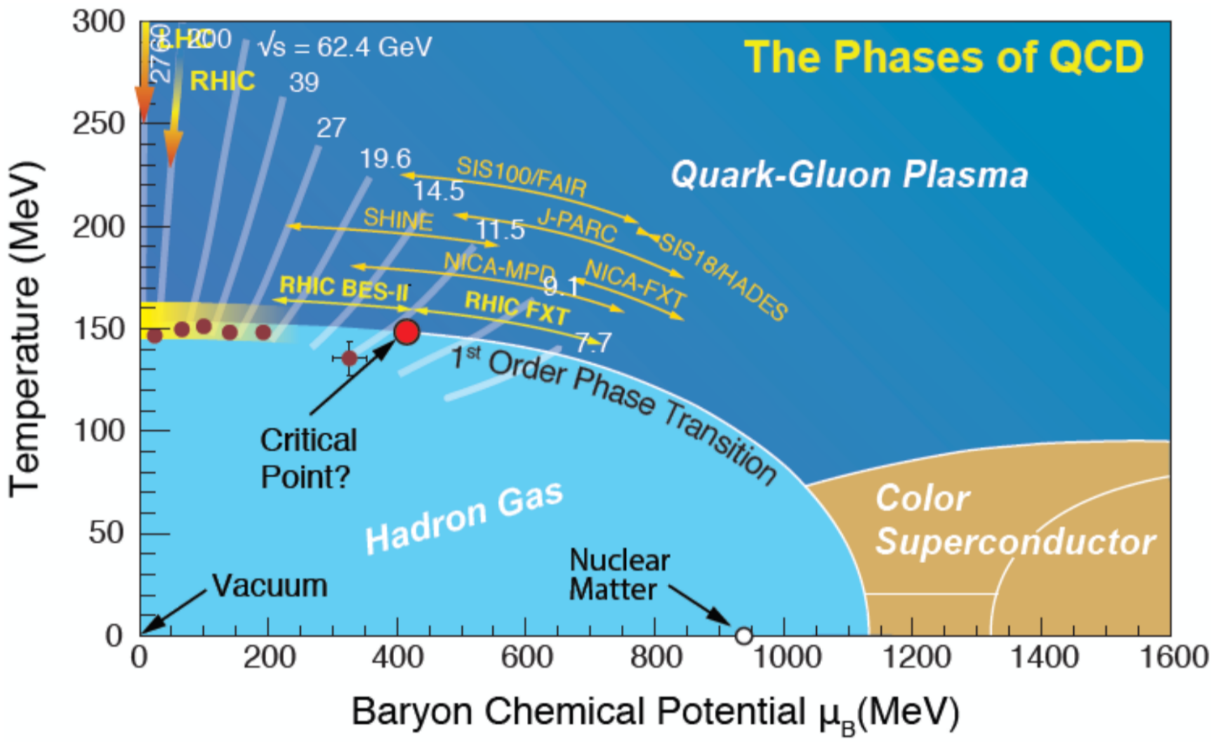

Figure 1.6: The phase diagram of strongly interacting matter. The existing and future accelerators or experiments are also shown. Small red circles represent chemical freeze-out points at different collision energies. Figure taken from Ref. [30].

Further decreasing of μ_B value leads to cross-over region in which physical parameters of state are changed rapidly but smoothly. The lattice QCD calculations for $\mu_B = 0$ allow to determine the region of transition temperature between hadron gas and QGP. The T_c from lattice QCD may depend on the number of quark flavors and their masses used in calculations. The most recent calculations suggest T_c=156.5±1.5 MeV [21].

The phase diagram in Fig. 1.6 is experimentally scanned by changing the collision energy (mostly along the x axis) and, at the SPS energies [29], the size of the colliding system (along the y axis). The temperatures of QGP, reached at the early stage, are about: 230 MeV (SPS), 300–500 MeV (RHIC) and 600–700 MeV (Large Hadron Collider, LHC).

1.4 Onset of Deconfinement

The Statistical Model of the Early Stage (SMES) [31] gives an answer about localization of the energy region in which the onset of deconfinement (minimum collision energy

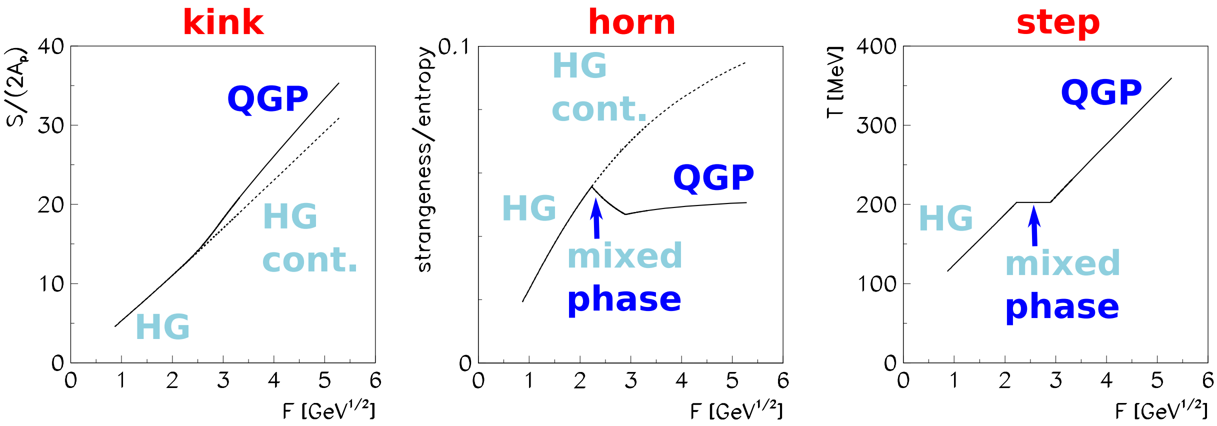

Figure 1.7: The structures predicted by the Statistical Model of the Early Stage. Figure taken from Refs. [13, 31].

to create QGP state) occurs. The model assumes three phases: confinement, mixed phase and deconfinement. The temperature of the mixed phase (hadronization) was fixed at $T_c = 200$ MeV. The two most important assumptions of the SMES model are that the whole number of created heavy flavors and the whole entropy are the same before and after hadronization. Moreover, the number of internal degrees of freedom (g) increases at the transition to QGP. More assumptions are described in Ref. [31].

Information about the early stage is given by studing the energy dependence of variables insensitive to hadronization and expansion processes, such as entropy (carried by pions – quantitatively dominant particles produced in the collision) and heavy flavour production (strangeness, charm) [31, 32]. In Fig. 1.7 the structures predicted by the SMES model are shown.

The first structure ("kink") describes the behavior of the total entropy to the number of nucleons in central A+A collisions as a function of Fermi energy:

$$F = \left[\frac{(\sqrt{s_{NN}} - 2m_N)^3}{\sqrt{s_{NN}}} \right]^{\frac{1}{4}} \simeq \sqrt{\sqrt{s_{NN}}}, \tag{1.3}$$

where nucleon mass is denoted by m_N. The slope of this function should be proportional to $g^{1/4}$, where g is an effective number of degrees of freedom in the early stage. The g value increases after transition to QGP stage.

The second structure ("horn") describes the behavior of the strangeness to entropy ratio as a function of Fermi energy. The maximum of the ratio is expected for deconfinement transition energy. This is connected with g_s/g ratio, where g_s and g are strangeness and total degrees of freedom, respectively [31].

The last structure ("step") describes the temperature as a function of energy. The temperature should increase with collision energy during confined or deconfined stages, whereas a plateau is expected for a mixed phase.

The proposed measures (pion production as a proxy of entropy in Fig. 1.8, charged kaon to pion ratio as a proxy of strangeness to entropy in Fig. 1.9 and inverse slope parameter of transverse mass(17) spectra in Fig. 1.10) were studied by the NA49, STAR, ALICE, and NA61/SHINE experiments. The onset of deconfinement was found by NA49 [33] in central Pb+Pb collisions at middle SPS energies ($\sqrt{s_{NN}} \approx 7.6$ GeV). In principle, the $\langle\pi\rangle/\langle W\rangle$ ratio (Fig. 1.8) showed a change of slope (due to activation of partonic degrees of freedom) in central Pb+Pb collisions at middle SPS energies. Such a change of slope is not observed for p+p data. The horn structure was also observed in K^+/π^- ratios in central Pb+Pb data (Fig. 1.9). Finally, a plateau in the inverse slope parameter of kaon m_T spectra was also observed for Pb+Pb data at SPS energies (Fig. 1.10). The structures observed by the NA49 experiment are currently studied by NA61/SHINE for different collision systems (p+p, Be+Be, Ar+Sc, Xe+La). The results for p+p, Be+Be, and Ar+Sc collisions are presented in Figs. 1.8, 1.9, and 1.10. The $\langle\pi\rangle/\langle W\rangle$, K^+/π^+ ratios and inverse slope (T) parameters of m_T spectra for Be+Be collisions are close to p+p results. The $\langle\pi\rangle/\langle W\rangle$ points for Ar+Sc collisions lie either on p+p curve (for low energies) or on Pb+Pb curve (for higher energies). The K^+/π^+ ratios for Ar+Sc collisions are higher than the ones for Be+Be or p+p data, but the horn structure is not observed. The T parameters of Ar+Sc data are located between p+p/Be+Be and Pb+Pb/Au+Au data.

(17)The transverse mass is defined as $m_T = \sqrt{m^2 + p_T^2}$, where m is a particle rest mass.

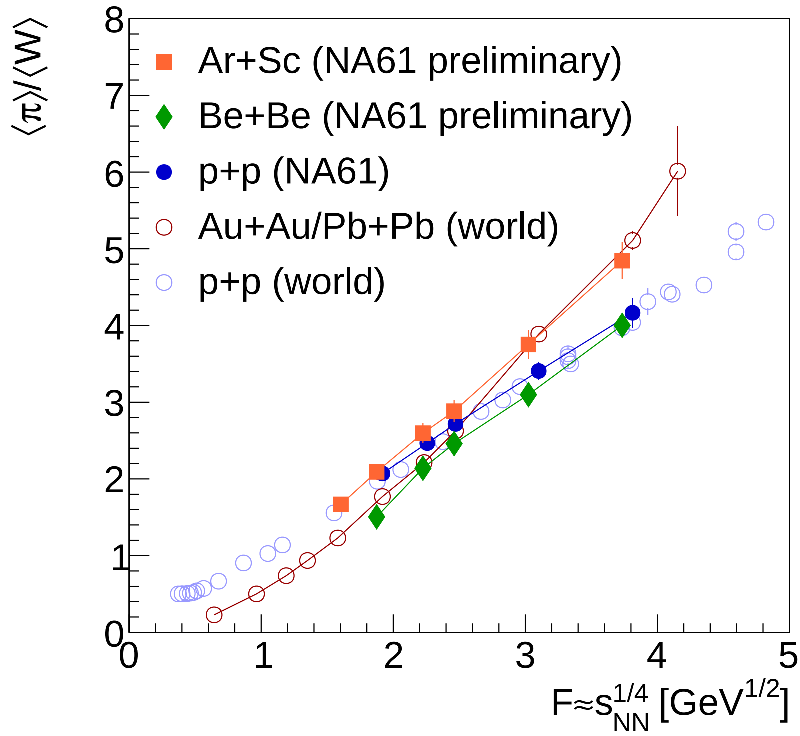

Figure 1.8: The mean π meson multiplicity divided by the mean number of wounded nucleons (W) in full 4π phase. Figure taken from Ref. [34].

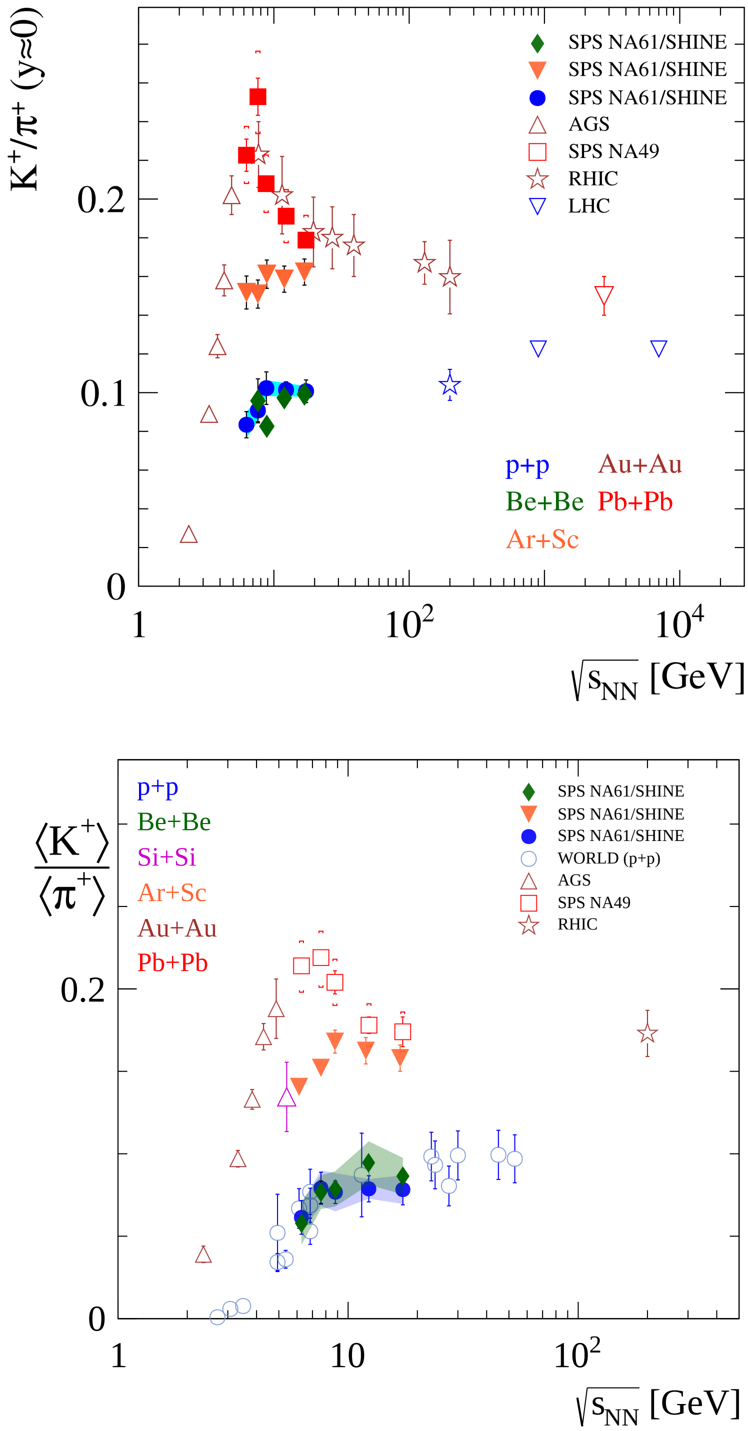

Figure 1.9: The K^+/π^+ ratio as a function of energy at mid-rapidity (top) and in 4π (bottom). Mid-rapidity is a region close to $y = 0$ where y is calculated in the collision center-of-mass reference system. The kaon and pion multiplicities in NA61/SHINE p+p data are taken from Ref. [35]. The world data are taken from Ref. [36] and references therein. Figures taken from Ref. [37].

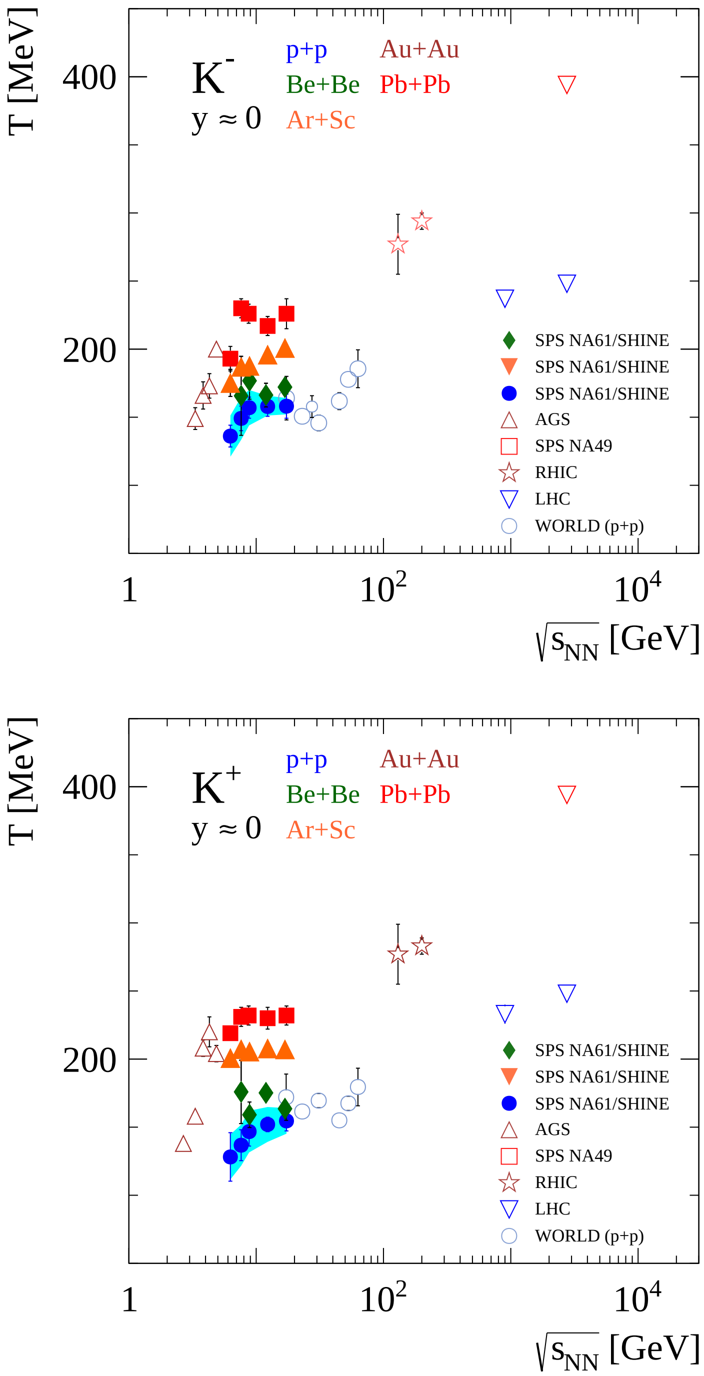

Figure 1.10: The inverse slope parameter (T) of m_T spectra of K^- (top) and K^+ (bottom) as a function of energy. The kaon spectra in NA61/SHINE p+p data are taken from Ref. [35]. The world data are taken from Ref. [36] and references therein. The m_T spectra can be described by $\frac{dN}{dm_T} \sim m_T \exp\left(-\frac{m_T}{T}\right)$, where T is kinetic freeze-out temperature plus additional part connected with colective (radial) flow of the system. Figure taken from Ref. [37].

Chapter 2

Resonance production and evolution of the system

The short-lived particles, which decay via strong interactions, are called *resonances*. Their lifetimes are of the order of about 10^{-23} s, so they are not directly observed but studied through their stable decay products (daughters). The properties of resonances are determined on the basis of the invariant mass (m_{ab}) of decay products, defined for two body decays as:

$$m_{ab} = \sqrt{(E_a + E_b)^2 - (\vec{p_a} + \vec{p_b})^2}, \tag{2.1}$$

where: E_a and E_b are energies of particles a and b, respectively, $\vec{p_a}$ and $\vec{p_b}$ are momenta of particles a and b, respectively. The resonance particle is visible as a peak in invariant mass distribution.

The lifetime (τ) of a resonance, at rest frame, can be calculated [38] on the basis of the uncertainty principle:

$$\begin{aligned} &\Delta E \Delta t \cong \hbar, \\ &\Delta E \approx \Gamma; \quad \Delta t = \tau, \\ &\tau \cong \tfrac{\hbar}{\Gamma}, \end{aligned} \tag{2.2}$$

where Γ (resonance width, see below) is taken from the fit to invariant mass distribution of decay products, $\hbar = \frac{h}{2\pi}$=$6.582 \cdot 10^{-22}$ MeV·s, h is Planck constant.

The fit to invariant mass distribution is based on *Breit-Wigner* equation:

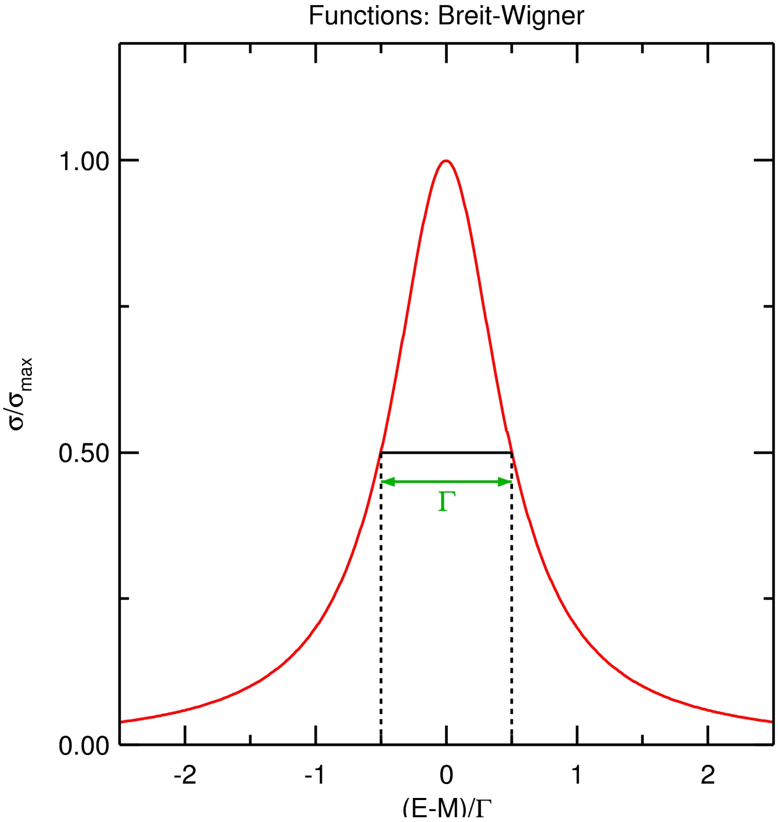

Figure 2.1: The Breit-Wigner distribution. Figure taken from Ref. [13].

$$\sigma(E) = \sigma_{max} \frac{\frac{\Gamma^2}{4}}{(E-M)^2 + \frac{\Gamma^2}{4}}, \tag{2.3}$$

which is a result of Fourier transformation of the particle wave function [3, 39]. The σ_{max} is a maximum of σ value. The E is the center-of-mass energy that produces the resonance, M is the mass of the resonance, and Γ is the resonance width (width of the distribution at σ/σ_{max}=0.5). The shape of Breit-Wigner distribution is shown in Fig. 2.1.

Short-lived particles can decay in various channels. The branching ratio:

$$BR = \frac{\Gamma_i}{\Gamma} \tag{2.4}$$

is the number of decays of resonance in the *i-th* channel to the total number of its decays. It allows to determine the multiplicity[(1)] of the chosen resonance by studying only one decay channel [39].

Following the Particle Data Group (PDG) [11] convention, in this thesis the momentum unit is expressed in MeV/c or GeV/c and mass (including invariant mass and

[(1)]Multiplicity is the number of specified particles per event (collision).

transverse mass) in MeV or GeV. Moreover, $c = 1$ is assumed in all calculations.

2.1 History of studying resonances

The history of short-lived particles began in the Chicago Cyclotron in 1952 when H. Anderson and E. Fermi observed a difference between the π^+p and π^-p total cross sections. The range of energy was not enough to see the whole shape of the resonance but this result motivated other groups to perform more measurements. The group from the Rochester cyclotron confirmed that there is a resonance called $\Delta(1232)$ [40].

The next breakthrough was a discovery of the first strange resonance called $Y_I^*(1385)$ ($\Sigma(1385)$ nowadays) during the experiments with K^- beams in hydrogen bubble chambers at the Bevatron in 1960. The studies of Luis Alvarez team showed a peak in the $\Lambda\pi$ invariant mass with a maximum at 1385 MeV. By the end of 1960, the same team found two other strange resonances [41,42]: $K^*(890)$ and $Y_o^*(1405)$ called nowadays $K^*(892)$ and $\Lambda(1405)$, respectively. In Fig. 2.2 a first reconstructed $K^*(890)^0$ peak is shown by using invariant mass of $K^+\pi^-$ pairs [43].

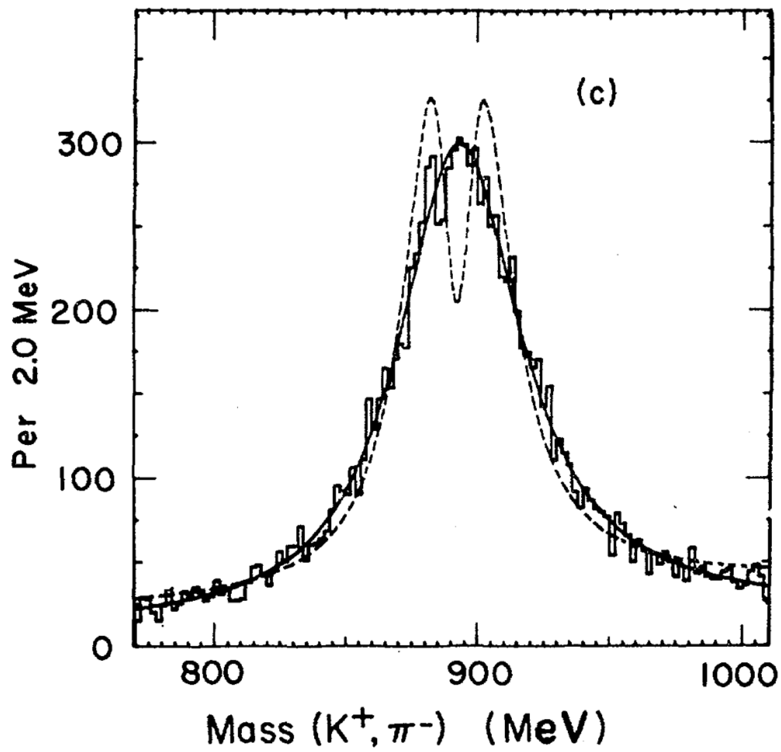

Figure 2.2: The first $K^*(890)^0$ peak. Figure taken from Ref. [43].

In the next year, A. R. Erwin *et al.* observed the ρ resonance by studying the invariant mass distribution of $\pi^+\pi^-$ pairs at the Cosmotron. The calculation of initial ρ mass was difficult due to large width of this resonance. Thanks to the work of two groups (team of G. Chew and F. E. Low and team of R. M. Walker), the mass of ρ was finally calculated as 765 MeV. At the same time, Bogdan Maglić (visitor in Luis Alvarez's team) studied proton-antiproton annihilation and discovered the ω resonance in invariant mass of $\pi^+\pi^-\pi^0$ [40, 44].

The introduction of particle grouping method called the Eightfold Way (described in Sec. 1.1) showed properties of missing particles which caused discovery of other resonances such as: η (1962), $\Xi^*(1530)$ (1962), ϕ (1963), and Ω^- (1964) [40, 44].

In Table 2.1 there are resonances shown which are actually being studied by the high-energy experiments. The main topic of this thesis is studying the $K^*(892)^0$ yields, so that the next chapter will focus on this meson.

	$\rho(770)$	$\Delta(1232)$	$K^*(892)^0$	$\Sigma(1385)$	$\Lambda(1520)$	$\phi(1020)$	$f_0(980)$
Decay channel	$\pi\pi$	$N\pi$	$K^+\pi^-$	$\Lambda\pi$	$N\overline{K}$	K^+K^-	$\pi\pi$
BR (%)	~ 100	~ 99.4	~ 66.66	~ 87	~ 45	~ 49.2	seen
Mass (MeV)	~ 775	~ 1232	~ 895.55	~ 1383.7	~ 1519.5	~ 1019.5	990
Width (MeV)	~ 149	~ 117	~ 47.3	~ 36	~ 15.6	~ 4.25	10-100
Lifetime (fm/c)	~ 1.32	~ 1.7	4.17	~ 5.5	~ 12.6	~ 46	$\sim 2 - 20$

Table 2.1: The list of selected resonances measured by high-energy experiments. Based on Ref. [11].

2.2 Motivation to study $K^*(892)^0$

In Sec. 1.2, the space-time evolution of heavy-ion collision was described with assumption that chemical (end of inelastic collisions) and kinetic (end of elastic collisions) freeze-outs occur at different times. The yields of short-lifetime resonances can help to distinguish between the two possible freeze-out scenarios: the sudden and the gradual one [45]. The time interval between freeze-outs can be estimated on the basis of the $K^*(892)^0$ to charged kaons ratio in small (e.g. p+p) and heavy (e.g. Pb+Pb, Au+Au) systems. The $K^*(892)^0$ meson is chosen to study the time interval between freeze-outs because its lifetime (≈ 4 fm/c) is comparable to the expected duration of the hadronic gas rescattering phase between freeze-outs. Therefore, the certain fraction of $K^*(892)^0$ mesons will decay inside the fireball(2) what causes modifications of their decay products momenta due to elastic scattering. These modifications prevent the experimental reconstruction of the $K^*(892)^0$ resonance via an invariant mass analysis what causes a suppression of the observed $K^*(892)^0$ yield. Such an effect was indeed observed in nucleus-nucleus collisions at SPS and RHIC energies [46–51]. The suppression of the observed $K^*(892)^0$ yield from the SPS data is shown in Fig. 2.3. The K^*/K ratio (K^* stands for $K^*(892)^0$, $\overline{K^*}(892)^0$ or $K^{*\pm}$, and K denotes K^+ or K^-) showed a decrease with increasing system size due to the increasing rescattering time between two freeze-outs. A similar trend was recently observed by the ALICE Collaboration (Fig. 2.4) at the LHC energy [52–55].

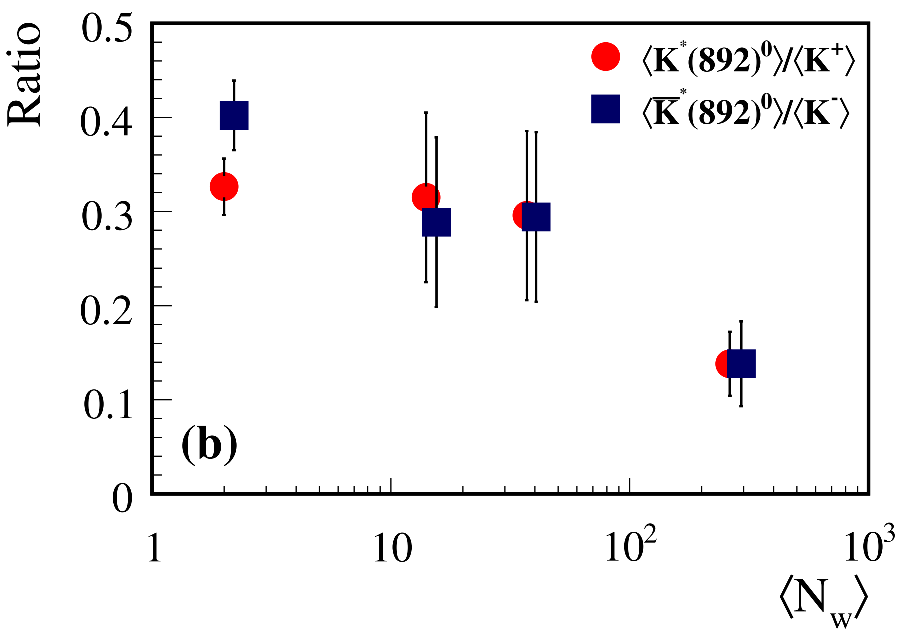

Figure 2.3: $\langle K^*(892)^0\rangle/\langle K^+\rangle$ (circles) and $\langle\overline{K^*}(892)^0\rangle/\langle K^-\rangle$ (squares) for p+p (most left), C+C, Si+Si, and Pb+Pb (most right) collisions at 158A GeV/c (A GeV/c means GeV/c per nucleon) beam momentum. N_W stands for the number of wounded nucleons. The error bars represent total uncertainties. Figure taken from Ref. [47].

The values of K^{*0}/K^- ratio(3) from LHC and RHIC as a function of energy are com-

(2)Fireball is a dense and hot matter created after heavy ion collision.

(3)In ALICE at LHC and STAR at RHIC papers. e.g. Refs. [50, 53, 55], the results for $K^*(892)^0$ and $\overline{K^*}(892)^0$ were combined and averaged and denoted by the symbol K^{*0}. The $K^*(892)^0$ and $\overline{K^*}(892)^0$ mesons were studied at mid-rapidity.

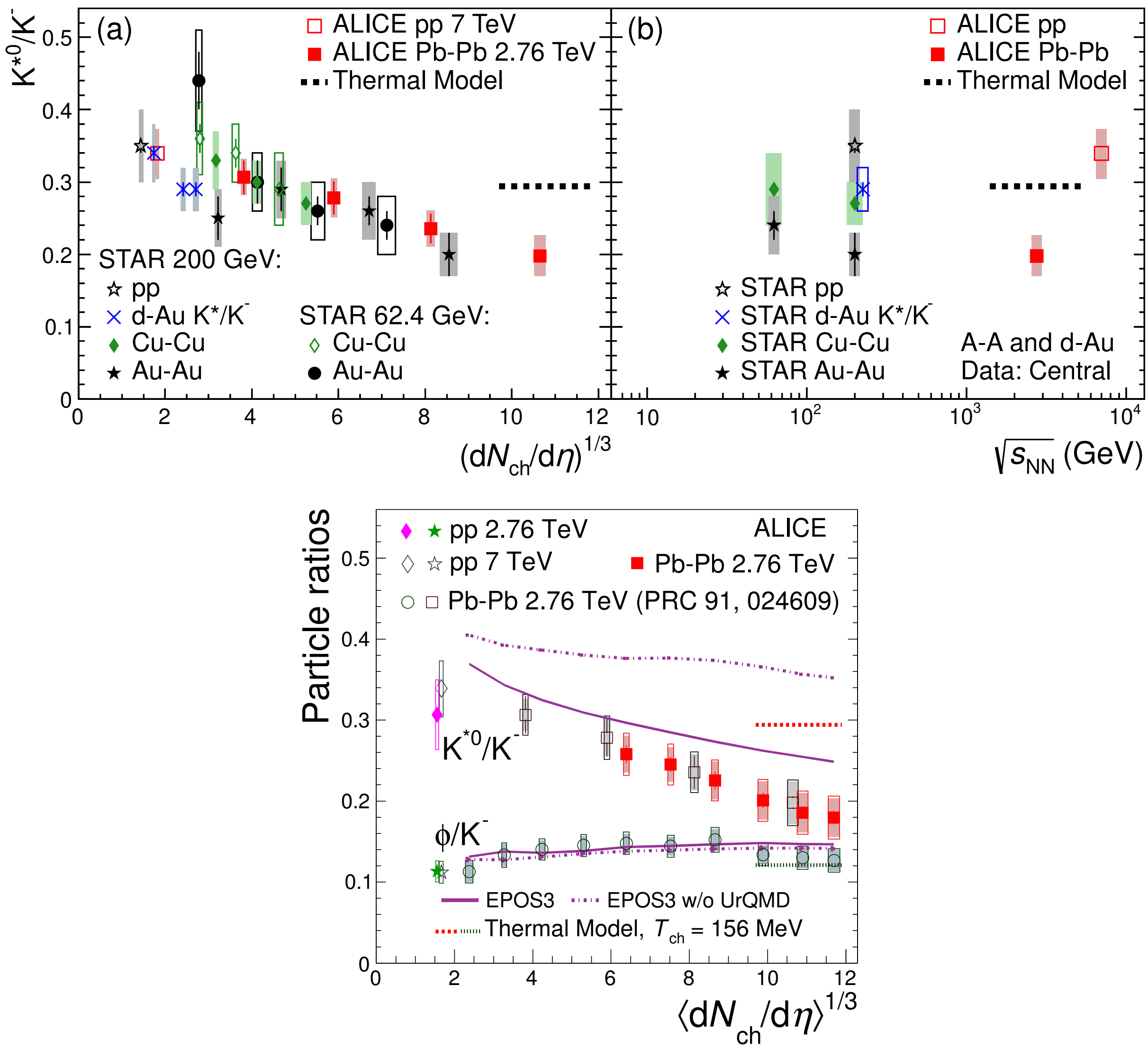

Figure 2.4: The ratios of K^{*0}/K^- and ϕ/K^- (only bottom) in p+p, d+Au, and A+A collisions. For d+Au collisions the multiplicity of K^{*0} is a combination of the charged and neutral K^{*0}. Figures taken from Refs. [52] (top) and [53] (bottom).

pared and shown in Fig. 2.4. The ALICE results for 2.76 TeV[(4)] LHC energy [53] indicate a bit larger suppression of K^{*0} than for the top RHIC energy (200 GeV) [50]. The reported values are: $K^{*0}/K^- = 0.180 \pm 0.027$ (0.186 ± 0.027) for the 0-5% (5-10%) central Pb+Pb reactions at LHC and 0.20±0.04 for the 0-10% most central Au+Au interactions at RHIC. The values of K^{*0}/K^- ratios in heavy systems (Pb+Pb or Au+Au) can be compared with those for small system (p+p), which are equal to 0.307±0.043 at LHC [53] and 0.34±0.05 at RHIC [50]. Thus, the LHC data (2.76 TeV) show the drop of K^{*0}/K^- ratio in heavy

[(4)]The K^{*0}/K^- ratios in Pb+Pb collisions at $\sqrt{s_{NN}} = 2.76$ TeV and 5.02 TeV are in agreement within uncertainties [55].

system to about 59 (61)% of the value found for p+p interactions. For RHIC data this drop equals 59%.

The NA49 experiment obtained the (almost 4π) mean multiplicities of, separately, $K^*(892)^0$ and $\overline{K^*}(892)^0$ mesons in the 23.5% most central Pb+Pb collisions at $\sqrt{s_{NN}}$ = 17.3 GeV. The values of mean multiplicities of $K^*(892)^0$ and $\overline{K^*}(892)^0$ mesons are equal to 10.3 ± 2.5 and 5.2 ± 1.7, respectively [47]. These values can be rescaled to the 5% most central Pb+Pb collisions using the mean number of wounded nucleons (factor 362/262, see Table 6.3). The results after rescaling are equal to 14.2 ± 3.5 and 7.2 ± 2.3, respectively. The average value of multiplicity of $K^*(892)^0$ and $\overline{K^*}(892)^0$ was calculated and divided by $\langle K^- \rangle$ multiplicity (51.9 ± 3.6) for the 5% most central Pb+Pb collisions [56]. The result is 0.21 ± 0.04, which is similar to the value $K^{*0}/K^- = 0.20 \pm 0.04$ obtained by RHIC in the 10% most central Au+Au collisions at $\sqrt{s_{NN}}$=200 GeV [50]. The ratio $0.5 \cdot (\langle K^*(892)^0 \rangle + \langle \overline{K^*}(892)^0 \rangle)/\langle K^- \rangle$ was also calculated for p+p interactions at the same SPS energy and is equal to 0.49 ± 0.03 [47,57]. Therefore, a drop of the resonance to charged kaons ratio in central Pb+Pb collisions is to about 43% of the value for p+p interactions. This suppression of $K^*(892)^0$ and $\overline{K^*}(892)^0$ mesons is even stronger than the one observed at LHC and RHIC. It might suggest that the time interval between freeze-outs (calculated in the K^{*0} rest frame; see Eq. 6.1 in Sec. 6.4) in central nucleus-nucleus collisions at the SPS is longer than that at higher energies. The another possible explanation is a longer contribution of resonance regeneration processes for higher energies what counteracts the K^{*0} suppression due to rescattering. One should also note that in these considerations, the same conditions at chemical freeze-out of p+p and Pb+Pb collisions were assumed. The detailed calculations of the time interval between chemical and kinetic freeze-outs, in the K^{*0} rest frame and in collision center-of-mass reference system, are presented in Sec. 6.4.

As seen, the results from p+p collisions provide an important base-line for heavier nucleus-nucleus systems. The published RHIC and LHC results on the K^{*0}/K^- ratio for p+p interactions are similar [53, 55, 58, 59] as is shown in Fig. 2.5. The most of results at lower energies are burdened with large uncertainties what causes that these are less reliable (see the compilation in Ref. [58] and new points in Refs. [47, 53, 55, 59]). This situation indicates a need for obtaining high precision p+p data at lower energies e.g. SPS energies.

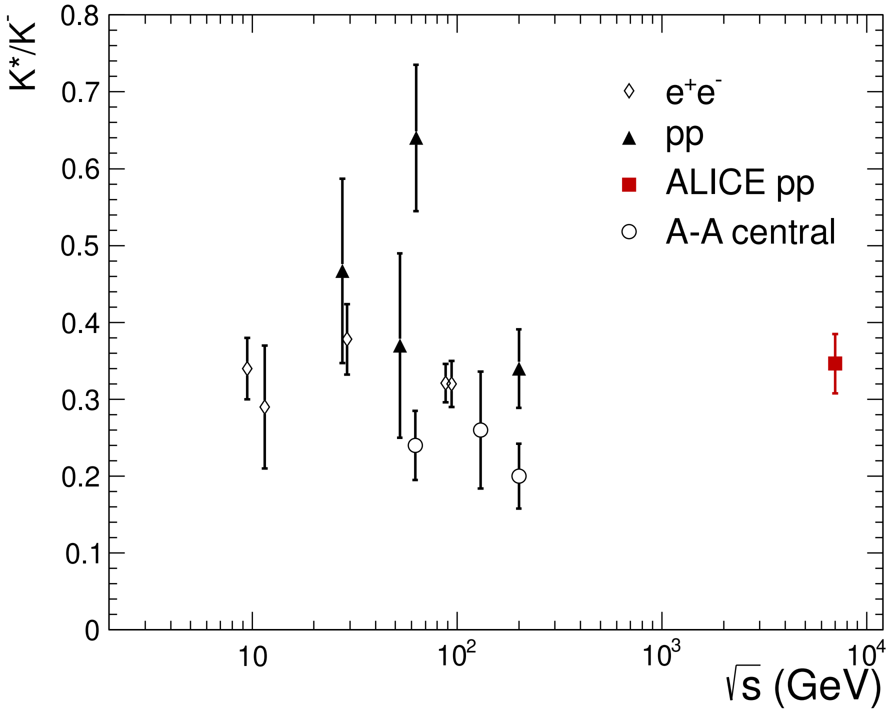

Figure 2.5: The ratio of K^{*0}/K^- for $e^+ + e^-$, p+p, and central A+A collisions as a function of collision energy. Figure taken from Ref. [58].

Moreover, recently the ALICE experiment reported a very intriguing effect in the analysis of the multiplicity dependence of resonance production in p+p collisions [60, 61]. The $K^{*0}/\langle K^{\pm}\rangle$ and K^{*0}/K^0_S ratios decrease when going from low-multiplicity to high-multiplicity p+p interactions at the LHC energies (Fig. 2.6). This effect might be explained as an existence of a hadronic phase, with non-zero lifetime, even in p+p collisions.

The $K^*(892)^0$ transverse mass spectra and yields are also important inputs for Blast-Wave models and Hadron Resonance Gas models (HGM). The first model is used to determine kinetic freeze-out temperature and transverse flow velocity. The HGM allows to determine chemical freeze-out temperature, baryochemical potential, strangeness under-saturation factor, system volume, etc. Those models significantly help to understand the phase diagram of strongly interacting matter. The recent LHC, RHIC and even SPS results indicate that dense and collectively behaving system can appear also in collisions of small nuclei, or even in elementary interactions. Therefore, it is important to determine transverse flow velocity precisely. Moreover, the resonance decay products make a large fraction of the final state particles. Therefore, the measured resonance yields in elementary interactions give a contribution to understanding of hadron production process. Finally,

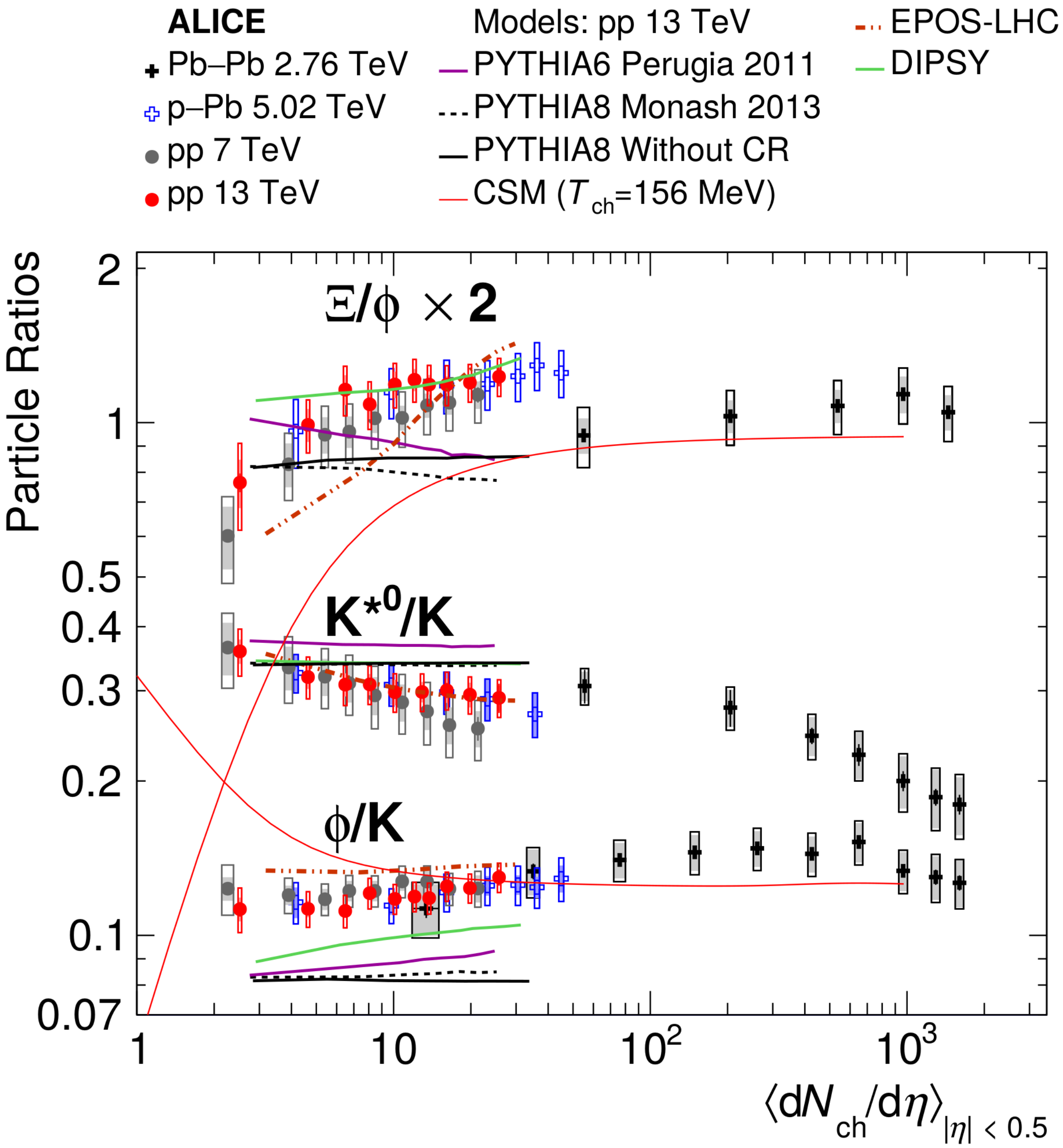

Figure 2.6: The ratio of K^{*0}/K, ϕ/K (K denotes K^- for Pb+Pb, average of K^+ and K^- for p+Pb and 7 TeV p+p, and K^0_S for p+p at 13 TeV [62]), and Ξ/ϕ yields in several systems, including p+p collisions at $\sqrt{s} = 13$ TeV. Figure taken from Ref. [61].

the resonance spectra and yields provide an important reference for tuning Monte Carlo string-hadronic models.

The $K^*(892)^0$ and/or $\overline{K^*}(892)^0$ production measurements in p+p collisions were performed at RHIC energies by the the STAR [48] and PHENIX [63] experiments and at LHC energies by ALICE [53, 55, 58, 59, 61, 64]. For the energies lower than RHIC and LHC, the $K^*(892)^0$ and/or $\overline{K^*}(892)^0$ were studied by the NA49 experiment in inelastic p+p collisions at 158 GeV/c ($\sqrt{s_{NN}}$=17.3 GeV) (CERN SPS) [47]. The LEBC-EHS facility at the CERN SPS also obtained $K^*(892)^0$ and $\overline{K^*}(892)^0$ yields in p+p collisions at 400 GeV/c beam momentum [65]. Finally, the measurements received at the energies of the CERN Intersecting Storage Rings (ISR) were published in Refs. [66, 67].

At the end, it is worth to mention that the analysis of resonance production in heavy nucleus-nucleus systems (not the subject of this thesis) may allow to better understand the QGP properties and the origin of particle mass. This is due to the fact that in the vicinity of a dense hadronic matter (QGP) the properties of some resonances (their masses, widths, branching ratios) may be modified due to the partial chiral symmetry restoration [68–71].

Chapter 3

NA61/SHINE experiment

The NA61/SHINE (*SPS Heavy Ion and Neutrino Experiment*) is a fixed target experiment located at the Super Proton Synchrotron at the CERN accelerator complex (more details are given in Sec. 3.2). The experiment was proposed in 2006 year to realize rich program focused on heavy ion, cosmic ray and neutrino physics. More details about the NA61/SHINE physics program are given in Sec. 3.1. The first data taking for ion program (strong interactions program) was realized in 2009 year and started a comprehensive two-dimensional scan with beam momentum and collision energy. The NA61/SHINE Collaboration consists of about 140 physicists from about 30 institutes [72].

3.1 Physics program

The NA61/SHINE program is divided into three main categories connected with heavy ion (strong interactions), cosmic ray and neutrino physics. The first category is focused on studying the phase diagram of strongly interacting matter by changing beam momentum (from 13A to 150(8)A GeV/c) and system size (from p+p to Pb+Pb). The collected and future data are shown in Fig. 3.1. The main goal of the 2D scan is studying the properties of the onset of deconfinement and search for the critical point which probably is located in the energy range available by SPS.

The next topic realized by the NA61/SHINE experiment is connected with cosmic ray physics. The Pierre-Auger Observatory and KASCADE experiment study the extensive air showers registered by the lateral coverage ground detector arrays. The registered tracks are reconstructed by using the simulations of the air shower. The existing models are

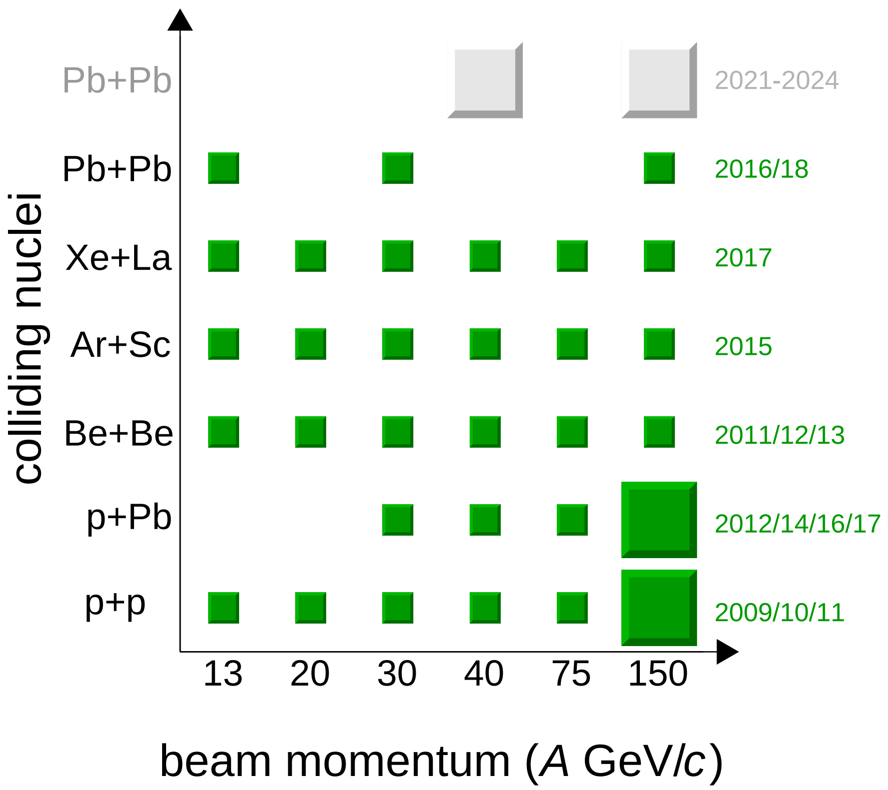

Figure 3.1: The data recordered and planned to be recorded within the strong interactions program of the NA61/SHINE experiment. The proton beam momenta are: 13, 20, 31, 40, 80, and 158 GeV/c. The ion beam momenta are: 13A, 19A, 30A, 40A, 75A, and 150A GeV/c. Figure taken from Ref. [73].

sensitive to $\mu^{\pm}$ production which can be produced by the weak decays of pions and kaons. The detailed measurements of pion and kaon production cross-section allow to reduce the model dependence of the air shower simulations [74].

The last topic realized by the NA61/SHINE experiment is connected with the neutrino physics studied by the T2K long-baseline neutrino oscillation experiment at the Japan Proton Accelerator Research Complex (J-PARC). The neutrino beams are produced in the J-PARC complex and directed to the Super-Kamiokande detector located 295 km from beam source. The beam parameters are measured by the detectors located in the J-PARC complex (near source of the beam) and then in the Super-Kamiokande detector. The comparison of results allow to study neutrino oscillations[(1)]. The neutrino flux is obtained on the basis of the measurements and Monte Carlo modeling which needs the initial cross sections of pions and kaons. These cross sections are calculated on the basis of the NA61/SHINE measurements for p+C interactions at 31 GeV/c realized using 1 cm graphite target and a 90 cm long T2K replica target [75].

The experiments at Fermilab such as MINERvA, MINOS+ and NOvA have similar problem with neutrino flux calculation as the T2K experiment. These experiments use high-intensity proton beams which are directed to graphite or beryllium targets. Then, the pion and kaon secondaries are used to produce neutrinos. The neutrino flux is also obtained on the basis of measurements and Monte-Carlo simulations which need the initial cross sections of pions and kaons obtained by the NA61/SHINE experiment [76].

After the CERN Long Shutdown 2, which will be finished in 2021, the NA61/SHINE experiment will extend the physics program by studying open charm production, short-lived (including exotic and multistrange) particle production and nuclear fragmentation cross sections to interpret the new data of the AMS and PAMELA experiments [76–78].

3.2 NA61/SHINE in CERN accelerator complex

The NA61/SHINE experiment is located at the North Area of the CERN accelerator complex which is shown in Fig. 3.2. The proton and heavy ion beams, used by the NA61/SHINE detector, are accelerated by the Super Proton Synchrotron which circumference is about 6.8 km [79].

[(1)]Neutrino oscillation is a phenomenon whereby neutrino changes its flavour.

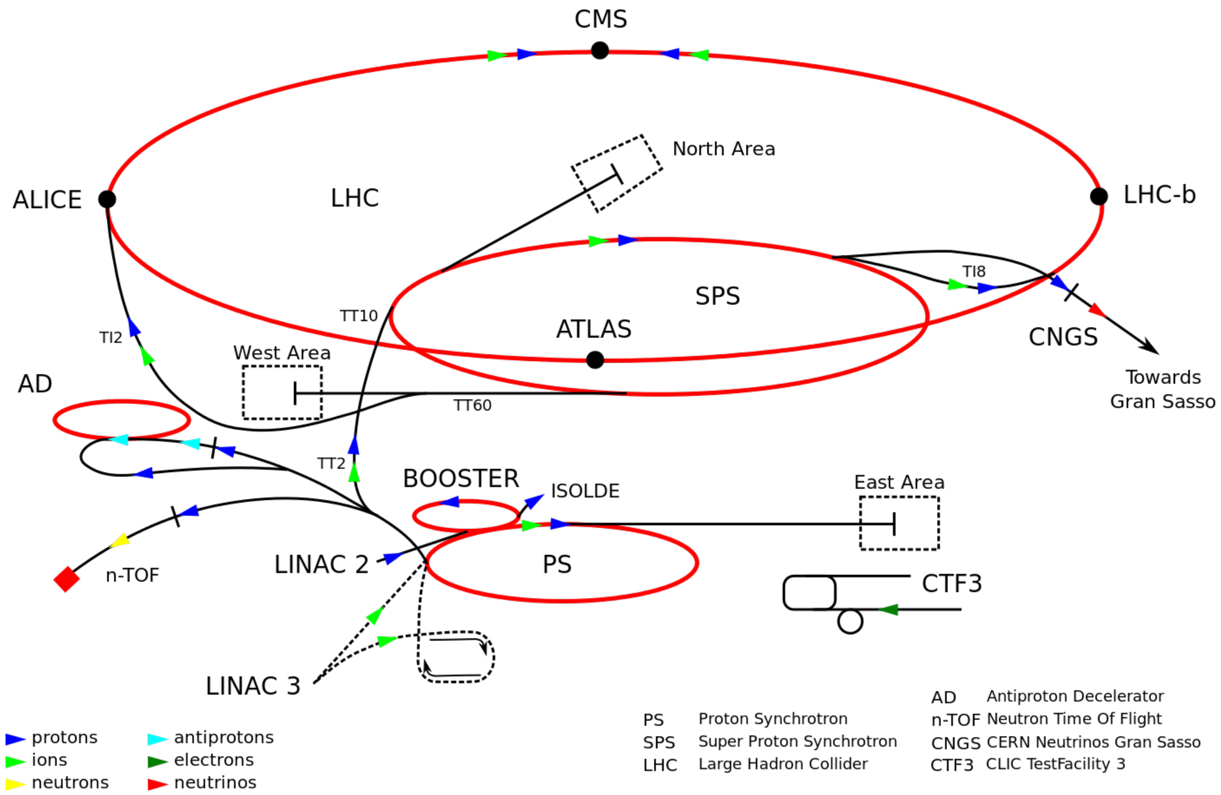

Figure 3.2: The CERN accelerator complex. Figure taken from Ref. [80].

The analysis presented in this thesis was performed using p+p data sets which were collected in 2009, 2010, and 2011. The proton beam was produced in the duo-plasmatron ion source from hydrogen gas (see Fig. 3.4) and then driven to the Radio Frequency Quadrupole RFQ2 in which the beam was focused and accelerated to 759 keV. Next, the prepared proton beam was accelerated in the LINAC 2 to 50 MeV and driven to four rings of the PS Booster in which the beam reached energy about 1.4 GeV. In the next step, the proton beam was accelerated in the Proton Synchrotron, which circumference is about 628 m, until it reached momentum of about 14 GeV/c. Finally, the beam was driven to the SPS and accelerated to 400 GeV/c beam momentum. The primary proton beam was driven to T2 primary target (located 525 m before the NA61/SHINE detector) what allowed to produce secondary proton beam with chosen beam momentum [79].

The ion beam is produced in the Electron Cyclotron Resonance Source (ECR) and driven to the LINAC 3. Then, the initially accelerated ion beam is injected to the Low Energy Ion Ring (LEIR), then to PS, and finally to SPS.

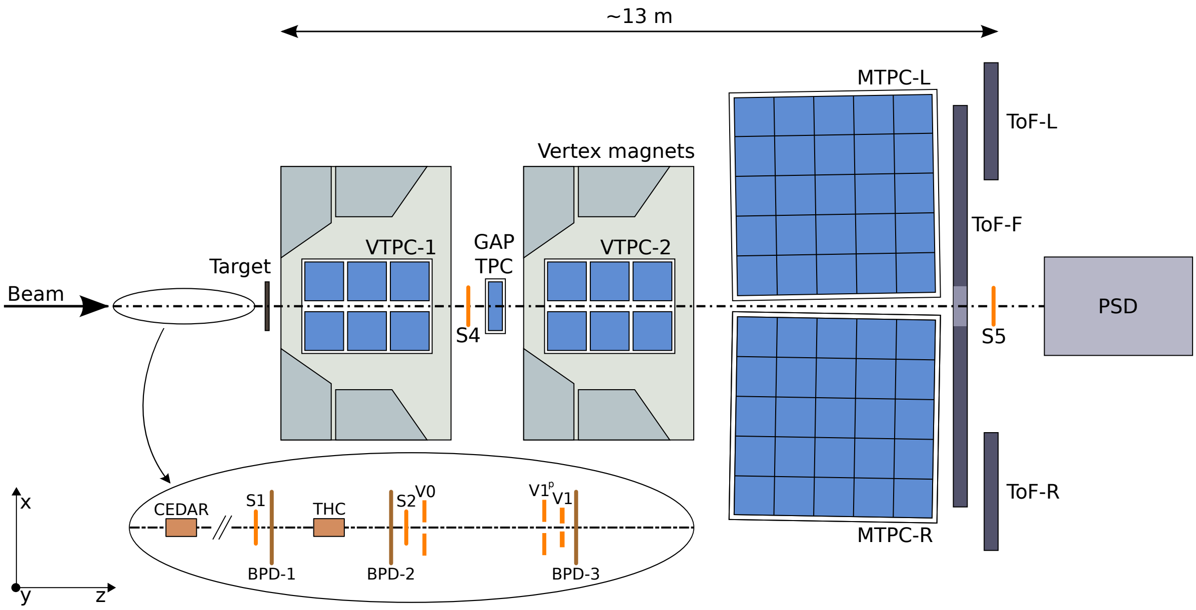

Figure 3.3: The NA61/SHINE detector scheme. Figure taken from Ref. [73].

3.3 NA61/SHINE detector

The NA61/SHINE detector [79], shown in Fig. 3.3, is a large acceptance hadron spectrometer. The first part of the detector is the set of scintillators, Cherenkov counters and the Beam Position Detectors (BPD-1, BPD-2 and BPD-3) which provide the precise time reference and beam position detection. The identification of beam particles is realized by two Cherenkov counters: a CEDAR [81] (or CEDAR-N in case of beam momentum equal 158 GeV/c) and a threshold counter (THC). Signals from the Cherenkov counters allow to reach the purity of beam protons of about 99%. A consistent value for the purity was found by bending the beam into the TPCs with the full magnetic field and using identification based on its specific ionization energy loss dE/dx [82]. The trigger scintillator S4, located between Vertex Time Projector Chambers (VTPC-1 and VTPC-2), allows to select events after collision with the target by the absence of a charged particle hit. The Liquid Hydrogen Target (LHT), used for p+p interactions, is shown in Fig. 3.4. Its length is 20.29 cm and diameter 3 cm [79].

Behind the target, the Time Projector Chambers (TPCs) are located. Two of them (VTPC-1 and VTPC-2) are placed in the magnetic field of two super-conducting dipole magnets which provide the fields 1.5 T and 1.1 T, respectively. This field configuration was used for data taking on p+p interactions at 158 GeV/c. In order to optimize the acceptance of the detector, the field in both magnets was adjusted proportionally to the

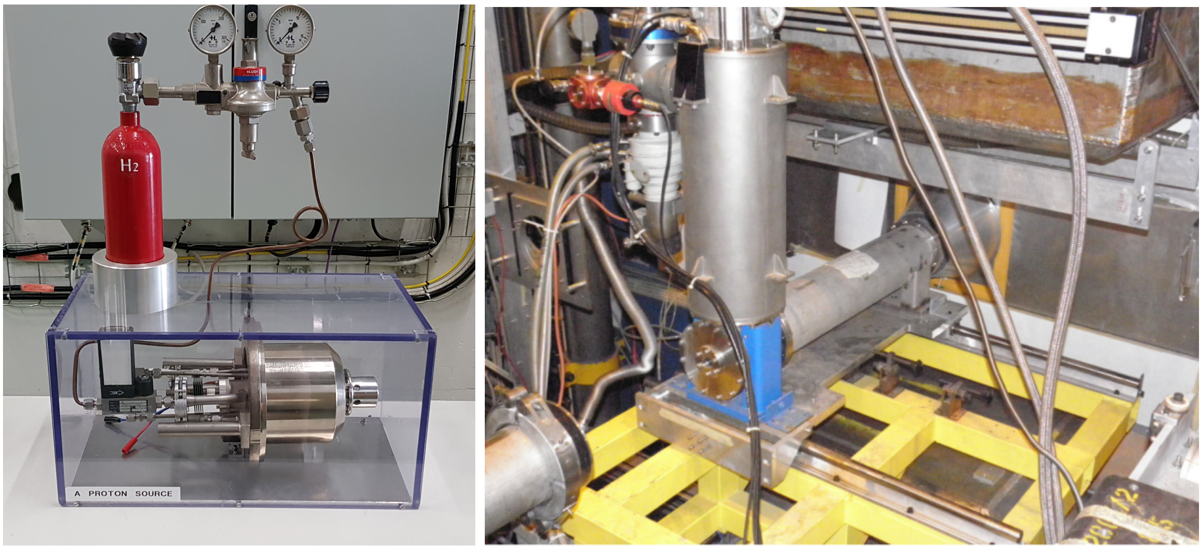

Figure 3.4: Left: The hydrogen gas bottle used to produce the proton beam. Right: The NA61/SHINE Liquid Hydrogen Target (LHT) with the cryogenic system. Figure taken from Ref. [83].

beam momentum. The VTPCs are filled with a mixture of argon and carbon dioxide in 90/10 proportion. They provide up to 72 points in the particle trajectory [79].

The GAP TPC is placed between two VTPCs and is used to register particles produced at small angles [79].

Behind the VTPCs, the two large Main Time Projected Chambers (MTPC-R and MTPC-L) are located, symmetrically to the beam line. The MTPCs are filled by a mixture of argon and carbon dioxide in 95/5 proportion. The trajectories of particles from MTPCs are determined by use of up to 90 points [79]. Particle identification in the TPCs is based on measurements of the specific energy loss ($\mathrm{d}E/\mathrm{d}x$) in the chamber gas and can be augmented by mass measurements using Time-of-Flight (ToF) detectors [79].

The last detector is the Projectile Spectator Detector (PSD) which is a high resolution calorimeter. It allows to measure energy flow around the beam direction, which is given by the projectile spectators for nucleus-nucleus collisions [79].

The photographs of the NA61/SHINE spectrometer are shown in Fig. 3.5.

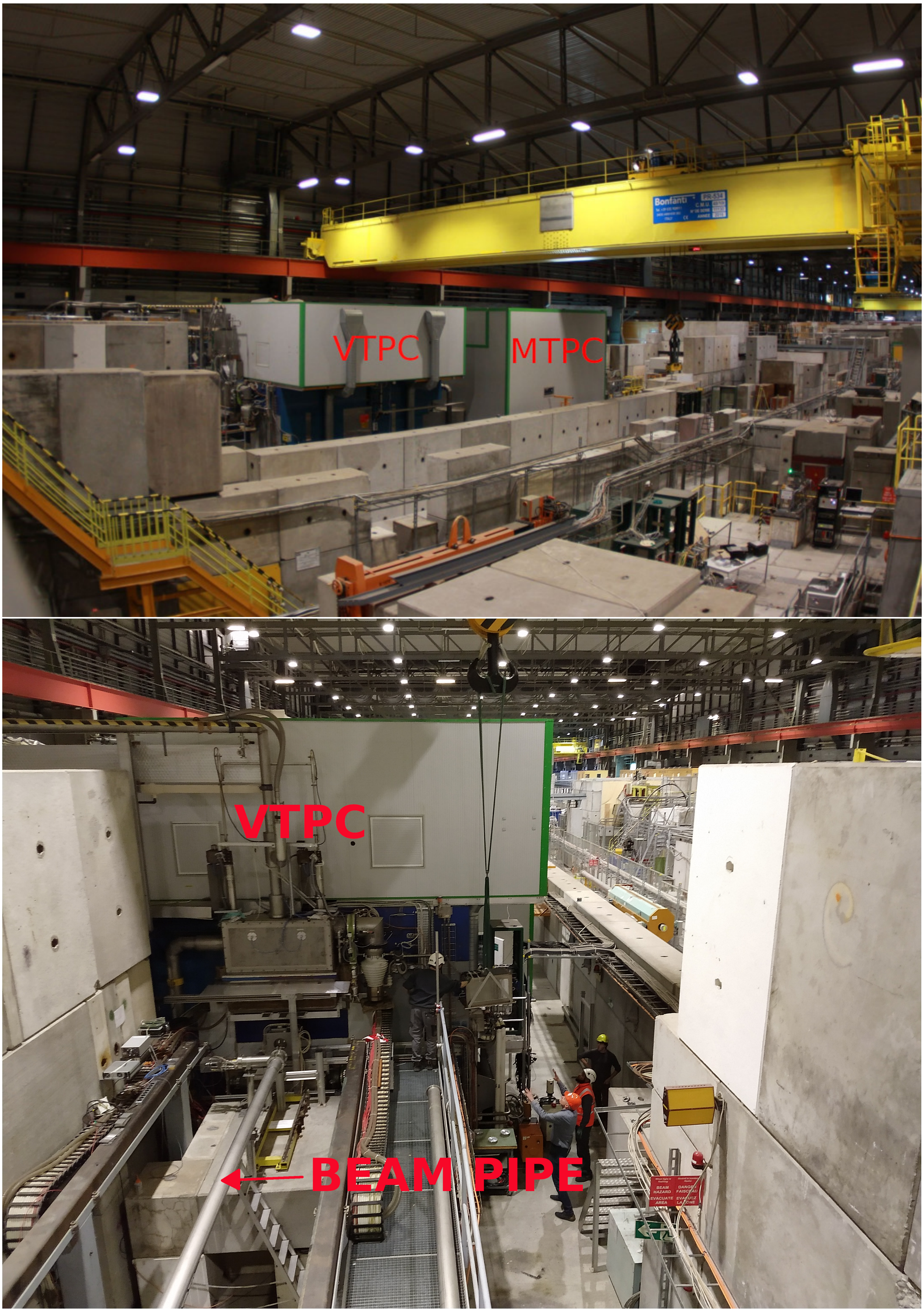

Figure 3.5: The photographs of the NA61/SHINE detector.

Chapter 4

Analysis methodology

The analysis methodology for the measurements of the $K^*(892)^0$ spectra is described in this chapter. It consists of the following steps:

(i) selection of events and tracks (details are described in Sec. 4.2),

(ii) selection of K^+ and π^- candidates based on the measurement of the ionization energy loss $\mathrm{d}E/\mathrm{d}x$ in the gas volume of the TPCs (details are described in Sec. 4.3),

(iii) preparation of invariant mass distributions of $K^+\pi^-$ pairs (details are described in Sec. 4.4),

(iv) preparation of invariant mass distributions of $K^+\pi^-$ pairs for mixed events (details are described in Sec. 4.5.1) and Monte Carlo templates (details in Sec. 4.5.3),

(v) extraction of $K^*(892)^0$ signal (see details in Sec. 4.5.3),

(vi) application of corrections (calculated from simulations) to the raw numbers of $K^*(892)^0$; they include losses of inelastic p+p interactions due to the on-line and off-line event selection as well as losses of $K^*(892)^0$ due to track and pair selection cuts and the detector geometrical acceptance (see details in Sec. 4.7).

The data calibration, simulation procedures, as well as the procedures of vertex and track reconstruction are not discussed in this thesis. The detailed descriptions are available in Refs. [84–86].

4.1 p+p data sets

In 2009, the NA61/SHINE experiment collected data on p+p interactions for five momenta of beam particles: 20, 31, 40, 80, and 158 GeV/c. All interactions were recorded using secondary proton beams and 20 cm long liquid hydrogen target located at z=-580 cm position. During the years 2010–2011, the NA61/SHINE gathered additional high-statistics data at p+p collisions for beam momentum 158 GeV/c.

$\sqrt{s_{NN}}$ (GeV)	8.8	12.3	17.3			
p_{beam}	40 GeV/c	80 GeV/c	158 GeV/c			
			2009	2010	2011	Total
Number of events selected by interaction trigger	4.70M (100%)	3.87M (100%)	2.87M (100%)	37.78M (100%)	11.88M (100%)	52.53M (100%)
Number of events after cuts	1.34M (28.5%)	1.26M (32.6%)	1.26M (43.9%)	19.97M (52.9%)	6.62M (55.7%)	27.85M (53.0%)
Number of tracks	5.17M (100%)	6.38M (100%)	8.62M (100%)	136.58M (100%)	45.48M (100%)	190.68M (100%)
Number of tracks after cuts without dE/dx cut	3.65M (70.6%)	4.68M (73.3%)	4.81M (55.8%)	76.41M (55.9%)	24.91M (54.8%)	106.13M (55.7%)
Number of tracks after all cuts	1.53M (29.6%)	2.13M (33.4%)	2.26M (26.2%)	35.79M (26.2%)	11.74M (25.8%)	49.79M (26.1%)

Table 4.1: Data sets used for the analysis of $K^*(892)^0$ production. The event and track cuts, which were used, are described in Sec. 4.2 and 4.3.

For 158 GeV/c, the three sets of data were taken with similar conditions what is demonstrated by the histograms of the z-position (along the beam line) of the reconstructed p+p interaction vertex (Fig. 4.1). The range of cut on z-position of the main vertex was chosen (black horizontal lines in Fig. 4.1) that way to cover mostly the LHT region and minimize the influence of the off-target interactions. The impact of the off-target interactions was estimated by calculating the ratio of the number of events in the target-removed (empty target) sample to the number of events in the target-inserted sample (see bottom plot in Fig. 4.1) in the range $-590 < z < -572$ cm. The histograms were normalized in the range $-450 < z < -300$ cm. For p+p interactions at 158 GeV/c, this ratio is on the level of 4.8% and therefore, the correction for non-target interactions was neglected. Alternatively, such a correction could be applied by subtracting the resonance yields in the target-removed data (see for example Ref. [84]). However, in this thesis, the analysis of $K^*(892)^0$ meson was done by using the template method (described in Sec. 4.5.3) which cannot be applied to data with small statistics such as the target-removed data recorded by the NA61/SHINE. The standard method also cannot be applied for low-statistics data sets. In order to estimate the systematic biases related to the contamination by off-target interactions the window of z-position of the main vertex was varied (see Sec. 4.10).

Table 4.1 presents the numbers of events recorded with the interaction trigger and the numbers of events after applying the event selection criteria (see Sec. 4.2) for p+p collisions at 40–158 GeV/c beam momenta. The statistics of data for p+p interactions at beam momenta 20–31 GeV/c appeared to be too small to analyse the $K^*(892)^0$ meson production. The drop of the number of events after cuts is caused mainly by BPD reconstruction inefficiencies and off-target interactions accepted by the trigger. The number of tracks, described in the Table. 4.1, corresponds to tracks registered in accepted events (after event cuts). The agreement of the fractions of accepted tracks in the three analyzed data sets for 158 GeV/c confirms the similarity of the data recorded in 2009, 2010, and 2011. For the analysis of $K^*(892)^0$ production these three data sets were combined at the level of preparation of invariant mass distributions (Sec. 4.5.3).

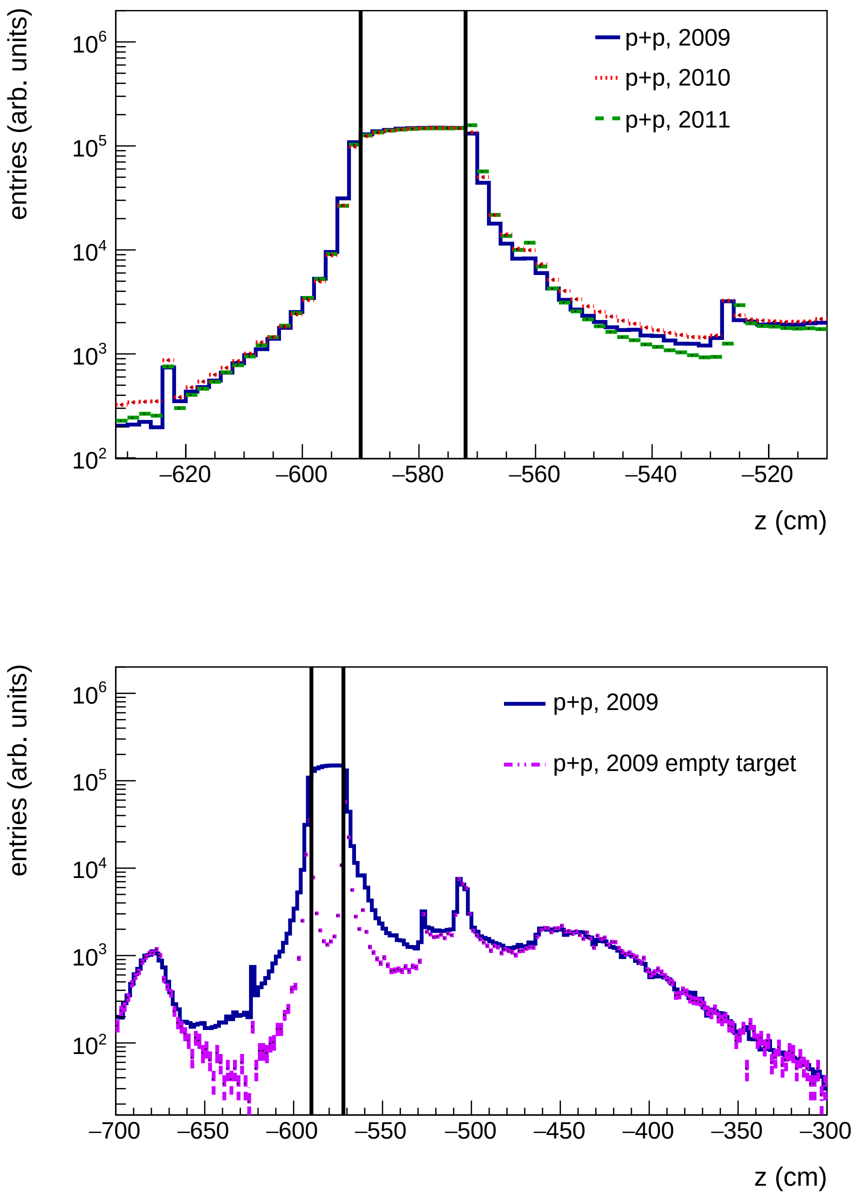

Figure 4.1: Top: Distributions of the z-coordinate of the reconstructed interaction vertex (z) for events recorded with the target inserted (2009, 2010, and 2011 data). Histograms are normalized to the same integral in the range $-590 < z < -572$ cm. Bottom: Distributions of the z-coordinate of the reconstructed interaction vertex for target-inserted (solid histogram) and target-removed (dash-dotted histogram) 2009 data. Histograms are normalized to the same integral in the range $-450 < z < -300$ cm. All event cuts were applied (see Sec. 4.2) with exception of cut (ii) and (v). Black vertical lines indicate the cuts used for the analysis (see Sec. 4.2).

4.2 Event and track selection

The following selection criteria were applied on events:

(i) an interaction was recognized by the trigger logic (see Refs. [84, 85] for detailed description),

(ii) no off-time beam particle was detected within ± 1 μs around the trigger particle,

(iii) the trajectory of the beam particle was measured in at least one of BPD-1 or BPD-2 and in the BPD-3 detector (the nearest to the target),

(iv) the primary interaction vertex fit converged,

(v) the fit of the z-coordinate of the primary p+p interaction vertex (see Fig. 4.1) converged and the value of the fitted z position was between -590 cm and -572 cm, where -580 cm corresponds to the center of the LHT (see Sec. 4.1),

(vi) events with a single, well measured positively charged track with absolute momentum close to the beam momentum ($p > p_{beam} - 1$ GeV/c) were rejected.

The listed event cuts allow to extract well measured inelastic p+p interactions. The elastic interactions are removed by using (iv) and (vi) cuts. The off-target interactions are reduced by (v) cut (see Sec. 4.1). The detailed statistics of events after cuts are shown in Table 4.2.

The tracks were selected according to the following criteria:

(i) the track fit including the interaction vertex converged,

(ii) the total number of reconstructed points on the track should be larger than 30,

(iii) the sum of the number of reconstructed points in VTPC-1 and VTPC-2 was larger than 15 or the number of reconstructed points in the GAP TPC was larger than 4,

(iv) the distance between the track extrapolated to the interaction plane and the interaction point (so-called impact parameter) should be smaller than 4 cm in the horizontal (bending) plane and 2 cm in the vertical (drift) plane,

Cuts	p_{beam} (GeV/c)				
	40	80	158		
			2009	2010	2011
(i)	$4.70 \cdot 10^6$ (100%)	$3.87 \cdot 10^6$ (100%)	$2.87 \cdot 10^6$ (100%)	$37.78 \cdot 10^6$ (100%)	$11.88 \cdot 10^6$ (100%)
(ii)	$4.47 \cdot 10^6$ (95.1%)	$3.80 \cdot 10^6$ (98.2%)	$2.83 \cdot 10^6$ (98.6%)	$37.38 \cdot 10^6$ (98.9%)	$11.74 \cdot 10^6$ (98.8%)
(iii)	$3.48 \cdot 10^6$ (74.0%)	$2.53 \cdot 10^6$ (65.4%)	$2.11 \cdot 10^6$ (73.5%)	$34.06 \cdot 10^6$ (90.2%)	$10.44 \cdot 10^6$ (87.9%)
(iv)	$2.14 \cdot 10^6$ (45.5%)	$1.90 \cdot 10^6$ (49.1%)	$1.84 \cdot 10^6$ (64.1%)	$29.27 \cdot 10^6$ (77.5%)	$9.44 \cdot 10^6$ (79.5%)
(v)	$1.35 \cdot 10^6$ (28.7%)	$1.26 \cdot 10^6$ (32.6%)	$1.26 \cdot 10^6$ (43.9%)	$19.97 \cdot 10^6$ (52.9%)	$6.62 \cdot 10^6$ (55.7%)
(vi)	$1.34 \cdot 10^6$ (28.5%)	$1.26 \cdot 10^6$ (32.6%)	$1.26 \cdot 10^6$ (43.9%)	$19.97 \cdot 10^6$ (52.9%)	$6.62 \cdot 10^6$ (55.7%)

Table 4.2: The statistics of events after cuts.

(v) the track total momentum (in the laboratory reference system) should be in the range $p_{lab} \leq 35$ GeV/c (for 40 GeV/c beam momentum), $p_{lab} \leq 74$ GeV/c (for 80 GeV/c beam momentum) or $3 \leq p_{lab} \leq 158$ GeV/c (for 158 GeV/c beam momentum),

(vi) the track transverse momentum was required to be smaller than 1.5 GeV/c,

(vii) dE/dx track cuts were applied to select K^+ and π^- candidates (see Sec. 4.3).

These cuts ensure high reconstruction efficiency, reduction of tracks from secondary interactions and weak decays, and proper identification of tracks (see Sec. 4.3). The detailed statistics of tracks after cuts are shown in Table 4.3.

Cuts	p_{beam} (GeV/c)				
	40	80	158		
			2009	2010	2011
(i)	$5.17 \cdot 10^6$ (100%)	$6.38 \cdot 10^6$ (100%)	$8.62 \cdot 10^6$ (100%)	$136.58 \cdot 10^6$ (100%)	$45.48 \cdot 10^6$ (100%)
(ii)	$4.44 \cdot 10^6$ (85.9%)	$5.51 \cdot 10^6$ (86.4%)	$8.34 \cdot 10^6$ (96.8%)	$132.44 \cdot 10^6$ (97.0%)	$43.50 \cdot 10^6$ (95.6%)
(iii)	$4.04 \cdot 10^6$ (78.1%)	$5.06 \cdot 10^6$ (79.3%)	$8.08 \cdot 10^6$ (94.3%)	$129.17 \cdot 10^6$ (94.6%)	$42.31 \cdot 10^6$ (93.0%)
(iv)	$3.69 \cdot 10^6$ (71.4%)	$4.70 \cdot 10^6$ (73.7%)	$7.65 \cdot 10^6$ (88.4%)	$121.17 \cdot 10^6$ (88.7%)	$39.59 \cdot 10^6$ (87.0%)
(v)	$3.65 \cdot 10^6$ (70.6%)	$4.68 \cdot 10^6$ (73.4%)	$4.81 \cdot 10^6$ (55.8%)	$76.41 \cdot 10^6$ (55.9%)	$24.91 \cdot 10^6$ (54.8%)
(vi)	$3.65 \cdot 10^6$ (70.6%)	$4.68 \cdot 10^6$ (73.4%)	$4.81 \cdot 10^6$ (55.8%)	$76.41 \cdot 10^6$ (55.9%)	$24.91 \cdot 10^6$ (54.8%)

Table 4.3: The statistics of tracks after cuts.

4.3 Identification based on energy loss measurement (dE/dx)

The NA61/SHINE detector includes TPCs chambers which measure the ionization energy loss (dE/dx) in the gas, and the Time of Flight (ToF) detectors. At relativistic rise of the dE/dx at large momenta, the identification of charged particles can be performed based on dE/dx bands only. The dE/dx bands for different particle species overlap at the lower momentum region. The possibility of misidentification of particles is especially visible for p+p interactions at 158 GeV/c. For this reason, the additional track cut (v) ($p_{lab} \geq 3$ GeV/c for 158 GeV/c) was applied to reduce particles from overlapping region. The upper limit is needed to eliminate the region where dust particles are mostly registered. This limit is equal to $p_{beam} - 5$ GeV/c for 40 GeV/c, $p_{beam} - 6$ GeV/c for 80 GeV/c, and p_{beam} for 158 GeV/c.

The ToF detectors can be additionally used to identify particles with low momenta. The analysis on K^+ and π^- spectra (see Ref. [35]) showed that the results obtained for two different identification methods (dE/dx only or tof+dE/dx measurements) overlap in the common kinematic region. The results, obtained using identified particles based on TPCs measurements only, have smaller uncertainties (more details in Ref. [35]). The statistics of K^+ and π^- candidates is especially important to study the rare $K^*(892)^0$ meson. The misidentified particles give contribution to the background in $m_{K^+\pi^-}$[(1)] yield, but the background is removed by using different techniques (see Sec. 4.5.3).

The ionization energy losses as a function of total momentum in the laboratory reference system (p_{lab}) are shown in Figs. 4.2, 4.3, and 4.4 for positively and negatively charged particles, separately (upper plots). For fixed p_{lab}, the dE/dx distributions of kaons and pions can be described by the Gaussian functions. The standard deviations (σ) of Gaussian fits were determined as average values for different total momentum and transverse momentum bins. Since only small variations of σ were observed for different bins and beam momenta, fixed values $\sigma = 0.044$ for K^+ and $\sigma = 0.052$ for π^- were used. The K^+ and π^- candidates were selected by requiring their dE/dx values to be within 1.5σ and 3.0σ around their nominal Bethe-Bloch values, respectively. The dE/dx distributions as functions of p_{lab} for selected K^+ and π^- candidates are shown in the bottom panels of Figs. 4.2, 4.3, and 4.4.

[(1)] The invariant mass of $K^+\pi^-$ pairs ($m_{K^+\pi^-}$) is defined in Eq. 4.1.

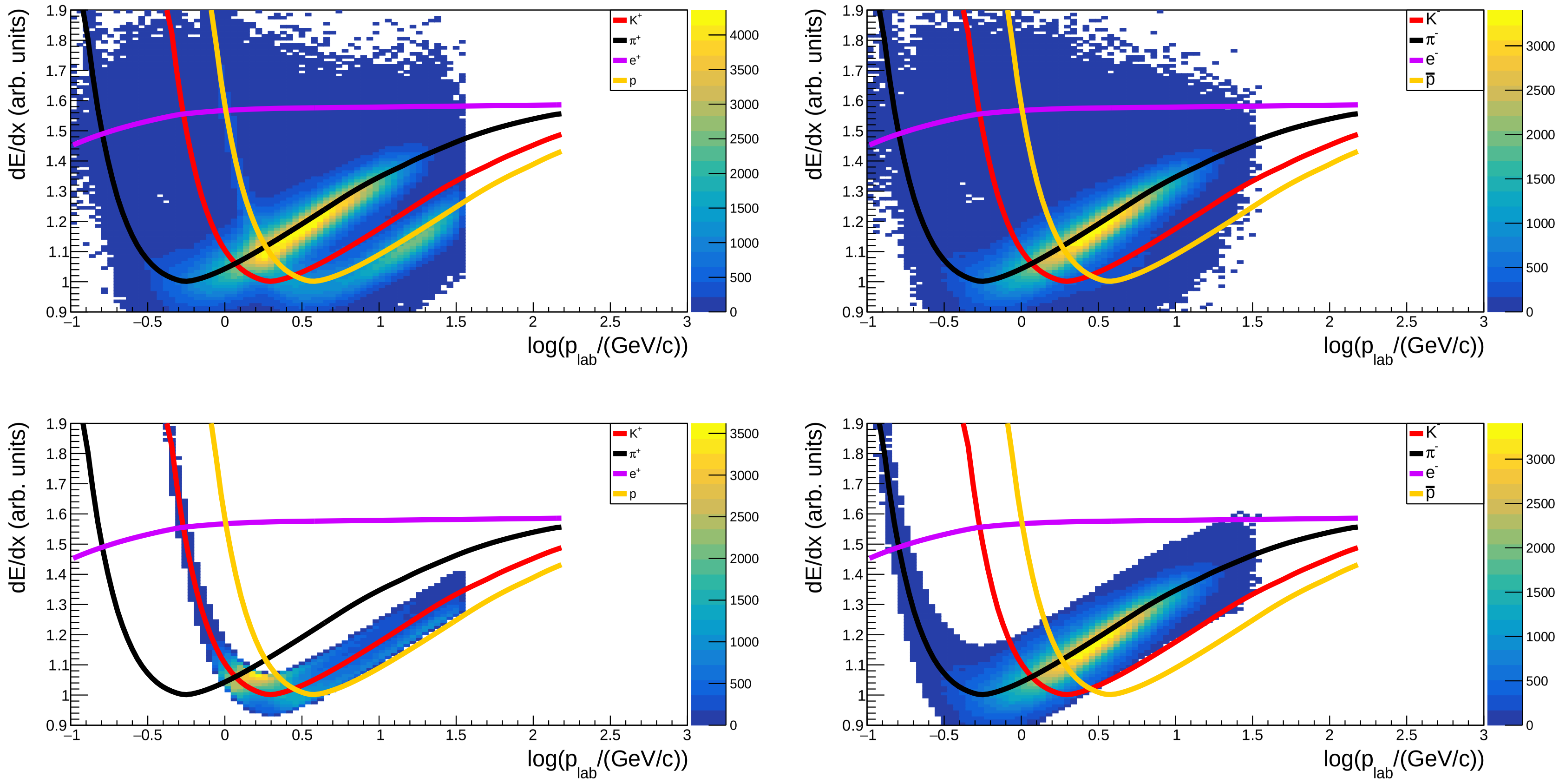

Figure 4.2: Top: The dE/dx distribution as a function of $\log(p_{lab}/(\mathrm{GeV}/c))$ for positively (left) and negatively (right) charged particles after all track cuts for p+p interactions at 40 GeV/c beam momentum. The lines represent Bethe-Bloch curves. Bottom: K^+ candidates (left) and π^- candidates (right) after dE/dx cuts.

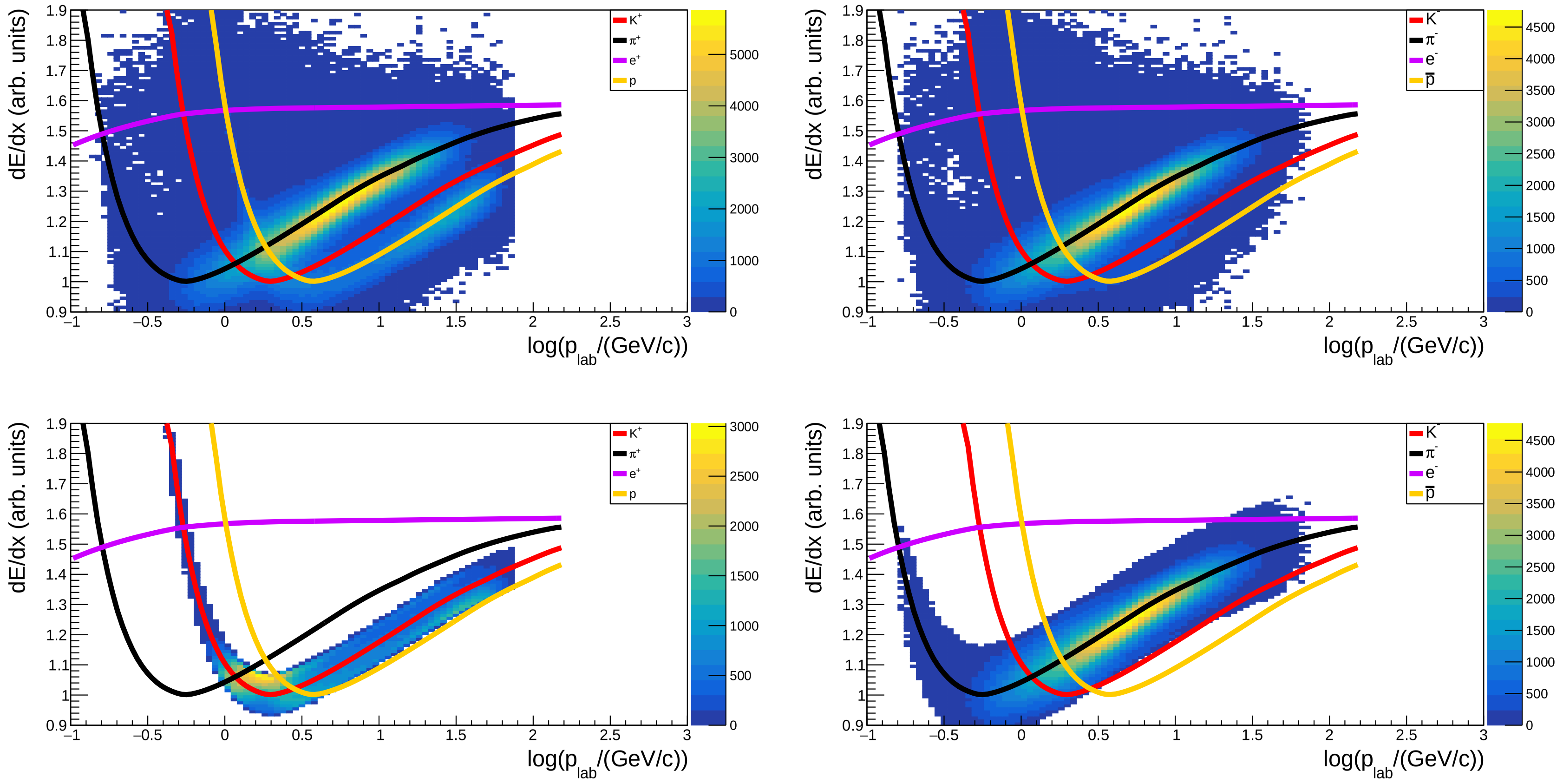

Figure 4.3: Top: The dE/dx distribution as a function of $\log(p_{lab}/(\mathrm{GeV}/c))$ for positively (left) and negatively (right) charged particles after all track cuts for p+p interactions at 80 GeV/c beam momentum. The lines represent Bethe-Bloch curves. Bottom: K^+ candidates (left) and π^- candidates (right) after dE/dx cuts.

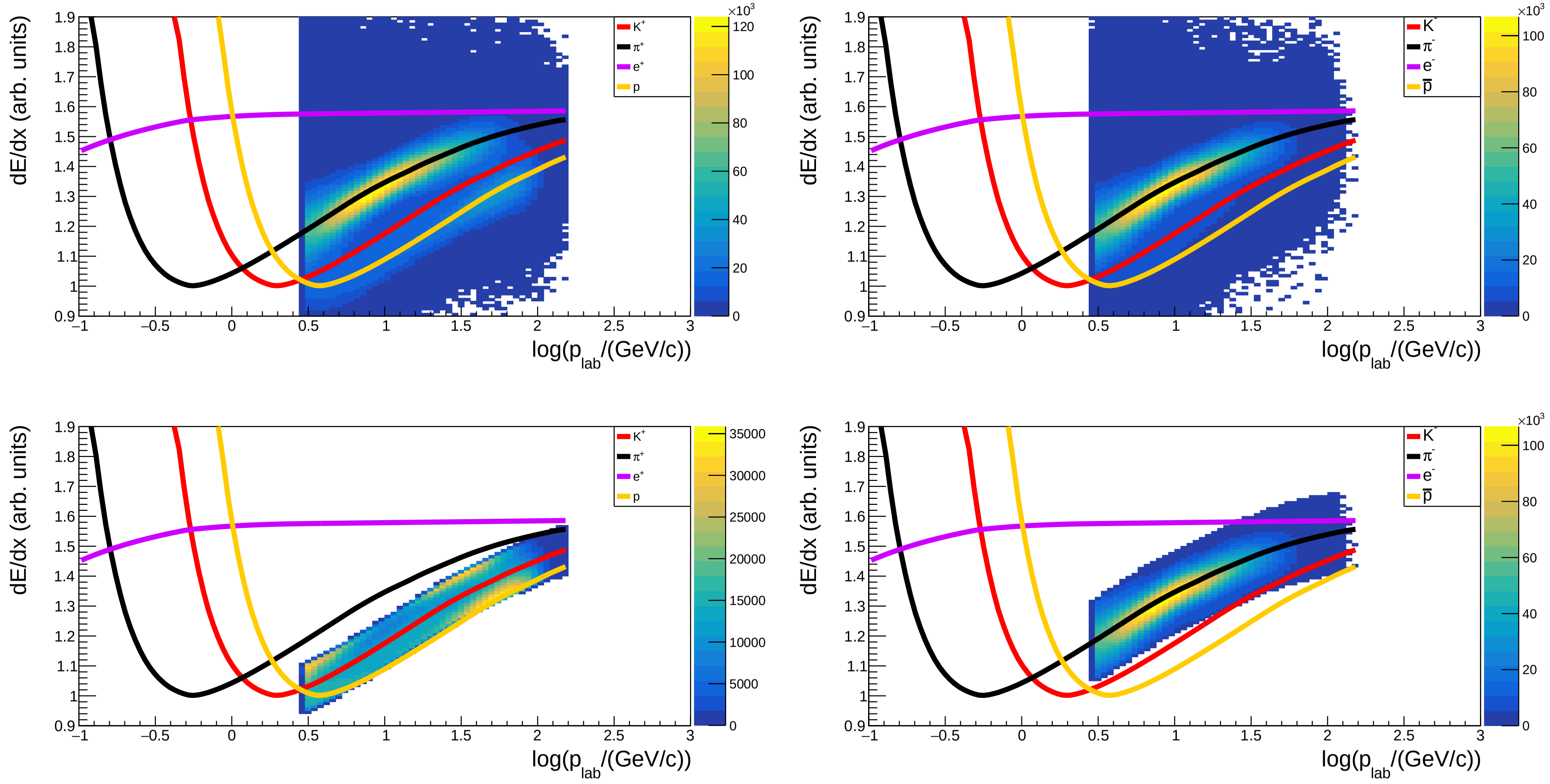

Figure 4.4: Top: The $\mathrm{d}E/\mathrm{d}x$ distribution as a function of $\log(p_{lab}/(\mathrm{GeV}/c))$ for positively (left) and negatively (right) charged particles after all track cuts for p+p interactions at 158 GeV/c beam momentum. The lines represent Bethe-Bloch curves. Bottom: K^+ candidates (left) and π^- candidates (right) after $\mathrm{d}E/\mathrm{d}x$ cuts.

4.4 Invariant mass distribution

The $K^*(892)^0$ lifetime is of about 4 fm/c, so this meson decays in the main interaction vertex. The dominant decay channel is $K^*(892)^0 \rightarrow K^+\pi^-$ (BR=2/3). The another decay channel is $K^*(892)^0 \rightarrow K^0\pi^0$ (BR=1/3). It is not possible to distinguish whether K^+ or π^- particle, produced in the collision, came from direct production or from resonance decay. Therefore, the indirect measurement of $K^*(892)^0$ meson is based on the *invariant mass method*.

The invariant mass is defined as:

$$m_{K^+\pi^-} = \sqrt{(E_{K^+} + E_{\pi^-})^2 - (\overrightarrow{p_{K^+}} + \overrightarrow{p_{\pi^-}})^2}, \tag{4.1}$$

where E_{K^+} and E_{π^-} represent the total energies and $\vec{p_{K^+}}$ and $\vec{p_{\pi^-}}$ represent the momenta vectors of daughter particles from $K^*(892)^0$ decay.

The invariant mass is calculated for all combinations of K^+ and π^- candidates from the same event. These values fill the histogram. The example invariant mass distributions are shown in Fig. 4.5. According to the quantum mechanics, the energy and lifetime of unstable particles are correlated by the uncertainty principle so that the mass of $K^*(892)^0$ meson is visible as a peak on invariant mass distribution of $K^+\pi^-$ pairs [39]. The large combinatorial background on the invariant mass distribution should be removed in order to obtain the raw number of $K^*(892)^0$. The possible methods of removing background are described in Sec. 4.5.1 and 4.5.3.

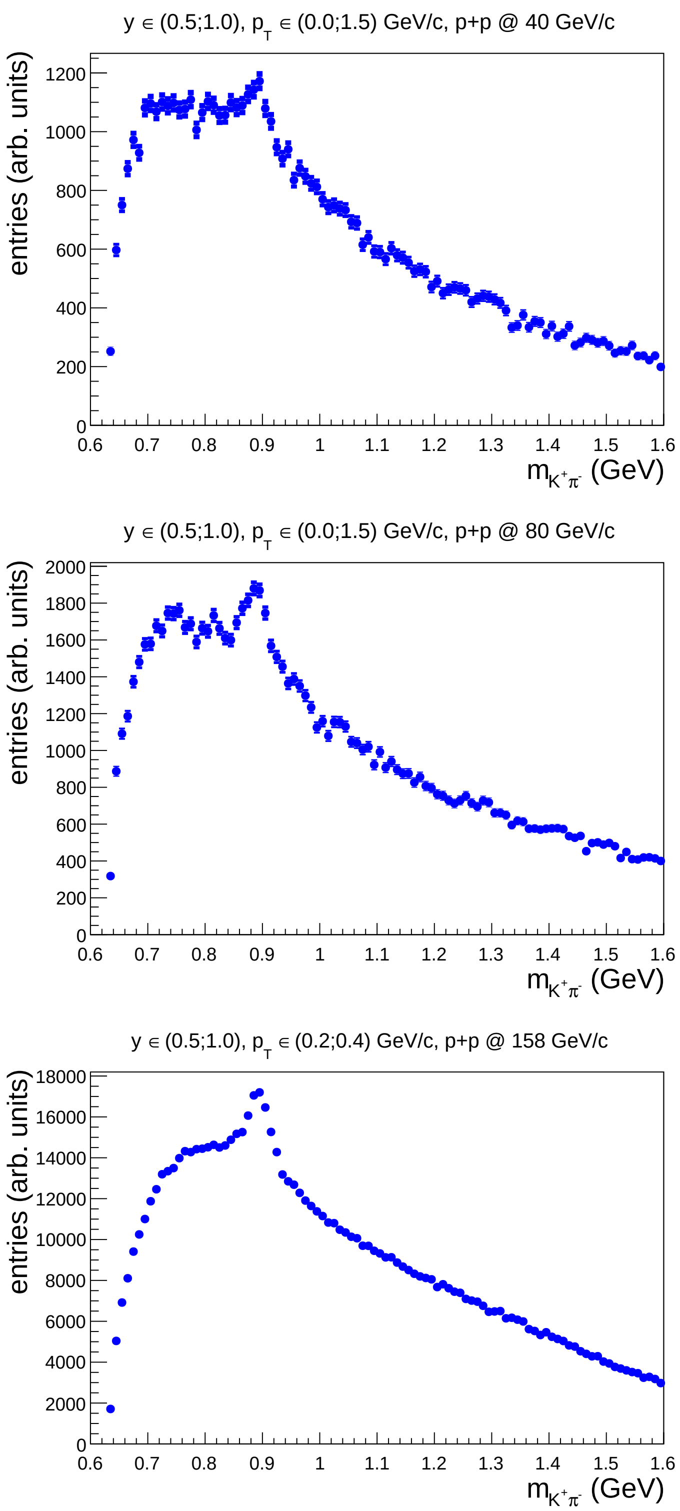

Figure 4.5: The invariant mass distributions of $K^+\pi^-$ pairs in example rapidity (y) and transverse momentum (p_T) bins for p+p interactions at beam momenta 40 (top), 80 (middle), and 158 (bottom) GeV/c. The bars indicate statistical uncertainties. The rapidity is defined as $y = \frac{1}{2}\ln\frac{E+p_L}{E-p_L}$, where E is the total energy and p_L is the particle momentum parallel to the beam direction. All rapidity values shown in this thesis are calculated in the collision center-of-mass reference system.

4.5 Signal extraction

The large, combinational background is usually removed based on two methods: *standard method* or *cocktail fit*. The first one is based on *mixing technique* (see Sec. 4.5.1) and is commonly used to analyze different kinds of resonances. The second method is used to analyze mostly the $\rho(770)^0$ meson in such experiments as: ALICE and STAR (see Sec. 4.5.2).

4.5.1 Standard method of signal extraction

The *standard method* of signal extraction is based on *mixing technique* in which the invariant mass distribution is prepared for $K^+\pi^-$ pairs originating from different events. These distributions are shown as red points in Fig. 4.6 (left plots). The mixed events histogram is normalized to the same number of pairs as in real data histogram (blue points in Fig. 4.6, left plots) in range $0.6 \leq m_{K^+\pi^-} \leq 1.6$ GeV.

The background described by the mixed events is subtracted from data points and the result is shown as blue points in Fig. 4.6 (right plots). There is still residual background in invariant mass distributions, especially for low $m_{K^+\pi^-}$ values. This residual background probably comes from the products of other resonance decays, which are not properly accounted for by the event-mixing, and should be subtracted. The $K^*(892)^0$ signal is obtained by performing fit with Eq. 4.2 (marked as *total fit 2* in Fig. 4.6 – right plots) to points. The fitted function consists of signal (Breit-Wigner distribution – BW) and residual background (second order polynomial curve):

$$f(m_{K^+\pi^-}) = d \cdot (m_{K^+\pi^-})^2 + e \cdot (m_{K^+\pi^-}) + f + g \cdot BW(m_{K^+\pi^-}), \tag{4.2}$$

where d, e, f, and g are free parameters of the fit, and the BW component is described by Eq. 4.3:

$$BW(m_{K^+\pi^-}) = A \cdot \frac{\frac{1}{4} \cdot \Gamma_{K^*}^2}{(m_{K^+\pi^-} - m_{K^*})^2 + \frac{1}{4}\Gamma_{K^*}^2}, \tag{4.3}$$

where A is the normalization factor, and m_{K^*} and Γ_{K^*} are also fitted. The initial values of the mass (m_{K^*}) and width (Γ_{K^*}) parameters of $K^*(892)^0$ were taken from the Particle Data Group (PDG): $m_{K^*} = m_0 = 0.89555$ GeV and $\Gamma_{K^*} = \Gamma_0 = 0.0473$ GeV [11].

The residual background description based on a second order polynomial curve is shown as red lines (*polynomial background*) in Fig. 4.6 (right plots). Finally, the raw

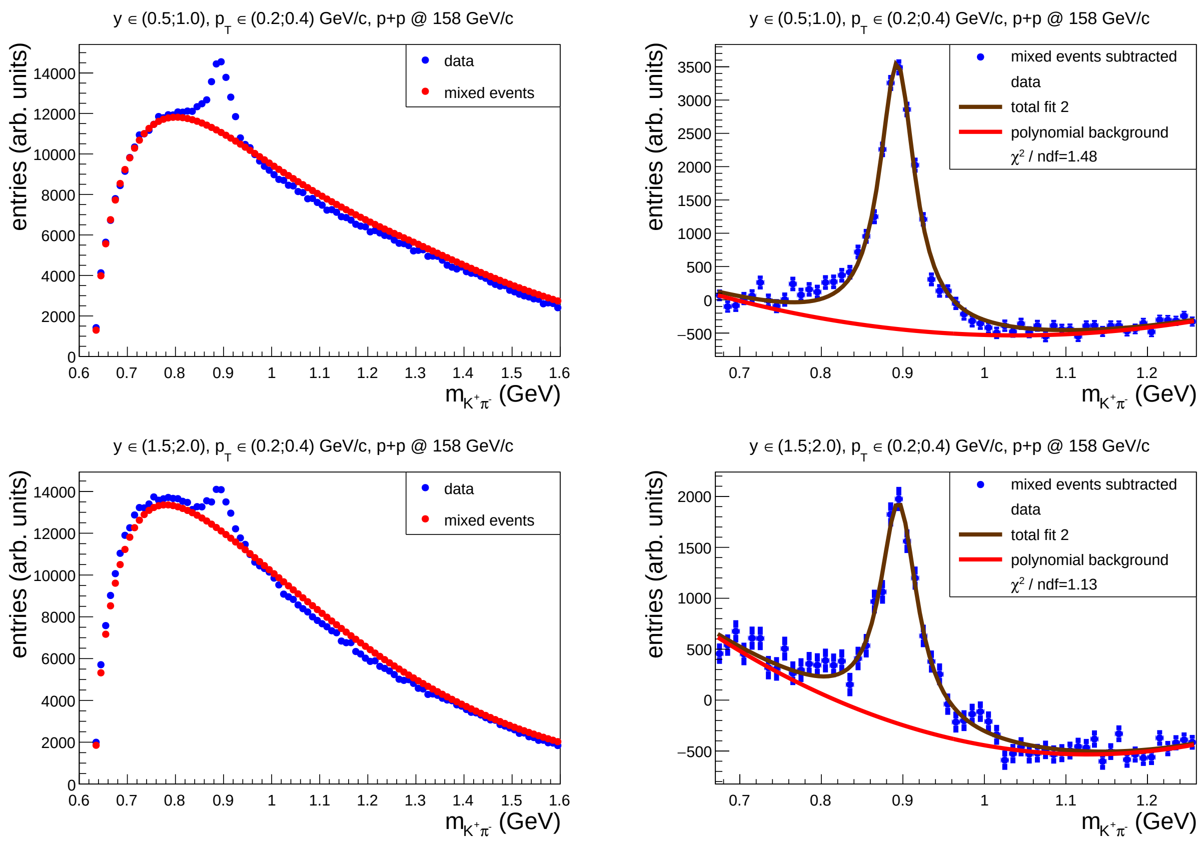

Figure 4.6: The example of the procedure of signal extraction (standard method) for $K^*(892)^0$ in rapidity and transverse momentum bins: $0.5 < y < 1.0$, $0.2 < p_T < 0.4$ GeV/c (top plots) and $1.5 < y < 2.0$, $0.2 < p_T < 0.4$ GeV/c (bottom plots) for p+p collisions at 158 GeV/c. All rapidity values are given in the center-of-mass reference system. See the text for details.

number of $K^*(892)^0$ mesons may be obtained essentially as the difference between *total fit 2* and *polynomial background*.

The above method of $K^*(892)^0$ meson extraction is commonly used by many experiments such as NA49, ALICE, and STAR. The main disadvantage of this method is quite a large residual background which increases with decreasing pair invariant mass.

4.5.2 Coctail fit

The cocktail fit method is used to extract $\rho(770)^0$ signal from invariant mass distributions of $\pi^+\pi^-$ pairs. It was used by the NA61/SHINE [87], ALICE [88], and STAR [89] experiments. This method starts with preparing background description based on "standard" mixing technique (discussed in Sec. 4.5.1) or "charge" mixing method. The second

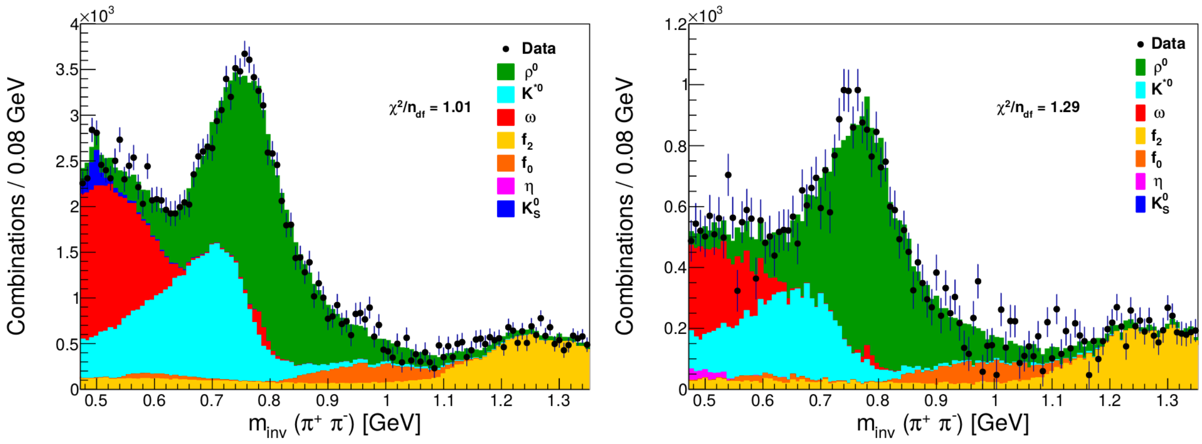

Figure 4.7: The example of cocktail fit prepared for π^-+C interactions at 158 GeV/c (left) and 350 GeV/c (right), in x_F range $0.3 < x_F < 0.4$. Feynman x_F variable is a ratio of the longitudinal momentum of particle to the maximum momentum that this particle can reach (both in the center-of-mass reference system). Green histogram is defined by Eq. 4.4. Figure taken from Ref. [87].

method is based on preparing the invariant mass distribution of $\pi^+\pi^+$ and $\pi^-\pi^-$ pairs from the same event. The background is then subtracted from invariant mass distribution of $\pi^+\pi^-$ pairs and the example result is shown as black points in Fig. 4.7.

In this case, the residual background is huge and an additional description is needed. For this reason, the invariant mass distributions of $\pi^+\pi^-$ pairs are prepared, in which two pions come from different resonances, for example $\pi^+_{\rho^0}\pi^-_{\omega}$. Such invariant mass histograms are prepared based on reconstructed Monte Carlo (MC) data, separately for different resonances. The same list of event and track cuts should be applied to reconstructed MC data as for real data before preparing $m_{\pi^+\pi^-}$ histograms. The fit to black points in Fig. 4.7 is performed using Eq. 4.4:

$$f(m_{\pi^+\pi^-}) = e \cdot T_{mix}(m_{\pi^+\pi^+/\pi^-\pi^-}) + \sum_i f_i T_i(m_{\pi^+\pi^-}), \tag{4.4}$$

where e, f_i are free parameters of the fit, $T_{mix}(m_{\pi^+\pi^+/\pi^-\pi^-})$ is charge mixing background, and $T_i(m_{\pi^+\pi^-})$ are invariant mass histograms for different resonances prepared by using reconstructed Monte Carlo data.

The example fits (green histograms) are shown in Fig. 4.7, where invariant mass histograms for different resonances are marked by using different colors (for more details see Ref. [87]).

The cocktail fit (Eq. 4.4) allows to describe background better than in the standard (mixing) method. Moreover, it shows the estimated contribution of other resonance decay products in invariant mass distributions of $\pi^+\pi^-$ pairs. The fit can be performed when the components (T_i) have unique shapes which is true for $\pi^+\pi^-$ decay channel. Unfortunately, this method does not work properly for different decay channels e.g. $K^+\pi^-$ because the separate T_i components have too similar shapes. Moreover, the fit can be done incorrectly when the real values of masses and widths of resonances are different than the values used while preparing MC data.

4.5.3 Template method of signal extraction

The standard method (Sec. 4.5.1) allows to study $K^*(892)^0$ but it has a poor description of residual background. On the other hand, the cocktail fit allows to obtain a better description of the background but it does not work properly for the decay channels other than $\pi^+\pi^-$. This problem was solved by introducing a modified version of the cocktail fit which is called the *template method*.

In this method, the invariant mass spectra for the data were fitted with a function given by Eq. 4.5:

$$f(m_{K^+\pi^-}) = a \cdot T_{res}^{MC}(m_{K^+\pi^-}) + b \cdot T_{mix}^{DATA}(m_{K^+\pi^-}) + c \cdot BW(m_{K^+\pi^-}). \tag{4.5}$$

This function consists of the background (T_{res}^{MC} and T_{mix}^{DATA}) and signal (BW) descriptions. The first component of the background is T_{res}^{MC} template which is prepared on the basis of reconstructed Monte Carlo data. It is the shape of the background which describes the contribution of $K^+\pi^-$ pairs originating from:

(i) combination of tracks that came from decays of resonances different than $K^*(892)^0$, for example one track from a ρ^0 meson and one from a K^{*+} meson,

(ii) combination of tracks where one came from decay of a resonance and one came from direct production in the primary interaction.

The MC data, used to prepare the T_{res}^{MC} templates, were generated by the EPOS 1.99 [90] hadronic interaction model using the CRMC 1.4 package [91]. These data were processed by the full NA61/SHINE detector simulation chain and then through the same

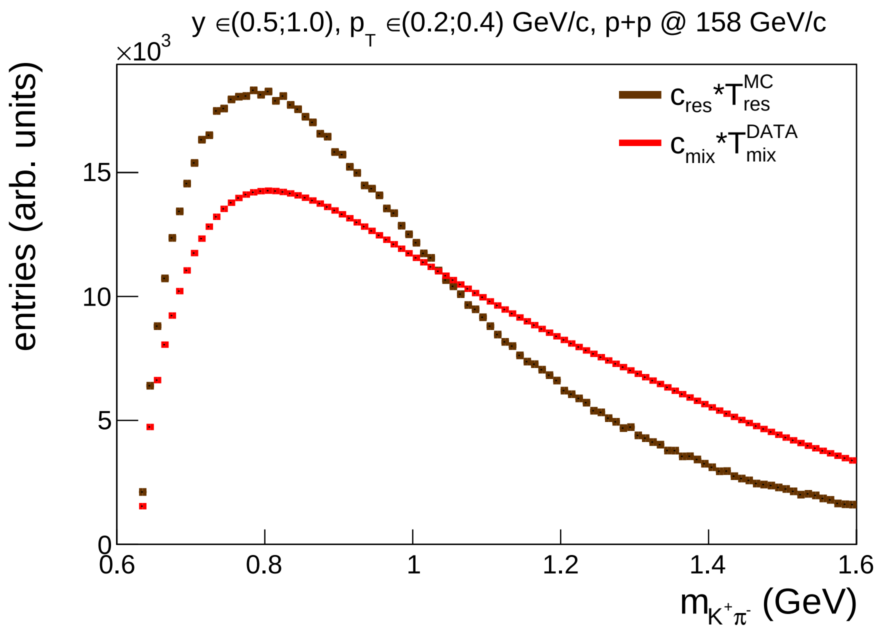

Figure 4.8: The comparison of T^{MC}_{res} and T^{DATA}_{mix} template shapes. The templates are normalized to have the same number of pairs as the real data histogram (see blue points in Figs. 4.9 and 4.10, top, right). The c_{res} and c_{mix} are normalization constants for T^{MC}_{res} and T^{DATA}_{mix} templates, respectively.

reconstruction routines as the data. The next step was applying the same event and track selection criteria to the MC events as were used for the real data. Because the simulation maintains the history of particle production, it enables accurate identification of the particles and creation of proper templates based on the particle origins.

The event generator was chosen based on the NA61/SHINE results on hadron production. The experimental results were very well reproduced by the EPOS 1.99 and FLUKA2008 models [35, 74, 84, 92–94]. The NA61/SHINE Monte Carlo group develops and supports software based on EPOS 1.99 model, so this model was chosen as a primary event generator. If the chosen EPOS 1.99 model did not describe the resonance background well, the fit would be done incorrectly, which would result in large χ^2/ndf value. Fortunately, such situations were not observed for $K^*(892)^0$ meson analysis.

The response of the detector is simulated based on the GEANT 3.21 package [95], so the limited acceptance of the NA61/SHINE detector is also included in the reconstructed Monte Carlo data used to prepare the T^{MC}_{res} templates.

The T^{DATA}_{mix} template describes the combinational background. This template is prepared in the same way as mixed events histogram (see Sec. 4.5.1). The comparison of background template shapes is shown in Fig. 4.8. The T_{res}^{MC} and T_{mix}^{DATA} histograms in the fit function (Eq. 4.5) were normalized to have the same numbers of pairs as the real data histogram in the invariant mass range from 0.6 to 1.6 GeV. The signal (BW), in Eq. 4.5, is described using the Breit-Wigner distribution (Eq. 4.3).

Finally, the symbols a, b, and c in Eq. 4.5 are the normalization parameters of the fit and fulfill the equation: $a + b + c = 1$. These parameters describe the contributions of T_{res}^{MC}, T_{mix}^{DATA}, and BW to the invariant mass spectra.

Both the template and the data histograms were computed in bins of rapidity y (calculated in the center-of-mass reference system) and transverse momentum p_T.

Figures 4.9 and 4.10 show the comparison of the standard (left plots) and template (right plots) methods used for extracting the signal of $K^*(892)^0$ meson. Note, that Figs. 4.9 and 4.10 (left) show the same data as in Fig. 4.6. The first step is similar in both methods and relies on preparing invariant mass spectra for all $K^+\pi^-$ pairs within the same event (blue points in top plots). The next steps, for the standard method, are described in Sec. 4.5.1. In case of the template method, the data points in Figs. 4.9 and 4.10 (top, right) are fitted with a function given by Eq. 4.5 (brown curve, *total fit 1*). The background is described by two templates: T_{res}^{MC} and T_{mix}^{DATA} (red line, *fitted background*). Both fits (brown and red curves) were performed in the invariant mass range from 0.66 GeV to 1.26 GeV. It is seen that Eq. 4.5 (without BW component) describes the background much better than only mixed events (Figs. 4.9 and 4.10, top, left). After the background subtraction (bottom, right plots, see Eq. 4.6) the residual background is much less significant than in the case of the standard method (Figs. 4.9 and 4.10, bottom, left). The effect is much more visible for smaller statistics bins (see Fig. 4.10). The residual background in Figs. 4.9 and 4.10 (bottom, right) is removed in the same way as in the standard method, it is by fitting data with a function described by Eq. 4.2. The brown lines in Figs. 4.9 and 4.10 (bottom, right), *total fit 2*, were obtained using Eq. 4.2 and the red lines (*polynomial background*) represent Eq. 4.2 without BW component.

The uncorrected number of $K^*(892)^0$ mesons (for each y and p_T bin) is obtained as the integral over the BW signal of *total fit 2* in Figs. 4.9 and 4.10 (bottom, right). The integral is calculated in the mass window $m_0 \pm 4\Gamma_0$. Finally, the mass and width of the $K^*(892)^0$ are obtained from parameters of the *total fit 2* within $m_o \pm 4\Gamma_o$. These two values are included in the BW distribution (see Eq. 4.3).

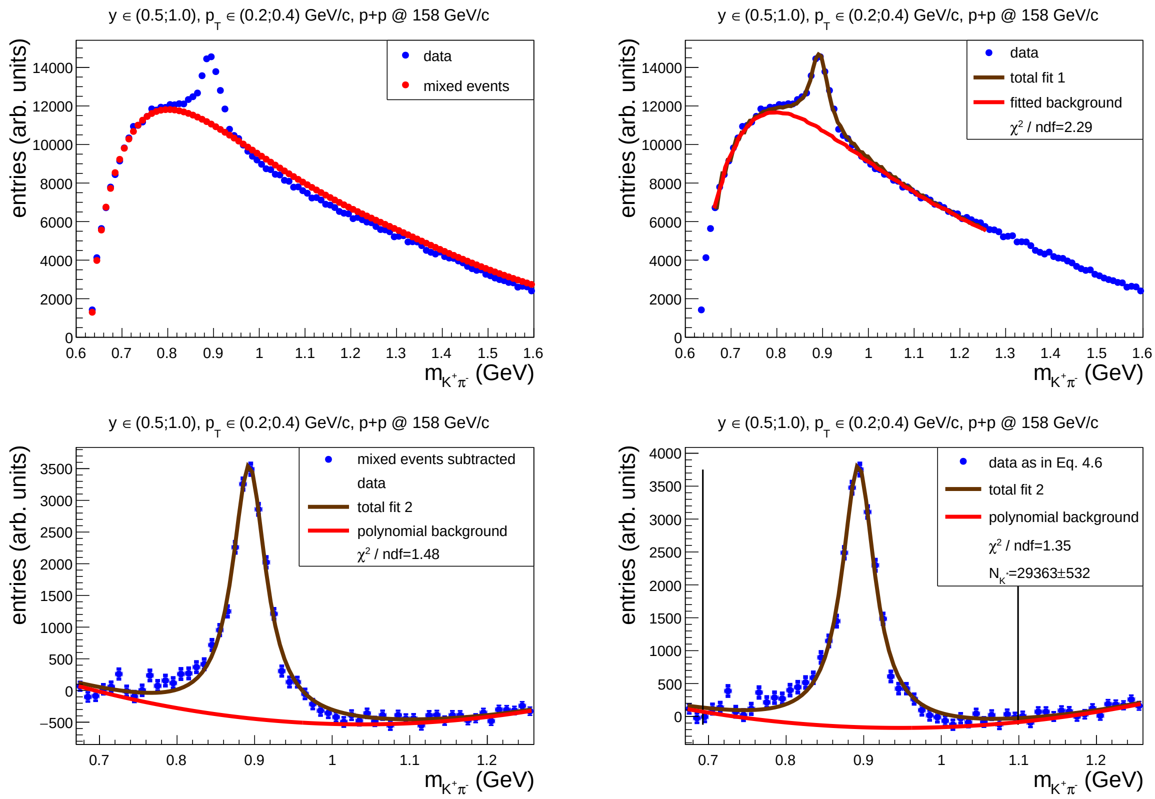

Figure 4.9: The example of the procedure of signal extraction for $K^*(892)^0$ in rapidity bin $0.5 < y < 1.0$ and transverse momentum bin $0.2 < p_T < 0.4$ GeV/c for p+p collisions at 158 GeV/c. Top, left: data signal (blue points), and background histogram (red points) obtained from mixed events (standard method). Top, right: data signal (blue points), and fitted background (red line) obtained from the templates. Bottom: background subtracted signal for the standard method (left) and template method (right) – more details in the text. Thin black vertical lines in bottom right panel correspond to the range of integrating fit functions while obtaining the raw number of $K^*(892)^0$ mesons ($m_0 \pm \Gamma_0$; see the text for details).

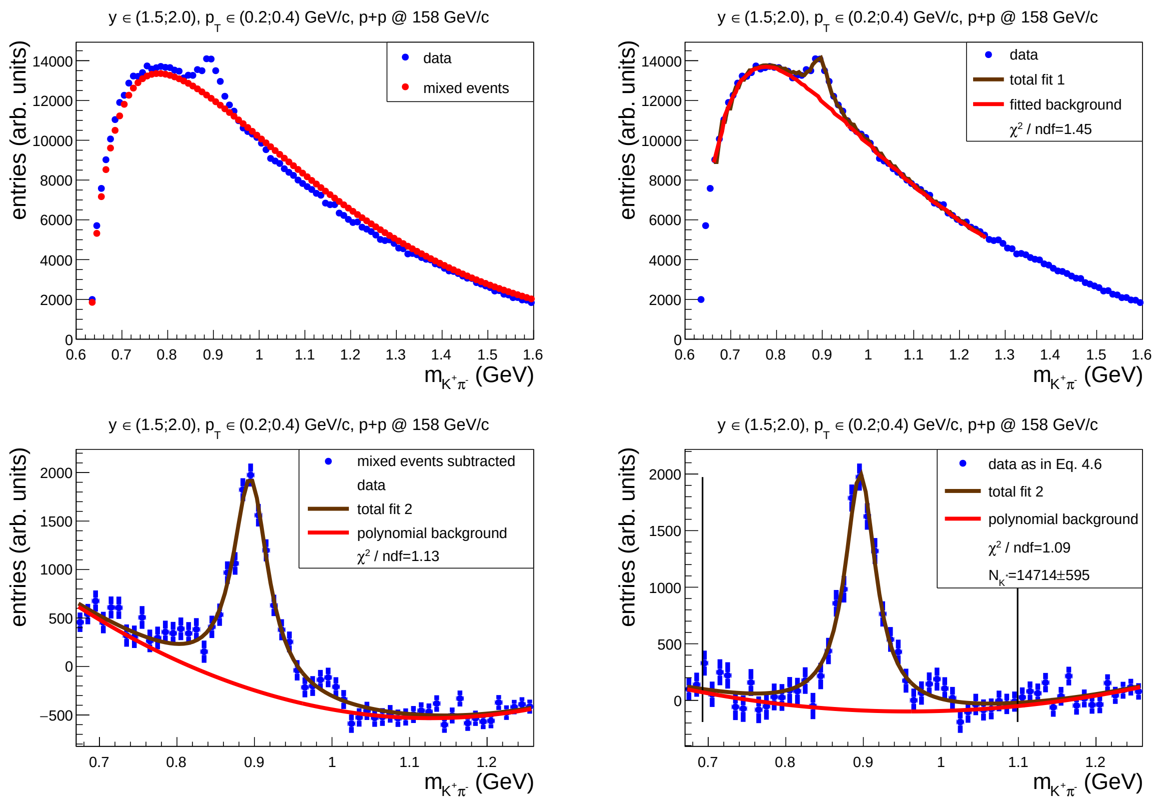

Figure 4.10: Same as Fig. 4.9 but for $1.5 < y < 2.0$ and $0.2 < p_T < 0.4$ GeV/c.

4.6 Uncorrected numbers of $K^*(892)^0$

The method of extracting $K^*(892)^0$ signal was described in Sec. 4.5.3. Figure 4.11 presents the uncorrected numbers of $K^*(892)^0 (N_{K^*})$ as obtained from the extraction procedure described in Sec. 4.5.3. The values are shown with statistical uncertainties. For each $m_{K^+\pi^-}$ invariant mass bin in Fig. 4.9 or 4.10 (bottom, right), the bin content $N_{bin}(m_{K^+\pi^-})$ was calculated as:

$$N_{bin}(m_{K^+\pi^-}) = N_{raw}(m_{K^+\pi^-}) - a \cdot T^{MC}_{res}(m_{K^+\pi^-}) - b \cdot T^{DATA}_{mix}(m_{K^+\pi^-}), \tag{4.6}$$

where $N_{raw}(m_{K^+\pi^-})$ is the raw production in a given $m_{K^+\pi^-}$ bin, and the rest of elements (a, b, $T^{MC}_{res}(m_{K^+\pi^-})$, and $T^{DATA}_{mix}(m_{K^+\pi^-})$) are defined in Eq. 4.5. For simplifying the equations, the $m_{K^+\pi^-}$ notation will be further omitted.

The statistical uncertainty of $N_{bin}(m_{K^+\pi^-})$ was calculated on the basis of Eq. 4.7:

$$\Delta N_{bin} = \sqrt{(\Delta N_{raw})^2 + a^2(\Delta T^{MC}_{res})^2 + b^2(\Delta T^{DATA}_{mix})^2}, \tag{4.7}$$

where ΔN_{raw}, ΔT^{MC}_{res}, and ΔT^{DATA}_{mix} are calculated as the square roots of the number of entries. The T^{MC}_{res} and T^{DATA}_{mix} histograms were normalized to the same number of entries as real data histogram. The normalization factors are included in the standard statistical uncertainties (ΔT^{MC}_{res} and ΔT^{DATA}_{mix}). The uncertainties of a and b parameters were neglected due to high statistics of data, Monte Carlo, and mixed events.

The uncorrected number of $K^*(892)^0$ mesons for a given rapidity and transverse momentum bin, $N_{K^*}(y, p_T)$, is calculated as the integral over the BW component in a function described by Eq. 4.2 (marked as *total fit 2* in Figs. 4.9 and 4.10, bottom, right). The integral was obtained within the mass window $m_0 \pm 4\Gamma_0$. The statistical uncertainty of the uncorrected number of $K^*(892)^0$ mesons, $\Delta N_{K^*}(y, p_T)$, was obtained as the uncertainty of the integral. This value was calculated using the ROOT [96] package which takes into account the covariance matrix of the fitted parameters. The $N_{K^*}(y, p_T)$ values, with its statistical uncertainties, are shown in Fig. 4.11. The statistics of events for p+p interactions at 40 and 80 GeV/c was not sufficient to analyze $K^*(892)^0$ meson production both in rapidity and transverse momentum bins. Therefore, for those two energies, the uncorrected numbers of $K^*(892)^0$ were obtained in rapidity bins only.

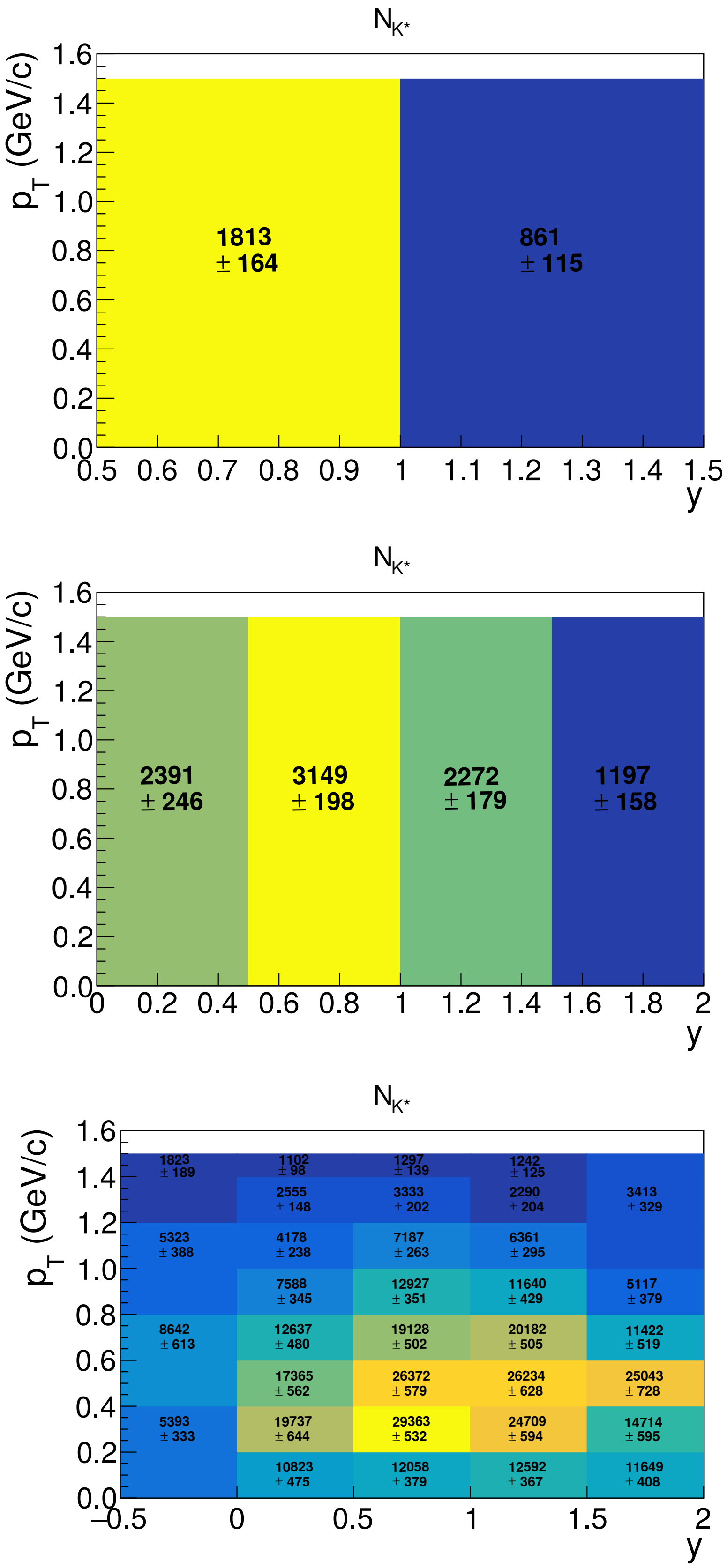

Figure 4.11: The uncorrected numbers of $K^*(892)^0$ mesons in inelastic p+p interactions at 40 (top), 80 (middle), and 158 (bottom) GeV/c beam momenta.

4.7 Correction factors

The procedure of obtaining the uncorrected number of $K^*(892)^0$ mesons was described in Sec. 4.6. These numbers should be corrected for effects which reduce the $K^*(892)^0$ peak such as identification inefficiency, geometrical acceptance, track and event reconstruction inefficiencies, and losses of inelastic p+p events due to the trigger bias.

The list of corrections used to determine the corrected numbers of $K^*(892)^0$ mesons produced in inelastic p+p interactions:

(i) The K^+ and π^- candidates were selected on the basis of dE/dx cuts (see Sec. 4.3). The correction for the identification inefficiency is defined as:

$$c_{dE/dx} = \frac{1}{\epsilon_{K^+} \cdot \epsilon_{\pi^-}} = 1.158, \tag{4.8}$$

where $\epsilon_{K^+} = 0.866$ and $\epsilon_{\pi^-} = 0.997$ are the probabilities for K^+ or π^- to lie within 1.5σ or 3σ around the theoretical Bethe-Bloch value. The probabilities were calculated on the basis of the cumulative Gaussian distribution.

(ii) The $K^*(892)^0$ meson was studied in the $K^+\pi^-$ decay channel. Therefore, the number of obtained $K^*(892)^0$ mesons should be divided by a branching ratio (BR) for $K^+\pi^-$ decay channel (equal to 2/3). The value of BR was calculated based on the Clebsch-Gordan coefficients [3, 97].

(iii) The corrections for geometrical acceptance, event and track reconstruction efficiencies, event losses due to the trigger bias, detector acceptance as well as the quality cuts are calculated on the basis of Monte Carlo simulated data. The EPOS 1.99 [90] model was used to produce 19.7×10^6 (p_{beam}=40 GeV/c), 19.8×10^6 (p_{beam}=80 GeV/c) and 227.9×10^6 (p_{beam}=158 GeV/c) inelastic p+p events. The validity of these events for calculation of the corrections was verified in Refs. [84, 98]. The width of $K^*(892)^0$ resonance was simulated according to the known PDG value [99]. The produced particles were tracked through the NA61/SHINE detector using the GEANT 3.21 package [95]. The next step was simulation of TPC response using dedicated NA61/SHINE software which allowed to repeat the same reconstruction chain procedures as for experimental data. The output data from reconstruction software are called reconstructed MC data. They are subjected to the same event and track cuts as experimental data with exception of identification cuts (dE/dx and total momentum p_{lab}). The tracks are identified based on *matching procedures* which compare reconstructed tracks with simulated tracks (the two tracks are matched when the number of common points on tracks trajectories is higher than 70%; in case of more simulated candidates the best one is selected for matching). The correction factor was calculated separately for each y and p_T bin according to Eq. 4.9:

$$c_{MC}(y, p_T) = \frac{n_{gen}(y, p_T)}{n_{sel}(y, p_T)} = \frac{N^{gen}_{K^*}(y, p_T)}{N^{gen}_{events}} / \frac{N^{sel}_{K^*}(y, p_T)}{N^{sel}_{events}}, \tag{4.9}$$

where:

- $N^{gen}_{K^*}(y, p_T)$ is the number of $K^*(892)^0$ mesons produced by the EPOS 1.99 model in a given rapidity and transverse momentum bin,
- $N^{sel}_{K^*}(y, p_T)$ is the number of $K^*(892)^0$ obtained on the basis of reconstructed MC data in a given rapidity and transverse momentum bin after applying the same event and track cuts (without dE/dx and p_{lab}) as for real data. In the *standard method*, the resonance is reconstructed on the basis of decay products which keep the history on the decay vertex position. This method was used in the NA49 experiment to calculate correction factors for $K^*(892)^0$ mesons [47]. In this analysis (*template method*), the number of $K^*(892)^0$ was obtained by repeating the same steps as in experimental data, starting from creation of invariant mass distributions of all $K^+\pi^-$ pairs (K^+ and π^- particles in MC reconstructed data were identified based on matching procedure) and then using the template method of signal extraction.
- N^{gen}_{events} is the number of generated inelastic p+p events based on the EPOS 1.99 model (19.7×10^6 for p_{beam}=40 GeV/c, 19.8×10^6 for p_{beam}=80 GeV/c, and 227.9×10^6 for p_{beam}=158 GeV/c),
- N^{sel}_{events} is the number of reconstructed and accepted p+p events (13.5×10^6 for p_{beam}=40 GeV/c, 15.6×10^6 for p_{beam}=80 GeV/c, and 140.1×10^6 for p_{beam}=158 GeV/c).

The uncertainty of $c_{MC}(y, p_T)$ was calculated assuming that the denominator $n_{sel}(y, p_T)$ is a subset of nominator $n_{gen}(y, p_T)$ and thus has a binomial distribution. The uncertainty of $c_{MC}(y, p_T)$ was calculated as follows:

$$\Delta c_{MC}(y, p_T) = c_{MC}(y, p_T)\sqrt{\frac{N_{K^*}^{gen}(y, p_T) - N_{K^*}^{sel}(y, p_T)}{N_{K^*}^{gen} \cdot N_{K^*}^{sel}}}. \tag{4.10}$$

The values of correction factors $c_{MC}(y, p_T)$, together with statistical uncertainties, are presented in Fig. 4.12.

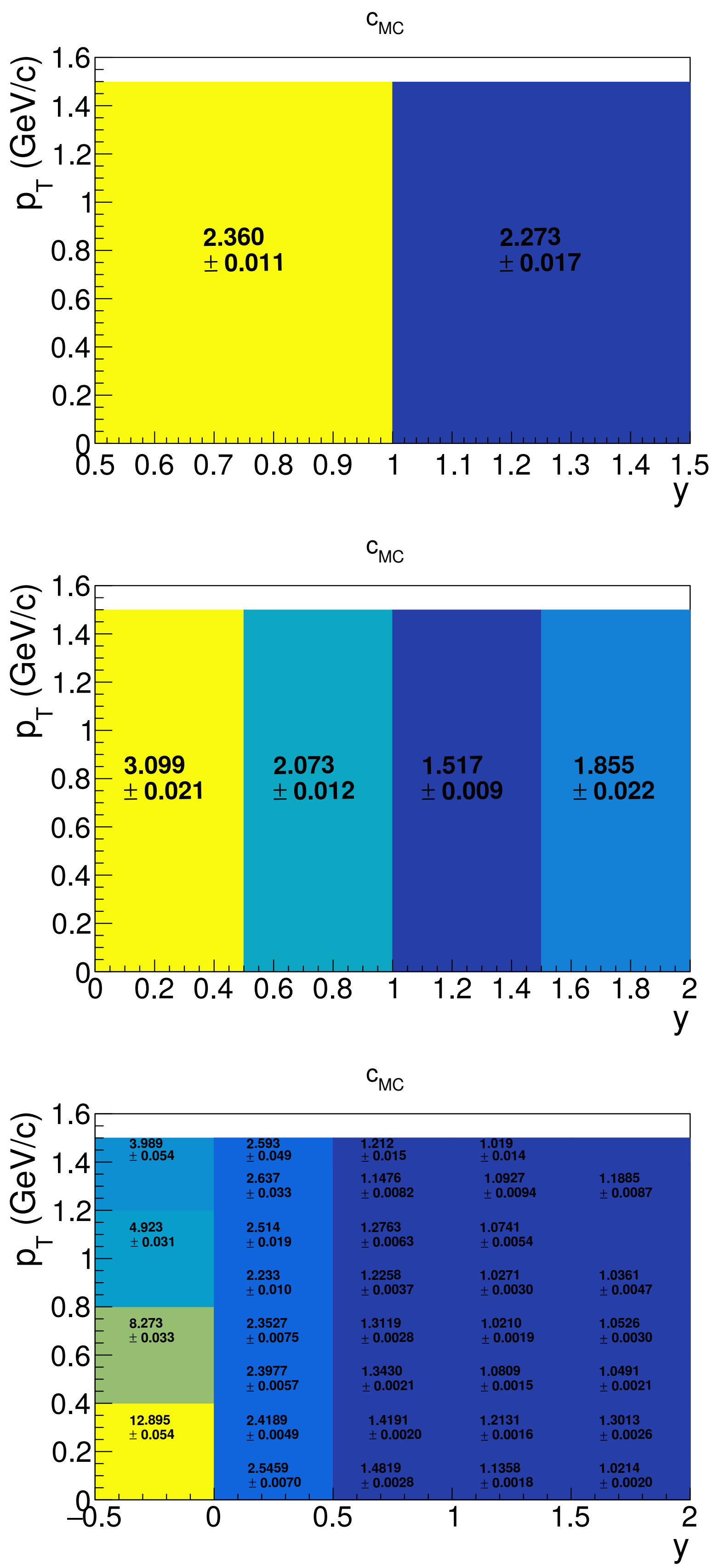

Figure 4.12: The correction factors $c_{MC}(y, p_T)$ with statistical uncertainties for p+p interactions at 40 (top), 80 (middle), and 158 (bottom) GeV/c.

4.8 Corrected yields of $K^*(892)^0$

The double-differential yield of $K^*(892)^0$ per inelastic event in a bin of (y, p_T) is calculated as follows:

$$\frac{d^2n}{dy\,dp_T}(y, p_T) = \frac{1}{BR} \cdot \frac{N_{K^*}(y, p_T)}{N_{events}} \cdot \frac{c_{dE/dx} \cdot c_{MC}(y, p_T)}{\Delta y\,\Delta p_T}, \tag{4.11}$$

where:

- $BR = 2/3$ is the branching ratio of $K^*(892)^0$ decay into $K^+\pi^-$ pairs,
- $N_{K^*}(y, p_T)$ is the uncorrected number of $K^*(892)^0$, obtained by the template method of signal extraction described in Sec. 4.5.3,
- N_{events} is the number of events after cuts,
- $c_{dE/dx}$, $c_{MC}(y, p_T)$ are correction factors described in Sec. 4.7,
- Δy and Δp_T are the bin widths of rapidity and transverse momentum, respectively.

The corrected double-differential yields of $K^*(892)^0$ are presented in Sections 5.2 and 5.3.

4.9 Statistical uncertainties

The statistical uncertainties of the corrected double-differential yields (see Eq. 4.11) were calculated based on the formula:

$$\Delta\frac{d^2n}{dy\,dp_T}(y, p_T) = \frac{1}{BR} \cdot \left[\left(\frac{c_{dE/dx} \cdot c_{MC}(y, p_T)}{N_{events}\,\Delta y\,\Delta p_T}\right)^2 \Delta N^2_{K^*}(y, p_T) + \left(\frac{N_{K^*}(y, p_T) \cdot c_{dE/dx}}{N_{events}\,\Delta y\,\Delta p_T}\right)^2 \Delta c^2_{MC}(y, p_T)\right]^{\frac{1}{2}}. \tag{4.12}$$

This equation takes into account the statistical uncertainties of $c_{MC}(y, p_T)$ (see Eq. 4.10) and the statistical uncertainties $\Delta N_{K^*}(y, p_T)$ (see Sec. 4.6) of the uncorrected numbers of $K^*(892)^0$ mesons. The correction $c_{dE/dx}$ has no statistical uncertainty.

4.10 Systematic uncertainties

The uncorrected numbers of $K^*(892)^0$ mesons (and later on the corrected yields), $K^*(892)^0$ mass and width parameters, etc. depend on the details of signal extraction procedure and the event and track quality cuts, chosen for the analysis. These two groups of effects were studied in order to obtain the systematic uncertainties.

(I) The uncertainty due to the signal extraction procedure:

- (i) the invariant mass fitting range was changed from (0.66;1.26) GeV to (0.69;1.26) GeV (see Figs. 4.9, 4.10, top, right),
- (ii) the initial value of the Γ_{K^*} parameter of the Breit-Wigner distribution (Eq. 4.3) was changed by ±8%,
- (iii) the initial value of the mass parameter (m_{K^*}) of the Breit-Wigner distribution (Eq. 4.3) was changed by ±0.3 MeV,
- (iv) the parameters a, b, and c in invariant mass fitting function (Eq. 4.5) were changed by ±10%.
- (v) the value of the Γ_{K^*} parameter of the Breit-Wigner distribution was fixed at the PDG value (Γ_0),
- (vi) the value of the m_{K^*} parameter of the Breit-Wigner distribution was fixed at the PDG value (m_0),
- (vii) the residual background description was changed from the second order polynomial curve to the third order one (red line in bottom, right plot in Figs. 4.9 and 4.10),
- (viii) the invariant mass range over which the raw number of $K^*(892)^0$ was integrated was changed from $m_0 \pm 4\Gamma_0$ to $\pm 3.5\Gamma_0$ and $\pm 4.5\Gamma_0$,
- (ix) the raw number of $K^*(892)^0$ was obtained as the sum of points (after 2nd order polynomial subtraction) instead of the integral over the Breit-Wigner signal.

(II) The uncertainty due to changing the event and track quality cuts:

- (i) the window in which off-time beam particles are not allowed was changed from ±1 μs to ±1.5 μs around the trigger (beam) particle,

(ii) the allowed range of the z-position of the interaction vertex was modified from $[-590; -572]$ cm to $[-591; -571]$ cm and $[-589, -573]$ cm,

(iii) the $\mathrm{d}E/\mathrm{d}x$ cuts ($\pm 3\sigma$ for π^- and $\pm 1.5\sigma$ for K^+) were changed into $\pm 2.5\sigma$ for π^-, $\pm 1.0\sigma$ for K^+ (narrower cut) and $\pm 3.5\sigma$ for π^-, $\pm 2.0\sigma$ for K^+ (wider cut),

(iv) the minimum required total number of points in all TPCs for K^+ and π^- candidates was modified from 30 to 25 and 35,

(v) the minimum required number of clusters in both VTPCs for K^+ and π^- candidates was modified from 15 to 12 and 18,

(vi) the impact parameter (distance between extrapolated track and the interaction point) cuts for the tracks were turned off.

The final systematic uncertainty was calculated as:

$$\sigma_{sys} = \sqrt{\sum \sigma_i^2}, \tag{4.13}$$

where σ_i is a partial systematic uncertainty for each of the possible sources described above. It is calculated as half of the difference between the lowest and the highest value obtained by varying the given parameter.

The I (ii), I (iii), and I (iv) sources have negligible contributions to the total systematic uncertainties.

The contributions of different sources of systematic uncertainties on the inverse slope parameter (T) of transverse momentum spectra (see Sec. 5.3), width (σ_y) of Gaussian rapidity distribution (see Sec. 5.4), and mean multiplicity of $K^*(892)^0$ mesons (see Sec. 5.5) are shown in Figs. 4.13–4.21.

The final systematic uncertainties are shown in figures in Chapter 5 and 6 as shaded bands.

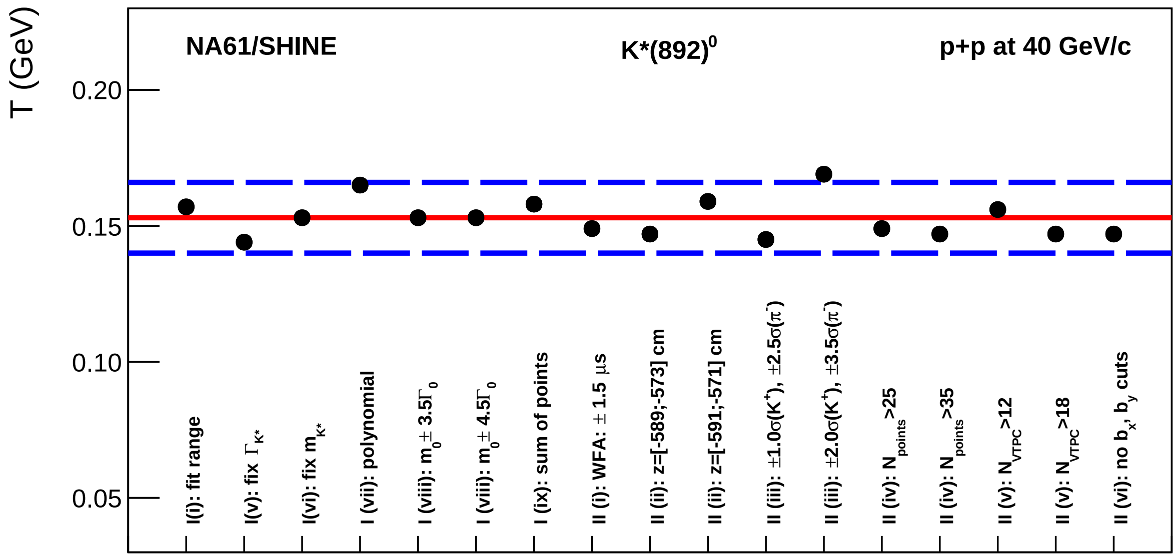

Figure 4.13: The inverse slope parameter T of transverse momentum spectrum at mid-rapidity region ($0 < y < 0.5$) for p+p interactions at 40 GeV/c beam momentum. The points represent the T parameter values for different sources of systematic uncertainties. The red line corresponds to the original value of the inverse slope parameter. The blue, dashed lines are original value of T parameter plus/minus the final systematic uncertainty.

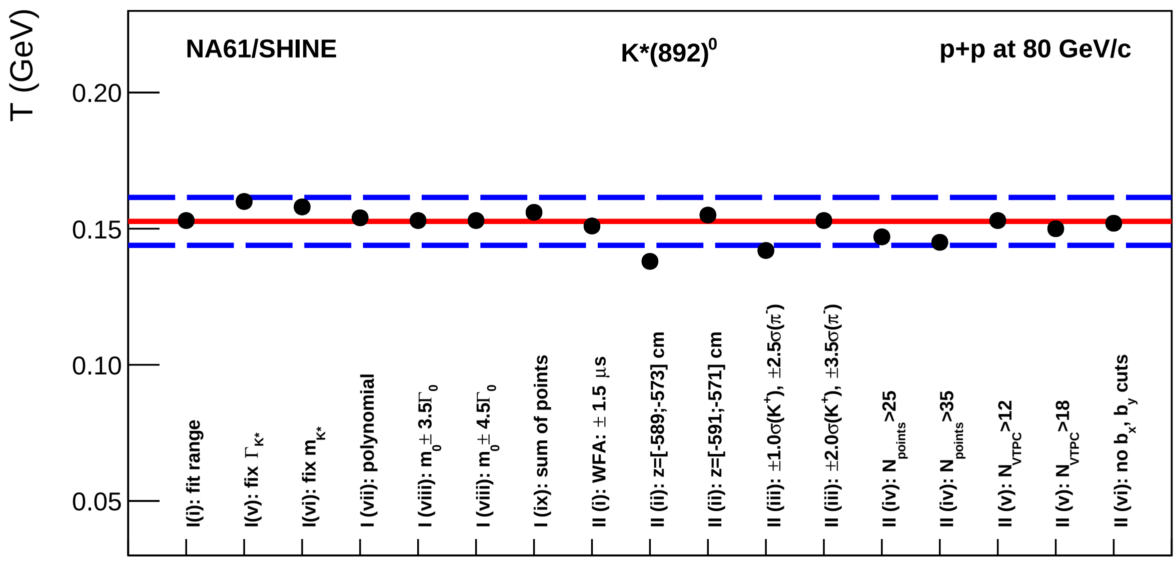

Figure 4.14: Same as Fig. 4.13 but for p+p interactions at 80 GeV/c beam momentum.

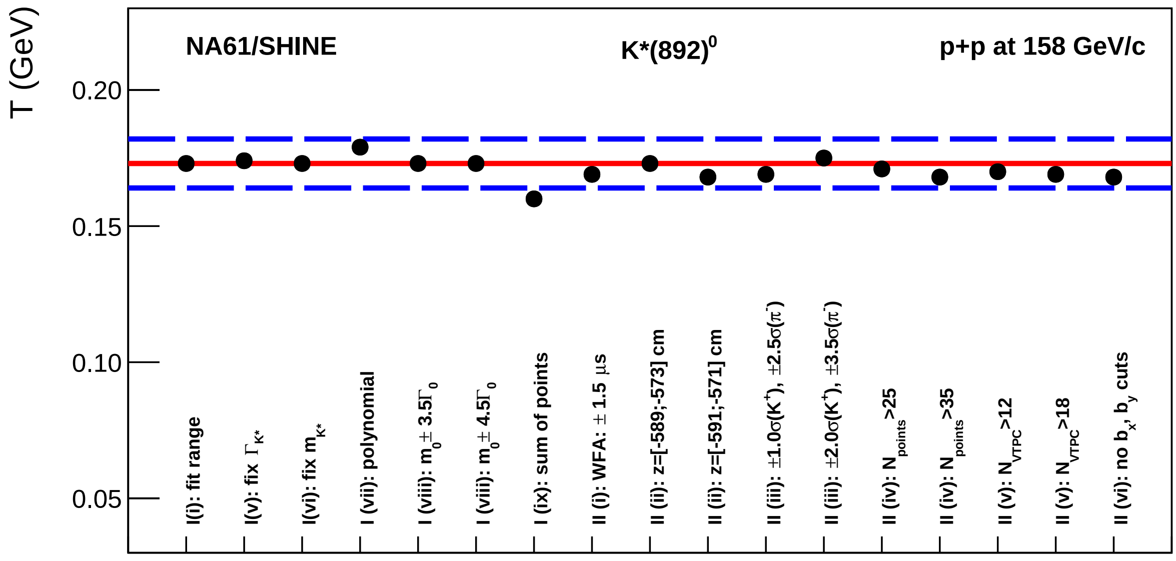

Figure 4.15: Same as Fig. 4.13 but for p+p interactions at 158 GeV/c beam momentum.

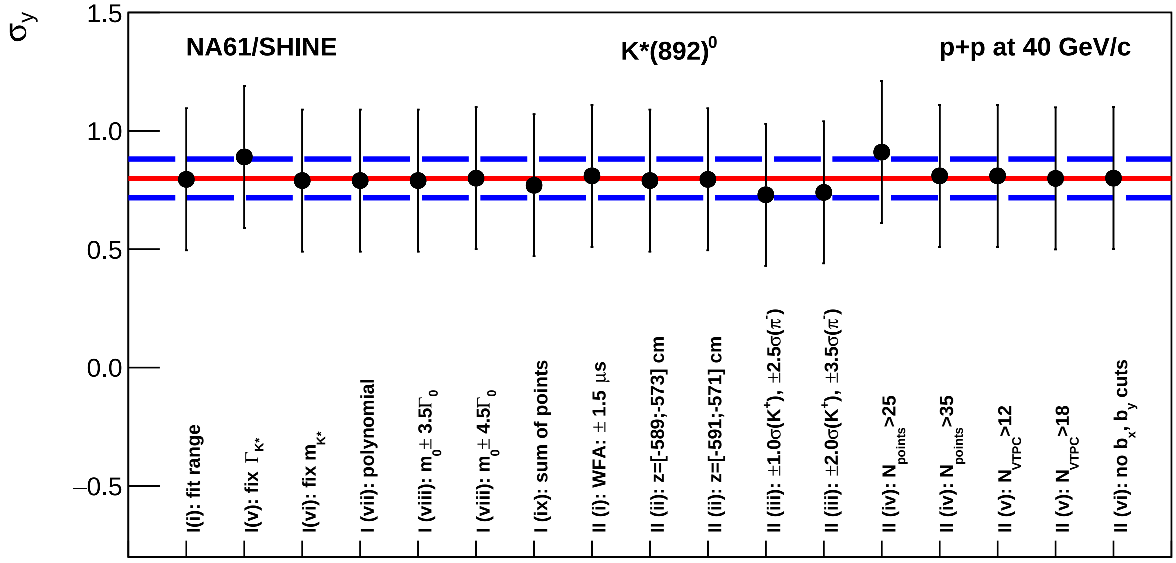

Figure 4.16: The σ_y of Gaussian fit to rapidity spectrum for p+p interactions at 40 GeV/c beam momentum. The points represent the σ_y values for different sources of systematic uncertainties. The red line corresponds to the original value of the σ_y parameter. The blue, dashed lines are original value of the σ_y parameter plus/minus the final systematic uncertainty.

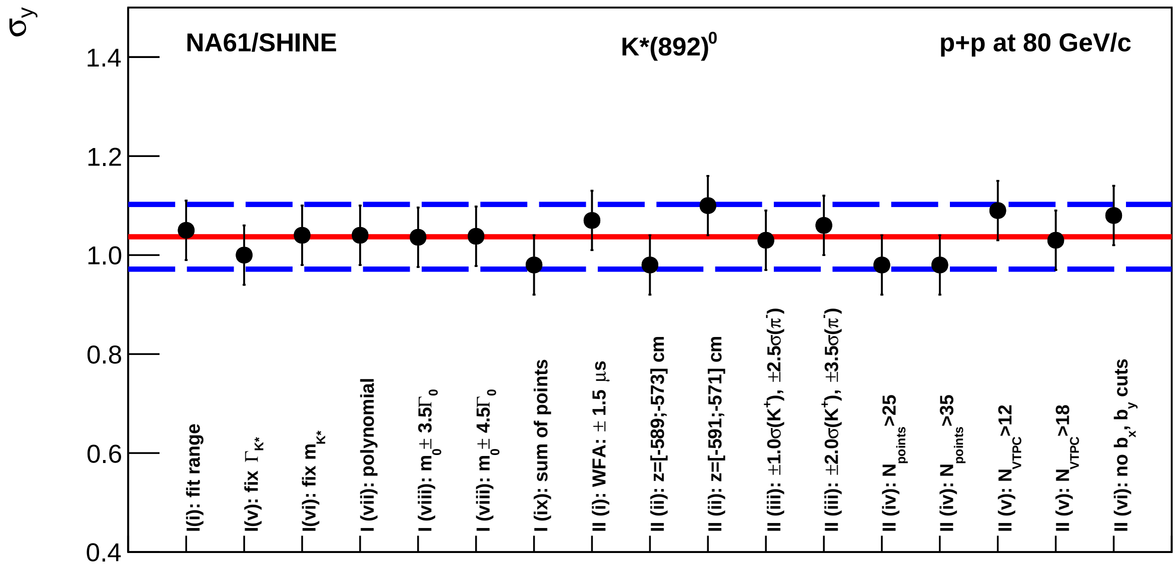

Figure 4.17: Same as Fig. 4.16 but for p+p interactions at 80 GeV/c beam momentum.

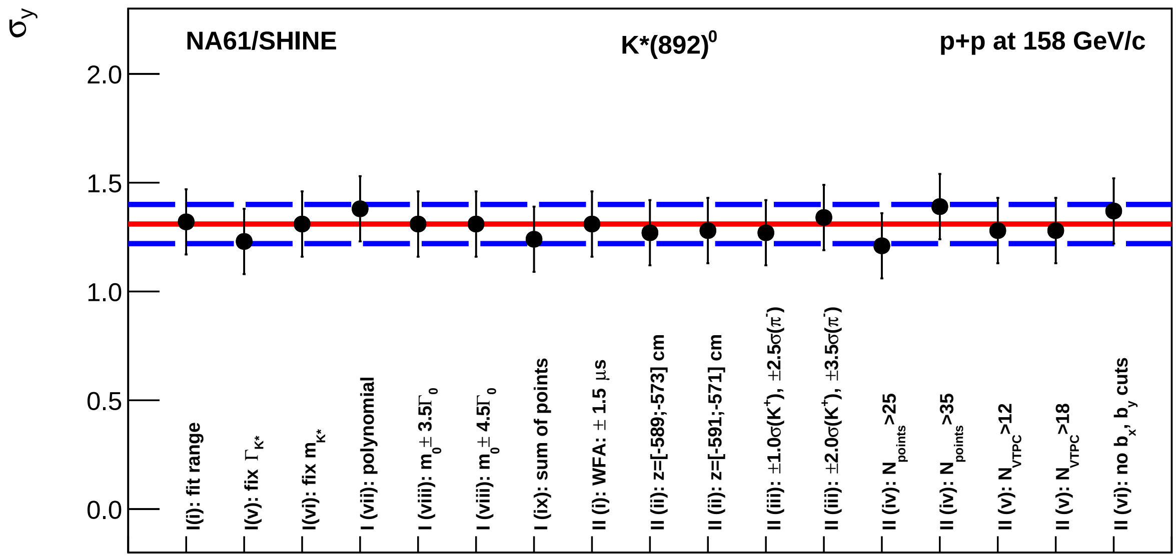

Figure 4.18: Same as Fig. 4.16 but for p+p interactions at 158 GeV/c beam momentum.

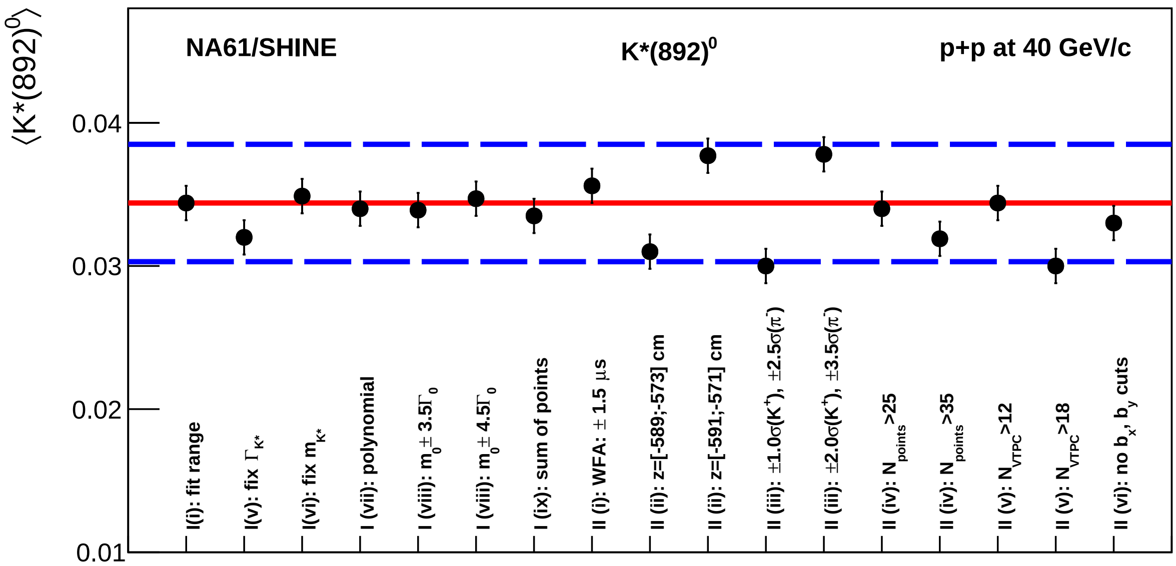

Figure 4.19: The mean multiplicity of $K^*(892)^0$ for p+p interactions at 40 GeV/c beam momentum. The points represent the $\langle K^*(892)^0 \rangle$ values for different sources of systematic uncertainties. The red line corrresponds to the original value of the $\langle K^*(892)^0 \rangle$. The blue, dashed lines are original value of the $\langle K^*(892)^0 \rangle$ plus/minus the final systematic uncertainty.

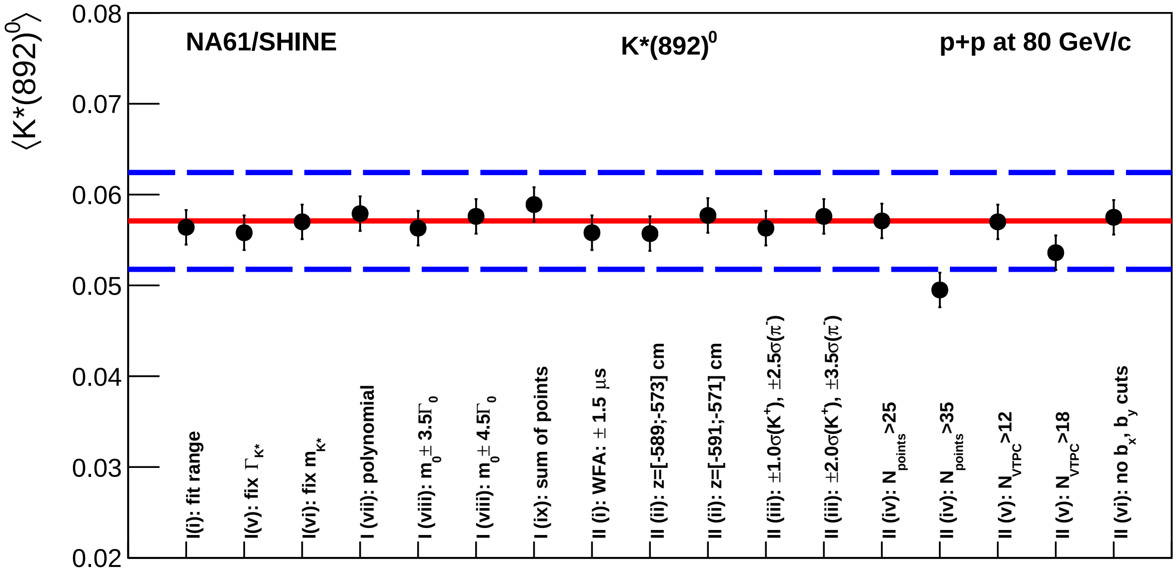

Figure 4.20: Same as Fig. 4.19 but for p+p interactions at 80 GeV/c beam momentum.

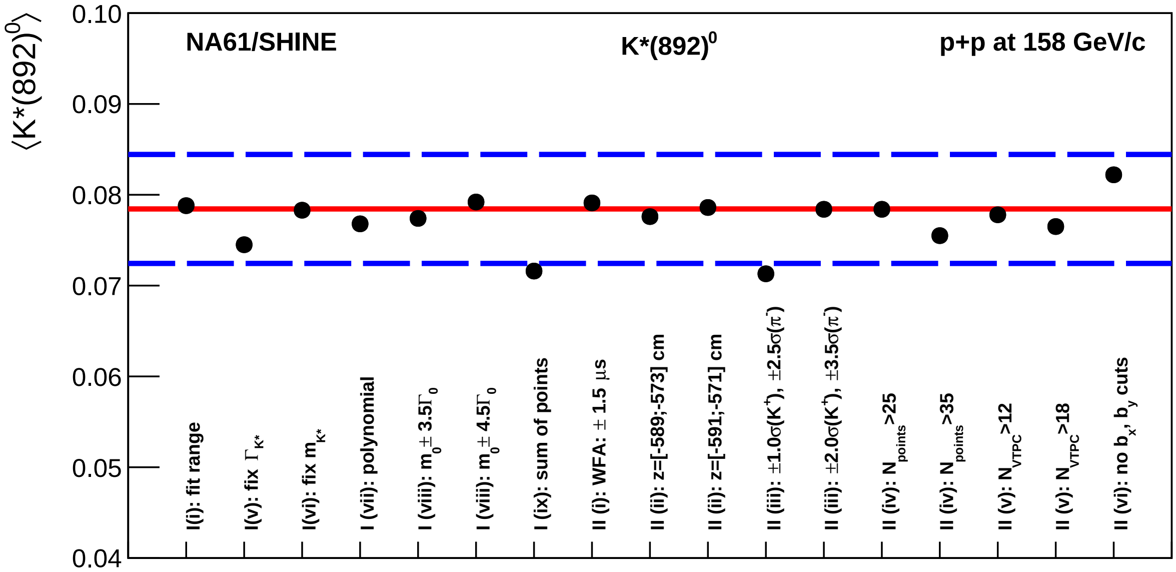

Figure 4.21: Same as Fig. 4.19 but for p+p interactions at 158 GeV/c beam momentum.

Chapter 5

Results

This chapter contains the results on $K^*(892)^0$ meson analysis, in particular, the rapidity and transverse momentum spectra. The calculated multiplicities of $K^*(892)^0$ are based on rapidity spectra. The mass and width of $K^*(892)^0$ were also obtained as functions of transverse momentum.

The results presented for p+p interactions at 158 GeV/c beam momentum are the basis of the Ref. [100] which is accepted by *The European Physical Journal C*. The results for p+p interactions at 40 and 80 GeV/c beam momenta, which are shown in this chapter, are slightly modified when compared to the preliminary NA61/SHINE results which were published in Ref. [101]. One of the differences is the method of fitting functions to invariant mass distribution which was changed from the Binned Maximum Likelihood method to the Minimum Chi-Square method which worked better in this case. The Minimum Chi-Square method was also used for the results from p+p interactions at 158 GeV/c [100].

5.1 Mass and width of $K^*(892)^0$

The mass and width of $K^*(892)^0$ mesons were obtained as parameters of Breit-Wigner fit (see Eq. 4.3) to the invariant mass spectra after (*total fit 2* in Figs. 4.9 and 4.10, bottom, right). The m_{K^*} and Γ_{K^*} values are shown in Fig. 5.1 as a function of p_T for $0 < y < 0.5$ (158 GeV/c beam momentum) or $0 < y < 1.5$ (40–80 GeV/c beam momenta). The numerical values are presented in Table 5.1. Please note, that the raw numbers of $K^*(892)^0$, presented in Fig. 4.11 for 40–80 GeV/c, were obtained in 2–4 rapidity bins but in one large p_T bin. In contrary, the mass and width of $K^*(892)^0$ mesons for 40–80 GeV/c

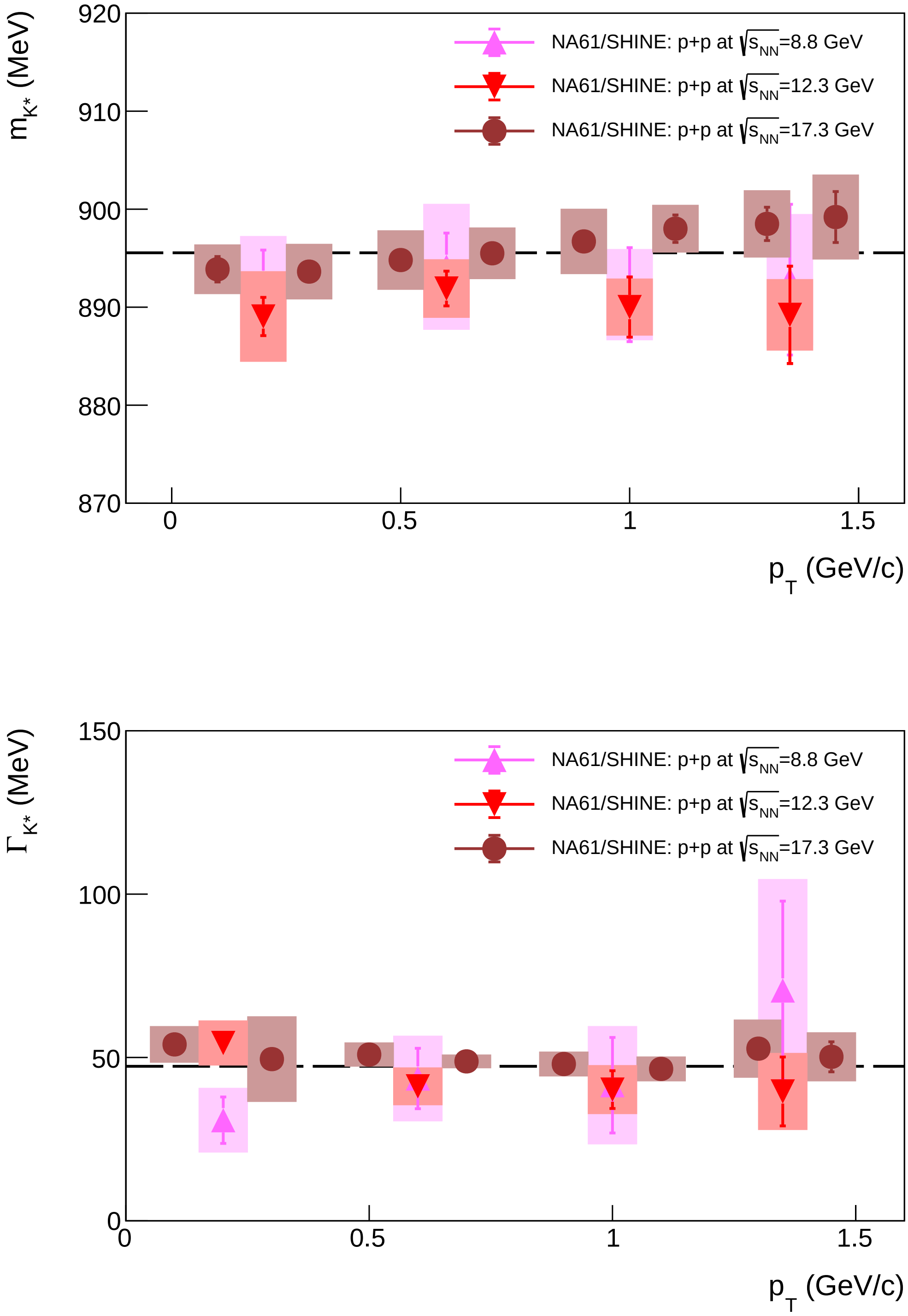

Figure 5.1: The $K^*(892)^0$ mass and width as a function of transverse momentum for inelastic p+p interactions at 40–158 GeV/c beam momenta. The values were obtained for rapidity $0 < y < 0.5$ (158 GeV/c) or $0 < y < 1.5$ (40–80 GeV/c). The numerical data are presented in Table 5.1. The horizontal lines correspond to the PDG values m_0=895.55 MeV and Γ_0=47.3 MeV [11].

	p+p @ 40 GeV/c		p+p @ 80 GeV/c		p+p @ 158 GeV/c	
p_T (GeV/c)	m_{K^*} (MeV)	Γ_{K^*} (MeV)	m_{K^*} (MeV)	Γ_{K^*} (MeV)	m_{K^*} (MeV)	Γ_{K^*} (MeV)
(0.0;0.2)	$892.5 \pm 3.3 \pm 4.7$	$30.8 \pm 7.1 \pm 9.8$	$889.1 \pm 1.9 \pm 4.6$	$54.4 \pm 3.6 \pm 6.8$	$893.9 \pm 1.3 \pm 2.5$	$54.00 \pm 0.64 \pm 5.5$
(0.2;0.4)					$893.63 \pm 0.90 \pm 2.8$	$49.50 \pm 0.93 \pm 13$
(0.4;0.6)	$894.1 \pm 3.4 \pm 6.4$	$43.6 \pm 9.2 \pm 13$	$891.9 \pm 1.8 \pm 2.9$	$41.2 \pm 3.4 \pm 5.7$	$894.81 \pm 0.93 \pm 3.0$	$50.9 \pm 3.3 \pm 3.6$
(0.6;0.8)					$895.50 \pm 0.92 \pm 2.6$	$48.8 \pm 1.8 \pm 2.0$
(0.8;1.0)	$891.3 \pm 4.8 \pm 4.6$	$41 \pm 15 \pm 18$	$890.0 \pm 3.1 \pm 2.9$	$40.2 \pm 5.8 \pm 7.4$	$896.7 \pm 1.1 \pm 3.3$	$48.0 \pm 2.1 \pm 3.7$
(1.0;1.2)					$898.0 \pm 1.4 \pm 2.4$	$46.5 \pm 2.5 \pm 3.7$
(1.2;1.4)	$892.8 \pm 7.7 \pm 6.7$	$71 \pm 27 \pm 34$	$889.2 \pm 5.0 \pm 3.6$	$40 \pm 10 \pm 12$	$898.5 \pm 1.7 \pm 3.4$	$52.7 \pm 3.3 \pm 8.8$
(1.4;1.5)					$899.2 \pm 2.6 \pm 4.3$	$50.2 \pm 4.6 \pm 7.4$

Table 5.1: The numerical values of mass and width of $K^*(892)^0$ mesons obtained in $0 < y < 0.5$ (for 158 GeV/c beam momentum) or $0 < y < 1.5$ (for 40 and 80 GeV/c beam momenta) and presented in Fig. 5.1. The first uncertainty is statistical, the second one is systematic.

data were calculated for several transverse momentum bins but in one larger rapidity bin.

For all three energies, within total uncertainties, the obtained Γ_{K^*} values are consistent with PDG ($\Gamma_0 = 47.3$ MeV [11]) represented as a horizontal line in Fig. 5.1 (bottom). For 158 GeV/c and 40 GeV/c m_{K^*} values are also consistent with PDG ($m_0 = 895.55$ MeV [11]) within uncertainties. For 80 GeV/c data the observed m_{K^*} values seem to be slightly smaller than PDG. For the highest beam momentum (158 GeV/c), a slight increase of the m_{K^*} parameter with p_T might be observed. The corresponding slope is significant since a large part of the shown systematic uncertainty is due to the magnetic field uncertainty (see below). The change of the m_{K^*} parameter with transverse momentum does not introduce a systematic variation of the $K^*(892)^0$ yield since the parameter is fitted in each (y, p_T) bin, and the signal integration range ($\approx$ 380 MeV) is much larger than the m_{K^*} change ($\approx$ 6 MeV).

Studying of the K^0_S[(1)] and Λ[(2)] invariant mass spectra allowed to determine the precision of the magnetic field strength which is better than 1% [102]. The influence of magnetic field calibration on the results (p+p at 158 GeV/c) were checked by changing the momentum components of K^+ and π^- candidates by $\pm$1%. The $K^*(892)^0$ width and yield were not changed significantly. However, the resulting changes of the mass parameter are equal or larger than uncertainties described in Sec. 4.10. Therefore, the additional component, connected with magnetic field calibration, was taken into account in the final systematic uncertainty of the mass of $K^*(892)^0$ meson.

5.2 Double-differential $K^*(892)^0$ spectra

The yield of $K^*(892)^0$ mesons in rapidity bins are presented in Fig. 5.2 (top and middle) for inelastic p+p interactions at 40 and 80 GeV/c beam momenta. For 158 GeV/c (Fig. 5.2, bottom) the statistics allowed to obtain the double-differential spectra in bins of rapidity and transverse momentum. The numerical values with uncertainties are given in Tables 5.3 and 5.2.

---

(1) The K^0_S is a short-lived neutral kaon which has mean lifetime about $8.9 \cdot 10^{-11}$ s. It consists of $(d\bar{s} + s\bar{d})/\sqrt{2}$ quarks.

(2) The Λ is a neutral lambda baryon containing uds quarks. The lifetime of Λ is about $2.6 \cdot 10^{-10}$ s.

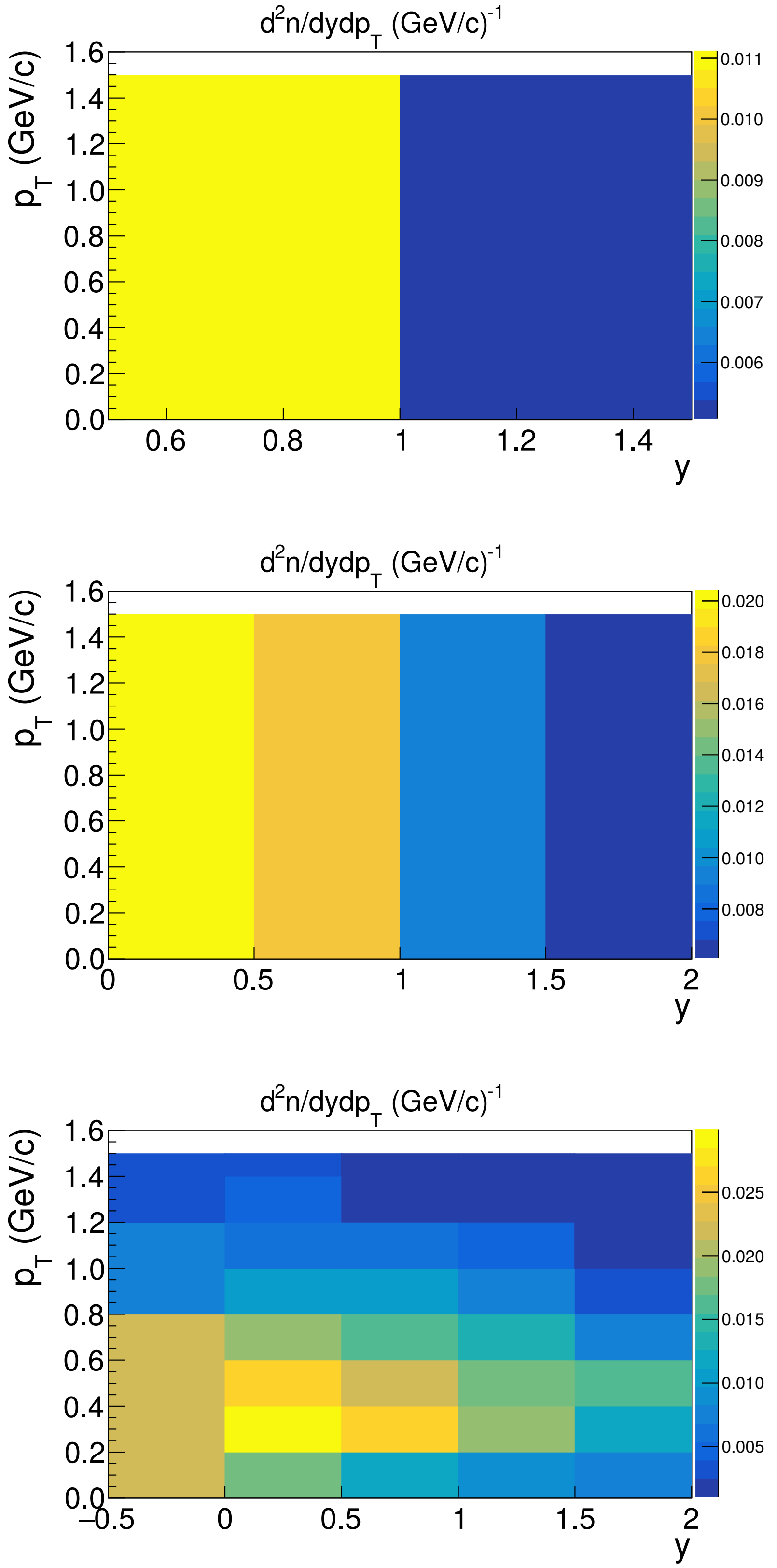

Figure 5.2: The $K^{*}(892)^{0}$ spectra in inelastic p+p interactions at 40 (top), 80 (middle), and 158 (bottom) GeV/c in rapidity and transverse momentum (only p+p at 158 GeV/c) bins, calculated based on Eq. 4.11. The numerical values are presented in Tables 5.3 and 5.2.

5.3 Transverse momentum and transverse mass spectra of $K^*(892)^0$

The statistics of data for p+p interactions at 40 and 80 GeV/c beam momenta is significantly smaller than for p+p interactions at 158 GeV/c. Therefore, for those two lower beam momenta, the analysis of $K^*(892)^0$ mesons was performed either in rapidity bins or transverse momentum bins. The first (rapidity) spectra allowed to determine the mean multiplicities of $K^*(892)^0$ mesons (see Fig. 5.7) and were obtained for large transverse momentum bin ($0 < p_T < 1.5$) GeV/c. The second (transverse momentum) spectra were used to obtain the inverse slope parameter T (see Fig. 5.3) and were obtained for large rapidity bin ($0 < y < 1.5$). The numerical values of transverse momentum spectra at 40 and 80 GeV/c are presented in Table 5.3.

The high statistics of p+p data at 158 GeV/c beam momentum allowed to prepare the double-differential yields of $K^*(892)^0$ mesons as function of transverse momentum. They are presented in Fig. 5.4 for separate rapidity bins. The numerical values are given in Table 5.2.

The function described by equation:

$$f(p_T) = A \cdot p_T \, \exp\left(-\frac{\sqrt{p_T^2 + m_0^2}}{T}\right) \tag{5.1}$$

was fitted to transverse momentum spectra of $K^*(892)^0$ mesons in order to obtain the inverse slope parameters T. The values of T parameters are listed in the legends of Figs. 5.3 and 5.4.

Moreover, for 158 GeV/c p+p data the fits allowed to estimate the production of $K^*(892)^0$ mesons in the unmeasured high-p_T region. More details are available in Sec. 5.4.

The transverse mass spectra $\frac{1}{m_T}\frac{d^2n}{dm_T dy}$ were obtained based on transverse momentum spectra $\frac{d^2n}{dy dp_T}$ according to the relation:

$$\frac{1}{m_T}\frac{d^2n}{dm_T\, dy} = \frac{1}{p_T}\frac{d^2n}{dy\, dp_T}. \tag{5.2}$$

The transverse mass spectra for p+p interactions at 158 GeV/c are shown in Fig. 5.6 and the numerical values are listed in Table 5.4. The transverse mass spectra for p+p interactions at 40 and 80 GeV/c (in $0 < y < 1.5$) are presented and compared with

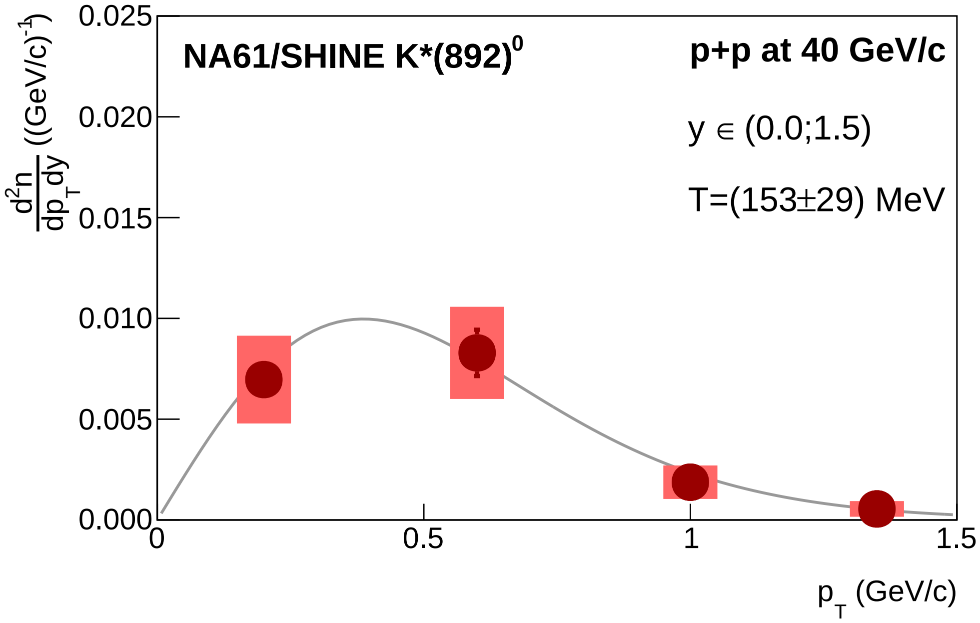

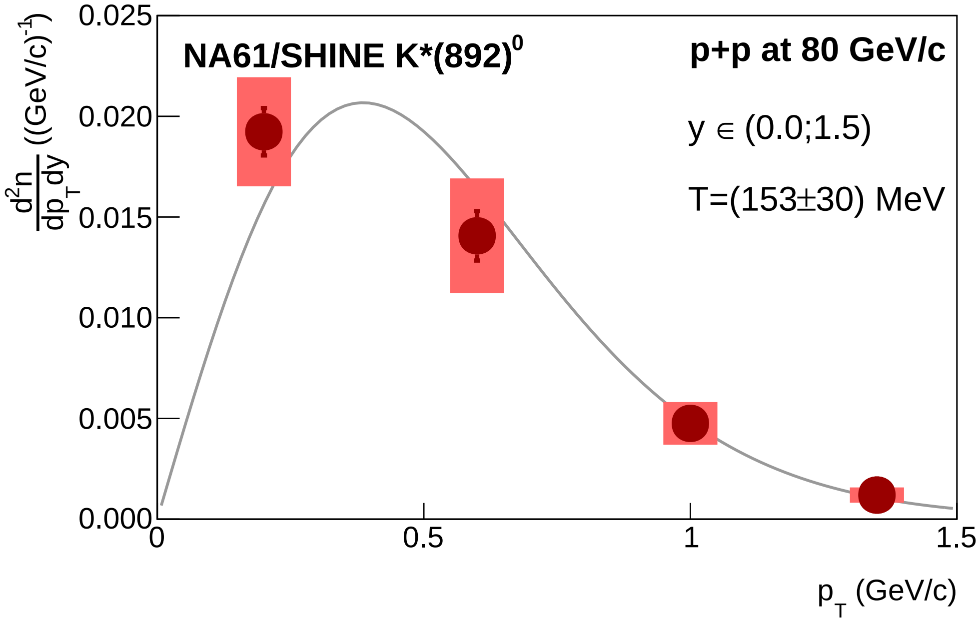

Figure 5.3: The transverse momentum spectra $\frac{d^2n}{dp_T dy}$ of $K^*(892)^0$ mesons for p+p interactions at 40 (top) and 80 (bottom) GeV/c beam momenta. The range of rapidity was taken as $0 < y < 1.5$. The function given by Eq. 5.1 was fitted to data and presented as solid lines in plots. The numerical values are given in Table 5.3. The fitted inverse slope parameters T are quoted in the legends.

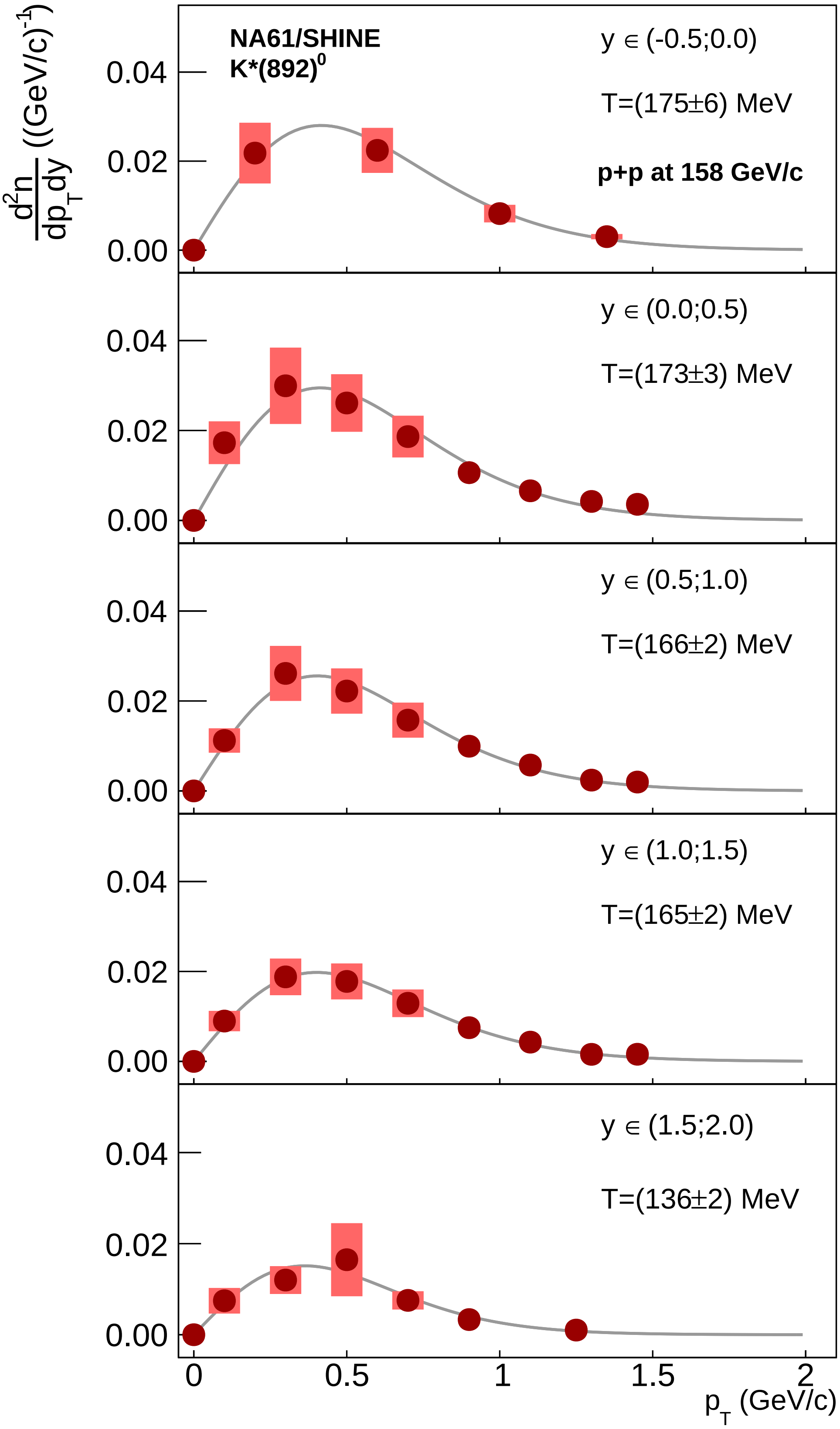

Figure 5.4: The transverse momentum spectra $\frac{d^2n}{dp_T dy}$ of $K^*(892)^0$ mesons in p+p at 158 GeV/c for five bins of rapidity. The function given by Eq. 5.1 was fitted to data and presented as solid lines in plots. The numerical values are given in Table 5.2. The fitted inverse slope parameters T for each bin are quoted in the legends.

<table>
<tr><th rowspan="2">p_T (GeV/c)</th><th colspan="3">y</th></tr>
<tr><th>(-0.5;0.0)</th><th>(0.0;0.5)</th><th>(0.5;1.0)</th></tr>
<tr><td>(0.0;0.2)</td><td rowspan="2">21.8 ± 1.3 ± 6.7</td><td>17.28 ± 0.76 ± 4.7</td><td>11.21 ± 0.35 ± 2.6</td></tr>
<tr><td>(0.2;0.4)</td><td>29.94 ± 0.98 ± 8.4</td><td>26.13 ± 0.47 ± 6.0</td></tr>
<tr><td>(0.4;0.6)</td><td rowspan="2">22.4 ± 1.6 ± 5.0</td><td>26.11 ± 0.85 ± 6.3</td><td>22.21 ± 0.49 ± 4.9</td></tr>
<tr><td>(0.6;0.8)</td><td>18.65 ± 0.71 ± 4.6</td><td>15.74 ± 0.41 ± 3.8</td></tr>
<tr><td>(0.8;1.0)</td><td rowspan="2">8.22 ± 0.60 ± 1.9</td><td>10.62 ± 0.48 ± 2.6</td><td>9.94 ± 0.27 ± 2.3</td></tr>
<tr><td>(1.0;1.2)</td><td>6.59 ± 0.38 ± 1.8</td><td>5.75 ± 0.21 ± 1.4</td></tr>
<tr><td>(1.2;1.4)</td><td rowspan="2">3.04 ± 0.32 ± 0.51</td><td>4.22 ± 0.25 ± 1.2</td><td>2.39 ± 0.15 ± 0.56</td></tr>
<tr><td>(1.4;1.5)</td><td>3.58 ± 0.33 ± 1.2</td><td>1.97 ± 0.21 ± 0.55</td></tr>
</table>

<table>
<tr><th rowspan="2">p_T (GeV/c)</th><th colspan="2">y</th></tr>
<tr><th>(1.0;1.5)</th><th>(1.5;2.0)</th></tr>
<tr><td>(0.0;0.2)</td><td>8.97 ± 0.26 ± 2.2</td><td>7.46 ± 0.26 ± 2.7</td></tr>
<tr><td>(0.2;0.4)</td><td>18.79 ± 0.45 ± 4.0</td><td>12.00 ± 0.49 ± 3.0</td></tr>
<tr><td>(0.4;0.6)</td><td>17.78 ± 0.43 ± 3.9</td><td>16.47 ± 0.48 ± 7.9</td></tr>
<tr><td>(0.6;0.8)</td><td>12.92 ± 0.32 ± 3.0</td><td>7.54 ± 0.34 ± 1.9</td></tr>
<tr><td>(0.8;1.0)</td><td>7.49 ± 0.28 ± 1.7</td><td>3.32 ± 0.25 ± 0.47</td></tr>
<tr><td>(1.0;1.2)</td><td>4.28 ± 0.20 ± 1.1</td><td rowspan="3">1.017 ± 0.082 ± 0.38</td></tr>
<tr><td>(1.2;1.4)</td><td>1.57 ± 0.14 ± 0.44</td></tr>
<tr><td>(1.4;1.5)</td><td>1.59 ± 0.16 ± 0.68</td></tr>
</table>

Table 5.2: The numerical values of double-differential yields $\frac{d^2n}{dp_T dy}$ of $K^*(892)^0$ mesons with statistical (first value) and systematic (second value) uncertainties for p+p interactions at 158 GeV/c. The values are given in units of 10^{-3} (GeV/c)$^{-1}$. These data were used to prepare Fig. 5.4.

p_T (GeV/c)	p+p at 40 GeV/c	p+p at 80 GeV/c
(0.0;0.4)	6.96 ± 0.91 ± 2.2	19.2 ± 1.2 ± 2.7
(0.4;0.8)	8.3 ± 1.2 ± 2.3	14.1 ± 1.2 ± 2.8
(0.8;1.2)	1.87 ± 0.42 ± 0.81	4.75 ± 0.72 ± 1.0
(1.2;1.5)	0.547 ± 0.094 ± 0.37	1.20 ± 0.33 ± 0.36

Table 5.3: The numerical values of $\frac{d^2n}{dp_T dy}$ of $K^*(892)^0$ mesons with statistical (first value) and systematic (second value) uncertainties for p+p interactions at 40 and 80 GeV/c. The values are given in units of 10^{-3} (GeV/c)$^{-1}$. These data were used to prepare plots in Fig. 5.3.

158 GeV/c (in $0 < y < 0.5$) in Fig. 5.5, and the numerical values for 40 and 80 GeV/c are given in Table 5.5.

The inverse slope parameters of transverse momentum spectra (Fig. 5.3) were obtained as: $T = (153 \pm 29 \pm 13)$ MeV for $p_{beam} = 40$ GeV/c and $T = (153 \pm 30 \pm 9)$ MeV for $p_{beam} = 80$ GeV/c. These values are taken from the fits to transverse momentum spectra for rapidity bin $0 < y < 1.5$. For p+p data at 158 GeV/c (Fig. 5.4) the inverse slope parameter was found to be equal to $T = (173 \pm 3 \pm 9)$ MeV. The fit to transverse momentum spectra was performed at the mid-rapidity region ($0 < y < 0.5$). All values are given with statistical uncertainties, taken as the uncertainty of the fit parameter, and systematic uncertainties obtained in the way described in Sec. 4.10. The NA49 experiment obtained the T parameter of the p_T spectrum in the rapidity range $0.2 < y < 0.7$ for p+p data at 158 GeV/c, and published a value $T = (166 \pm 11 \pm 10)$ MeV [47].

$m_T - m_0$ (GeV)	p_T (GeV/c)	y (-0.5;0.0)	y (0.0;0.5)	y (0.5;1.0)
0.011	(0.0;0.2)	109.0 ± 6.7 ± 34	172.8 ± 7.6 ± 47	112.1 ± 3.5 ± 26
0.054	(0.2;0.4)		99.8 ± 3.3 ± 28	87.1 ± 1.6 ± 20
0.134	(0.4;0.6)	37.4 ± 2.6 ± 8.3	52.2 ± 1.7 ± 13	44.42 ± 0.97 ± 9.9
0.244	(0.6;0.8)		26.6 ± 1.0 ± 6.5	22.48 ± 0.59 ± 5.5
0.376	(0.8;1.0)	8.21 ± 0.60 ± 1.9	11.81 ± 0.54 ± 2.9	11.04 ± 0.30 ± 2.5
0.524	(1.0;1.2)		5.99 ± 0.34 ± 1.6	5.23 ± 0.19 ± 1.3
0.684	(1.2;1.4)	2.25 ± 0.23 ± 0.38	3.25 ± 0.19 ± 0.91	1.85 ± 0.11 ± 0.43
0.809	(1.4;1.5)		2.47 ± 0.22 ± 0.81	1.36 ± 0.15 ± 0.38

$m_T - m_0$ (GeV)	p_T (GeV/c)	y (1.0;1.5)	y (1.5;2.0)
0.011	(0.0;0.2)	89.7 ± 2.6 ± 22	74.6 ± 2.6 ± 27
0.054	(0.2;0.4)	62.6 ± 1.5 ± 13	40.0 ± 1.6 ± 9.9
0.134	(0.4;0.6)	35.57 ± 0.85 ± 7.8	32.95 ± 0.96 ± 16
0.244	(0.6;0.8)	18.46 ± 0.46 ± 4.3	10.77 ± 0.49 ± 2.8
0.376	(0.8;1.0)	8.33 ± 0.31 ± 1.8	3.69 ± 0.27 ± 0.52
0.524	(1.0;1.2)	3.89 ± 0.18 ± 0.99	0.814 ± 0.065 ± 0.31
0.684	(1.2;1.4)	1.21 ± 0.11 ± 0.34	
0.809	(1.4;1.5)	1.09 ± 0.11 ± 0.47	

Table 5.4: The numerical values of double-differential yields $\frac{1}{m_T}\frac{d^2n}{dm_T\,dy}$ of $K^*(892)^0$ mesons with statistical (first value) and systematic (second value) uncertainties for p+p interactions at 158 GeV/c. The values are given in units of 10^{-3} (GeV)$^{-2}$. The values of $m_T - m_0$ specify the bin centers. These data were used to prepare Fig. 5.6.

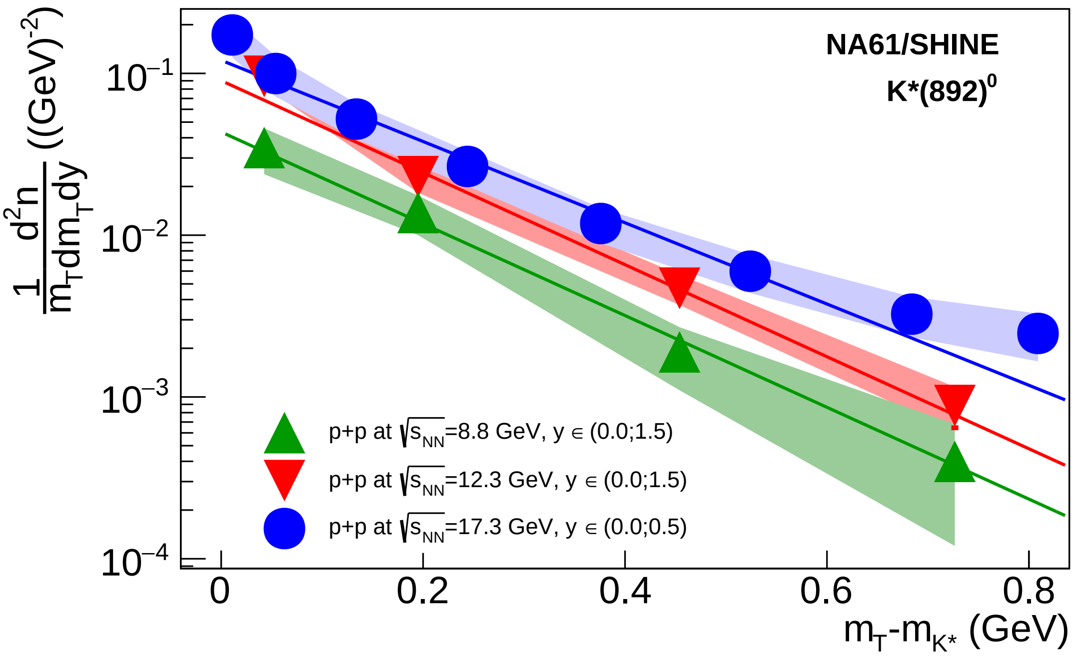

Figure 5.5: Transverse mass spectra $\frac{1}{m_T}\frac{d^2n}{dm_T\,dy}$ of $K^*(892)^0$ mesons in p+p interactions at 40–158 GeV/c. Results obtained in $0 < y < 1.5$ (p_{beam} = 40 and 80 GeV/c) or $0 < y < 0.5$ (p_{beam} = 158 GeV/c). The numerical values are listed in Tables 5.5 and 5.4. The lines represent the fitted functions given by Eqs. 5.1 and 5.2. Their parameters (A and T) are given in the legends of Figs. 5.3 and 5.4.

$m_T - m_0$ (GeV)	p_T (GeV/c)	p+p at 40 GeV/c	p+p at 80 GeV/c
0.043	(0.0;0.4)	34.8 ± 4.5 ± 11	96.2 ± 5.9 ± 13
0.195	(0.4;0.8)	13.8 ± 1.9 ± 3.8	23.4 ± 2.1 ± 4.7
0.454	(0.8;1.2)	1.87 ± 0.42 ± 0.81	4.75 ± 0.72 ± 1.0
0.727	(1.2;1.5)	0.405 ± 0.069 ± 0.27	0.88 ± 0.24 ± 0.27

Table 5.5: The numerical values of double-differential yields $\frac{1}{m_T}\frac{d^2n}{dm_T\,dy}$ of $K^*(892)^0$ mesons with statistical (first value) and systematic (second value) uncertainties for p+p interactions at 40 and 80 GeV/c. The values are given in units of 10^{-3} (GeV)$^{-2}$. The values of $m_T - m_0$ specify the bin centers. These data were used to prepare Fig. 5.5.

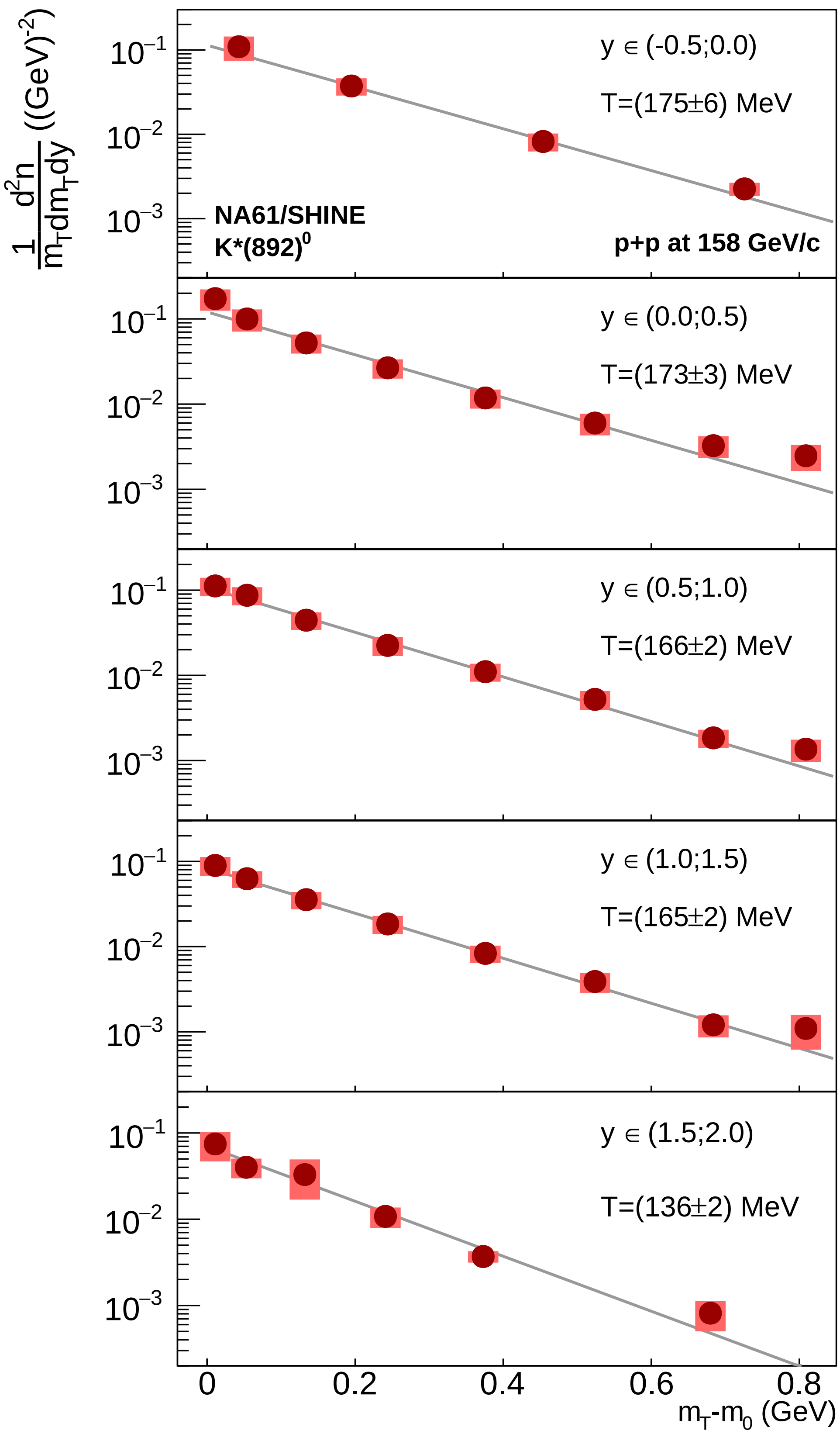

Figure 5.6: The transverse mass spectra $\frac{1}{m_T}\frac{d^2n}{dm_T\,dy}$ of $K^*(892)^0$ mesons in p+p at 158 GeV/c for five bins of rapidity. The numerical values are given in Table 5.4. The functions (solid lines) are described by Eqs. 5.1 and 5.2 with the fit parameters (A and T) taken from Fig. 5.4.

5.4 Rapidity distributions of $K^*(892)^0$

The rapidity distribution $\frac{dn}{dy}$, for p+p interactions at p_{beam} = 40 and 80 GeV/c, was obtained from invariant mass spectra prepared in rapidity bins but for large transverse momentum bin ($0 < p_T < 1.5$ GeV/c).

The high statistics of data, for p+p interactions at p_{beam} = 158 GeV/c, allowed to prepare the rapidity distribution by integrating and extrapolating (for the non-measured high-p_T region) the $\frac{d^2n}{dy\,dp_T}$ spectrum:

$$\frac{dn}{dy} = \sum_i \frac{d^2n}{dy\,dp_T} \cdot dp_T + \frac{A_{p_T}}{I_{p_T}} \sum_i \frac{d^2n}{dy\,dp_T} \cdot dp_T, \tag{5.3}$$

where:

$$A_{p_T} = \int_{1.5}^{+\infty} A{\cdot}p_T \exp\left(-\frac{\sqrt{p_T^2+m_0^2}}{T}\right) dp_T, \qquad I_{p_T} = \int_0^{1.5} A{\cdot}p_T \exp\left(-\frac{\sqrt{p_T^2+m_0^2}}{T}\right) dp_T. \tag{5.4}$$

The inverse slope parameters T were taken from the corresponding plots in Fig. 5.4. The equation:

$$\Delta\frac{dn}{dy} = \sqrt{\left(1+\frac{A_{p_T}}{I_{p_T}}\right)^2 \cdot \sum_i dp_T^2 \cdot \left(\Delta\frac{d^2n}{dy\,dp_T}\right)^2} \tag{5.5}$$

was used to calculate the statistical uncertainty of each point in the p_T-integrated and extrapolated rapidity distribution.

The comparison of rapidity distributions of $K^*(892)^0$ mesons for these energies is shown in Fig. 5.7. The numerical values are given in Table 5.6. The Gaussian function:

$$f(y) = A \cdot \exp\left(-\frac{y^2}{2\,\sigma_y^2}\right) \tag{5.6}$$

was fitted to the points to measure the width σ_y of the $K^*(892)^0$ rapidity distribution and to determine the mean multiplicity of $K^*(892)^0$ mesons (more details are given in Sec. 5.5). For p+p interactions at p_{beam} = 158 GeV/c, the first point ($y < 0$) was obtained only to check the symmetry of the distribution and was not included in the fit.

The statistical uncertainty of σ_y was taken from the fit and the systematic uncertainty was obtained in the way described in Sec. 4.10. The numerical values of fit parameters σ_y and mean multiplicities of $K^*(892)^0$ mesons (see Sec. 5.5) are presented in Table 5.6.

y	$\frac{dn}{dy}$		
	p+p at 40 GeV/c	p+p at 80 GeV/c	p+p at 158 GeV/c
(-0.5;0.0)	-	-	$(22.50 \pm 0.89 \pm 3.5) \cdot 10^{-3}$
(0.0;0.5)	-	$(20.4 \pm 2.1 \pm 3.9) \cdot 10^{-3}$	$(23.71 \pm 0.37 \pm 2.6) \cdot 10^{-3}$
(0.5;1.0)	$(11.1 \pm 1.0 \pm 1.3) \cdot 10^{-3}$	$(18.0 \pm 1.1 \pm 1.8) \cdot 10^{-3}$	$(19.27 \pm 0.20 \pm 1.9) \cdot 10^{-3}$
(1.0;1.5)	$(5.08 \pm 0.68 \pm 0.73) \cdot 10^{-3}$	$(9.51 \pm 0.75 \pm 1.0) \cdot 10^{-3}$	$(14.83 \pm 0.17 \pm 1.4) \cdot 10^{-3}$
(1.5;2.0)	-	$(6.10 \pm 0.81 \pm 1.4) \cdot 10^{-3}$	$(10.73 \pm 0.22 \pm 1.8) \cdot 10^{-3}$
σ_y	$0.768 \pm 0.29 \pm 0.082$	$1.037 \pm 0.059 \pm 0.065$	$1.31 \pm 0.15 \pm 0.09$
$\langle K^*(892)^0 \rangle$	$(34.4 \pm 1.2 \pm 3.8) \cdot 10^{-3}$	$(57.1 \pm 1.9 \pm 5.3) \cdot 10^{-3}$	$(78.44 \pm 0.38 \pm 6.0) \cdot 10^{-3}$

Table 5.6: The numerical values of rapidity distributions presented in Fig. 5.7. The first uncertainty is statistical, the second is systematic. Additionally, the table shows the widths of the Gaussian fits to the $\frac{dn}{dy}$ distributions and the mean multiplicities of $K^*(892)^0$ mesons (see the text for details).

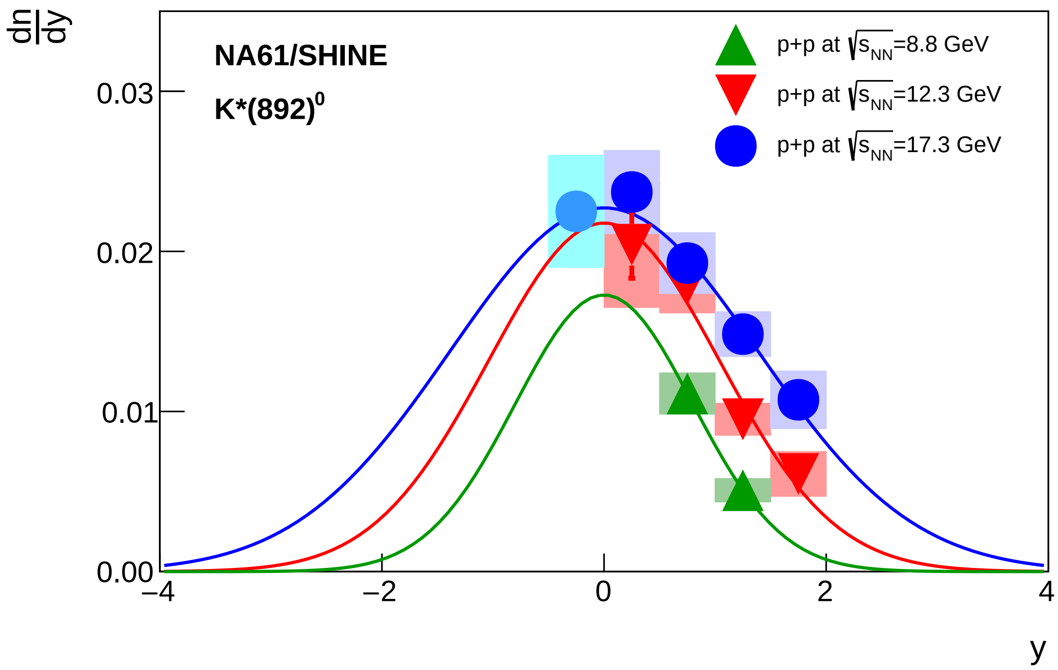

Figure 5.7: The rapidity spectra $\frac{dn}{dy}$ of $K^*(892)^0$ mesons for p+p interactions at 40–158 GeV/c beam momenta. For 158 GeV/c data the p_T-integrated and extrapolated rapidity distribution is shown; for 40 and 80 GeV/c data, the $\frac{dn}{dy}$ distribution was obtained for large transverse momentum bin ($0 < p_T < 1.5$ GeV/c). The fitted Gaussian functions are represented by Eq. 5.6. For 158 GeV/c the first point ($y < 0$) was not included in the fit (see the text for details). The numerical values are given in Table 5.6.

5.5 Mean multiplicities of $K^*(892)^0$

The mean multiplicities of $K^*(892)^0$ mesons were obtained based on rapidity distributions presented in Fig. 5.7. The high statistics of p+p data at $p_{beam} = 158$ GeV/c allowed to check the symmetry of $\frac{dn}{dy}$ distribution by adding additional point for $y < 0$. Assuming rapidity symmetry around $y = 0$, the $\langle K^*(892)^0 \rangle$ was calculated as the sum of measured points (for 158 GeV/c the point with $y < 0$ was not included in the sum) and the integral of the fitted Gaussian function (Eq. 5.6) in the unmeasured region:

$$\langle K^*(892)^0 \rangle = \sum_i \frac{dn}{dy} \cdot dy + \left(\frac{A_{y-} + A_{y+}}{I_y} \right) \sum_i \frac{dn}{dy} \cdot dy, \quad (5.7)$$

where:

$$A_{y-} = \int_{-\infty}^{0} A \cdot e^{-\frac{y^2}{2\sigma_y^2}} dy, \qquad A_{y+} = \int_{2.0}^{+\infty} A \cdot e^{-\frac{y^2}{2\sigma_y^2}} dy, \qquad I_y = \int_{0}^{2.0} A \cdot e^{-\frac{y^2}{2\sigma_y^2}} dy. \quad (5.8)$$

The statistical uncertainties of $K^*(892)^0$ multiplicities were calculated from the formula:

$$\Delta \langle K^*(892)^0 \rangle = \sqrt{\left(1 + \frac{A_{y-} + A_{y+}}{I_y}\right)^2 \cdot \sum_i dy^2 \cdot \left(\Delta \frac{dn}{dy}\right)^2}, \quad (5.9)$$

and the systematic uncertainties were estimated in the way described in Sec. 4.10.

The mean multiplicities of $K^*(892)^0$ mesons, produced in inelastic p+p collisions at 40–158 GeV/c, are given in Table. 5.6 and presented in Fig. 5.8.

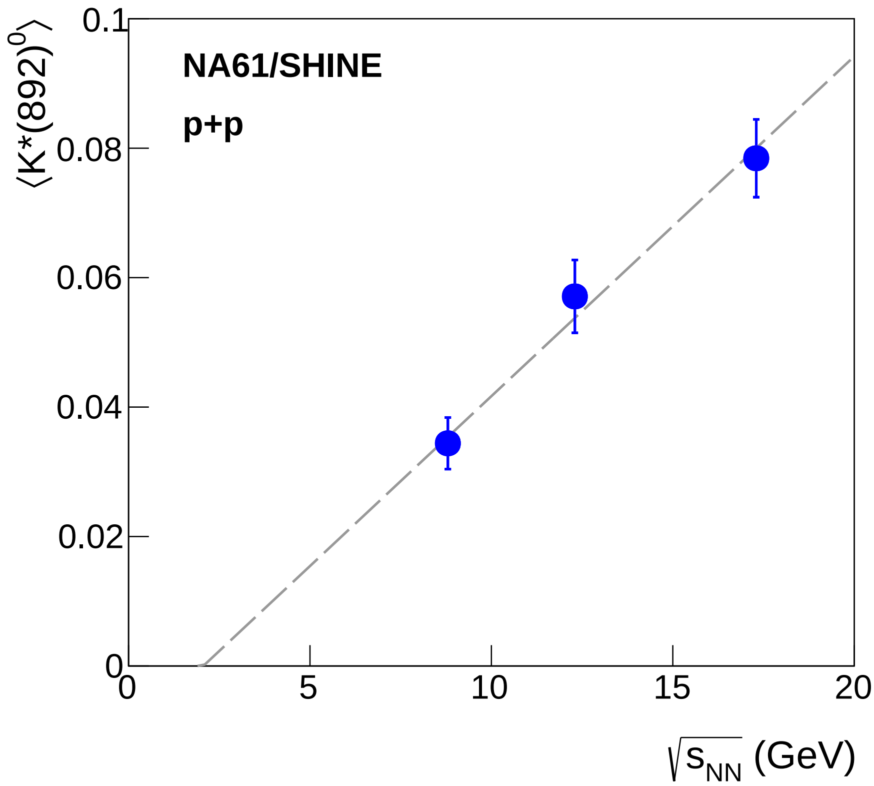

Figure 5.8: The $\langle K^*(892)^0 \rangle$ obtained from p+p data at p_{beam} = 40–158 GeV/c. The numerical values are presented in Table. 5.6. The mean multiplicities of $K^*(892)^0$ mesons were calculated based on Eq. 5.7. The bars represent the total uncertainties (square root of the sum of squares of statistical and systematic uncertainties). The dashed line represents the fitted 1st order polynomial curve to show the trend.

Chapter 6

Comparison with world data and model predictions

This chapter is focused on a comparison of the obtained results from inelastic p+p interactions at 40–158 GeV/c with publicly available world data as well as with predictions from microscopic and statistical models. Moreover, the calculated ratio of $\langle K^*(892^0)\rangle$ to $\langle K^{+/-}\rangle$ is used to determine the lower limit of the time between kinetic and chemical freeze-outs.

6.1 Mass and width of $K^*(892)^0$ peak

The comparison of mass and width of $K^*(892)^0$ meson peak with world data is shown in Fig 6.1. The results are presented from p+p interactions by NA61/SHINE, STAR (top RHIC energy), as well as from Pb+Pb and Au+Au collisions at SPS (NA49), RHIC (STAR), and LHC (ALICE) energies. In case of the ALICE and STAR experiments, the mass and width of K^{*0} meson peak were calculated as the averaged measurements from $K^*(892)^0$ and $\overline{K^*}(892)^0$ invariant mass spectra.

The obtained values of m_{K^*} and Γ_{K^*} in the NA61/SHINE experiment are close to the PDG values. However, somehow lower m_{K^*} values may be seen for 80 GeV/c p+p data. For p+p collisions at RHIC energies, the STAR experiment also measured lower K^{*0} mass, especially at lower transverse momenta. The high-statistics NA61/SHINE data from p+p interactions at p_{beam} = 158 GeV/c, allowed to determine m_{K^*} and Γ_{K^*} parameters with much higher precision than other available results.

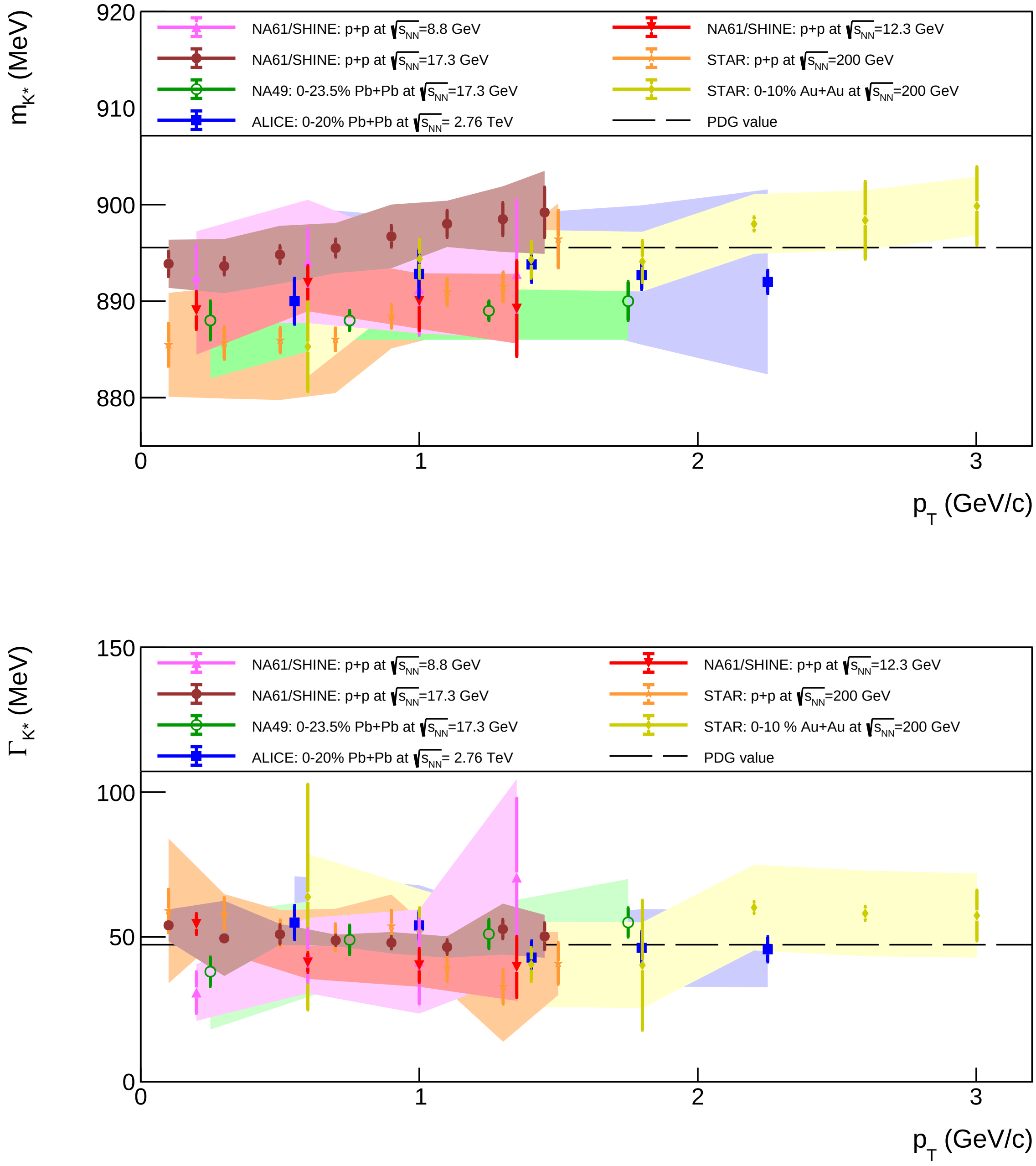

Figure 6.1: The mass and width of $K^*(892)^0$ (or K^{*0}) meson peak as a function of transverse momentum obtained by NA61/SHINE, NA49 [47], ALICE [52], and STAR [48]. For ALICE and STAR the averaged (K^{*0}) measurements of $K^*(892)^0$ and $\overline{K^*}(892)^0$ are shown. The horizontal lines represent PDG values [11].

6.2 Comparison of rapidity spectra and yields with NA49 and EPOS 1.99

The obtained rapidity distributions and mean multiplicities of $K^*(892)^0$ mesons were compared to those predicted by the microscopic model of hadron production EPOS 1.99 [90] for p+p interactions at $p_{beam} = 40$–158 GeV/c. The results are shown in Fig. 6.2 and the numerical values of $\langle K^*(892)^0 \rangle$ are given in Table 6.1. It is visible that the EPOS 1.99 model overestimates $K^*(892)^0$ production in inelastic p+p collisions at SPS energies.

The NA49 experiment studied the $K^*(892)^0$ mesons in p+p interactions at $p_{beam} = 158$ GeV/c [47, 97]. The results obtained from NA49 are also shown in Table 6.1. Instead of analysing in separate p_T bins, as in NA61/SHINE, the NA49 experiment used one wide p_T bin ($0 < p_T < 1.5$ GeV/c). It was due to much smaller statistics (about 52.5M interaction trigger events in NA61/SHINE compared to 2.5M p+p events [97] analyzed by NA49). The mean multiplicity of $K^*(892)^0$ in NA49 was obtained as the integral under the Gaussian function in the range $-3 < y < 3$ fitted to the $\frac{dn}{dy}$ distribution [97]. Within the uncertainties shown, the result of both experiments are consistent.

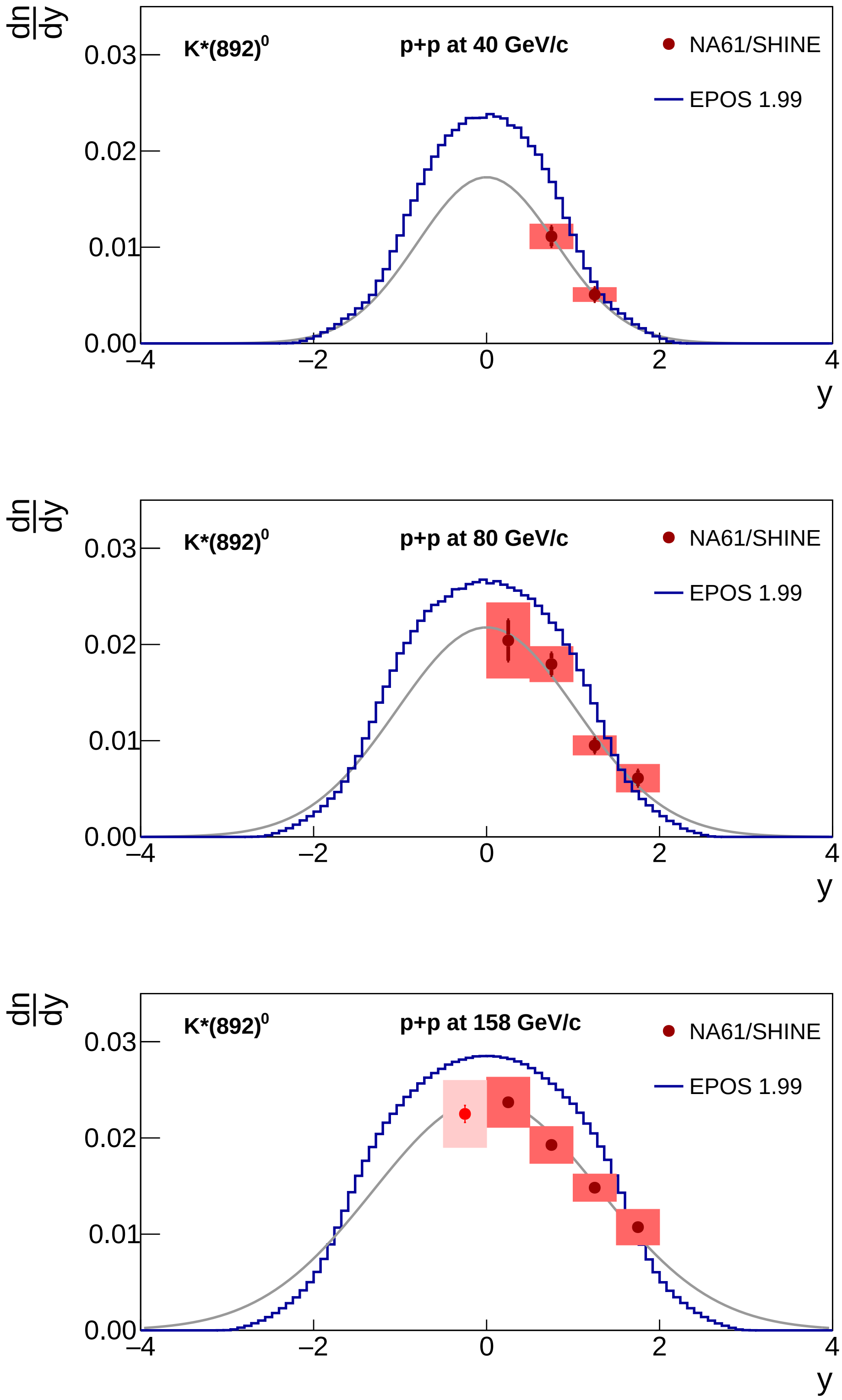

Figure 6.2: The comparison of $K^*(892)^0$ rapidity distribution from NA61/SHINE (points) and EPOS 1.99 model (blue histogram) for p+p interactions at 40 GeV/c (top plot), 80 GeV/c (middle plot), and 158 GeV/c (bottom plot). The fitted Gaussian functions to NA61/SHINE points (gray solid lines) are given by Eq. 5.6 (for 158 GeV/c the first point, with $y < 0$, was not included in the fit).

p+p at 40 GeV/c		
	$\langle K^*(892)^0 \rangle$	σ_y
NA61/SHINE, $\frac{dn}{dy}$ in wide p_T bin	$(34.4 \pm 1.2 \pm 3.8) \cdot 10^{-3}$	$0.768 \pm 0.29 \pm 0.082$
EPOS 1.99, no binning	$(46.67 \pm 0.03) \cdot 10^{-3}$	-
p+p at 80 GeV/c		
	$\langle K^*(892)^0 \rangle$	σ_y
NA61/SHINE, $\frac{dn}{dy}$ in wide p_T bin	$(57.1 \pm 1.9 \pm 5.3) \cdot 10^{-3}$	$1.037 \pm 0.059 \pm 0.065$
EPOS 1.99, no binning	$(67.02 \pm 0.04) \cdot 10^{-3}$	-
p+p at 158 GeV/c		
	$\langle K^*(892)^0 \rangle$	σ_y
NA61/SHINE, p_T-integrated and extrapolated $\frac{dn}{dy}$	$(78.44 \pm 0.38 \pm 6.0) \cdot 10^{-3}$	$1.31 \pm 0.15 \pm 0.09$
NA49, $\frac{dn}{dy}$ in wide p_T bin [47]	$(74.1 \pm 1.5 \pm 6.7) \cdot 10^{-3}$	$1.17 \pm 0.03 \pm 0.07$
EPOS 1.99, no binning	$(87.82 \pm 0.06) \cdot 10^{-3}$	-

Table 6.1: The mean multiplicities of $K^*(892)^0$ mesons and the widths of the rapidity distributions σ_y obtained from $\frac{dn}{dy}$ distributions (see the text for details). The results are presented for NA61/SHINE, NA49 [47], and the EPOS 1.99 model. The first uncertainty is statistical, the second is systematic.

6.3 System size and energy dependencies of $\langle K^*(892)^0\rangle$ and predictions of HGM

The statistical Hadron Resonance Gas Models (HGM) allow to calculate particle multiplicities using as adjustable parameters the chemical freeze-out temperature T_{chem}, the baryochemical potential μ_B, strangeness saturation parameter γ_S, etc. The models assume statistical systems of non-interacting hadrons and resonances [29, 103, 104]. The HGM predictions of particle multiplicities are commonly compared with experimental results both in elementary and nucleus-nucleus collisions. In the following section, the measured NA61/SHINE $\langle K^*(892)^0\rangle$ multiplicities are compared with predictions of two HGM models described in Refs. [29, 104].

In Ref. [29], the HGM fits to particle yields were done for two different assumptions. The first one, called B, used the usual parametrization with γ_S (strangeness undersaturation was allowed). For p+p interactions, the multiplicities of multi-strange baryons, Ξ and Ω, were not included in the fit. The second version of the fit (called A) was realized by replacing the γ_S parameter by the mean number of strange quark pairs $\langle s\bar{s}\rangle$. In case of p+p collisions, the ϕ meson was not included in the fit. For p+p collisions, both the A and B fits were performed in the Canonical Ensemble (CE) [29]. The NA61/SHINE $\langle K^*(892)^0\rangle$ from inelastic p+p interactions at $p_{beam} = 158$ GeV/c was divided by HGM predictions for fit A and B, separately. The results were compared with the NA49 measurements at the same beam momentum for p+p interactions [47] as well as C+C, Si+Si, and Pb+Pb collisions [47] in Fig. 6.3. For C+C and Si+Si systems, the HGM multiplicities of $K^*(892)^0$ mesons were calculated using the S-Canonical Ensemble (SCE) with exact strangeness conservation and grand-canonical treatment of electric charge and baryon number [29]. In contrary to p+p system, all available particles (including ϕ, Ξ, and Ω) were used to perform HGM fits. The heaviest Pb+Pb system was described [29] by the Grand Canonical Ensemble (GCE). The Pb+Pb HGM fits were realized for all particles with exception of the $\Lambda(1520)$ baryon. The centrality of Pb+Pb collisions, used in the HGM fits, was 0-5%[1] but the NA49 multiplicity of $K^*(892)^0$ mesons was obtained for

[1] In NA49 and NA61/SHINE 0-x% (or x%) centrality means x% of nucleus-nucleus collisions with the lowest value of forward energy (energy of projectile spectators, it is projectile nucleons/nuclear fragments which did not participate in the collision).

the 0-23.5% most central Pb+Pb collisions. Therefore, the HGM Pb+Pb predictions had to be scaled by a factor 262/362 corresponding to the respective number of wounded nucleons (see Table 6.3).

The comparison of the NA49 and NA61/SHINE measurements with HGM predictions at 158 GeV/c (Fig. 6.3) shows increasing (with the system size) deviation between the obtained and predicted $K^*(892)^0$ multiplicities. For systems heavier than p+p, there is no significant difference between fit A and fit B. In turn, the $\langle K^*(892)^0 \rangle$ values for p+p collisions are very close to the HGM prediction only for fit A where the ϕ meson was not included in the fit.

Recently, the HGM predictions were also prepared using the Grand Canonical Ensemble formulation [104] for p+p collisions at $p_{beam} = 158$ GeV/c. The obtained ratios are presented as star (comparison with NA61/SHINE result) and cross (comparison with NA49 result) symbols in Fig. 6.3. Surprisingly, the GCE statistical model provides a good description of the multiplicity of $K^*(892)^0$ mesons in p+p interactions at $\sqrt{s_{NN}} = 17.3$ GeV.

In fact, in this already mentioned paper [104], the HGM fits were performed for p+p collisions at several SPS energies. The multiplicities of particles were calculated in the Canonical Ensemble including (fit called *with* ϕ) or excluding (fit called *no* ϕ) $\phi(1020)$ meson from the fit. For both fits, the $f_o(500)$ and $K^*(800)$ mesons were excluded. In Fig. 6.4, the mean multiplicities of $K^*(892)^0$ mesons, obtained from p+p interactions at $p_{beam} = 40$–158 GeV/c, were divided by the HGM predictions [104].

The HGM predictions from Ref. [104] confirm the earlier conclusion that p+p measurements can be described by the CE HGM only when the ϕ meson is excluded from the fit. The authors of Ref. [104] showed that the ϕ meson multiplicities in p+p collisions at the SPS energies cannot be well fitted using the CE formulation of the HGM. The χ^2/ndf value of the HGM fit increases by an order of magnitude when the ϕ meson yield is included.

The numerical values of the mean multiplicities of $K^*(892)^0$ mesons, measured by the NA61/SHINE experiment, and their corresponding HGM predictions are given in Table 6.2. In Figs. 6.3 and 6.4 the total uncertainty of $\langle K^*(892)^0 \rangle$ was calculated as the square root of the sum of squares of statistical and systematic uncertainties. The final uncertainty of the $\langle K^*(892)^0 \rangle / K^*(892)^0_{HGM}$ ratio, shown on the vertical axis, was calculated as the final uncertainty of $\langle K^*(892)^0 \rangle$ divided by $K^*(892)^0_{\mathrm{HGM}}$ value.

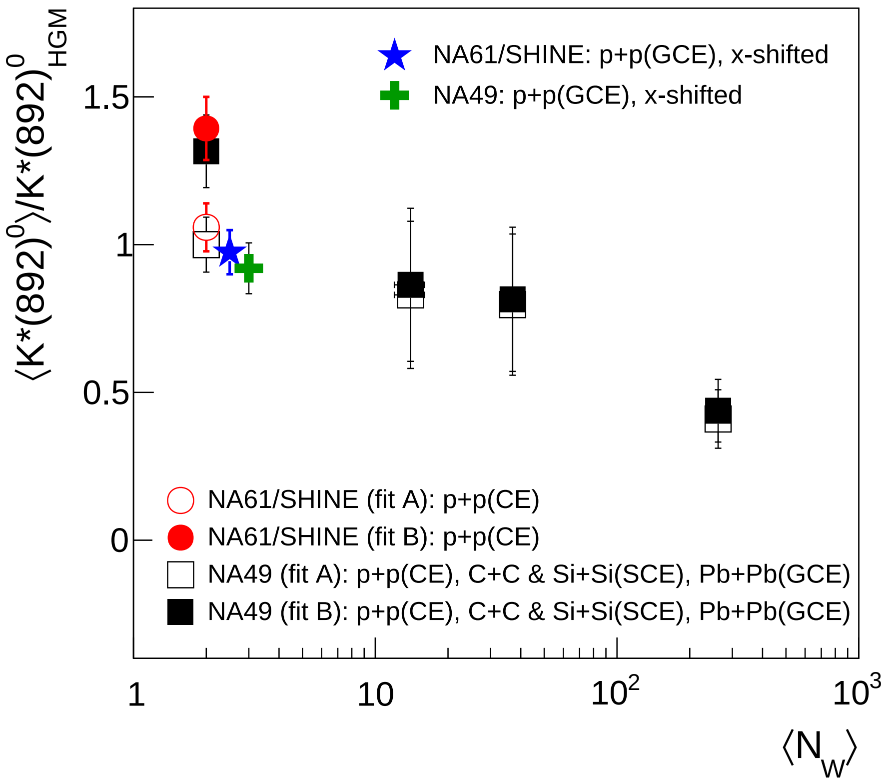

Figure 6.3: The $\langle K^*(892)^0 \rangle$ experimental values divided by the HGM predictions [29] for fit B (closed circle and closed squares) and fit A (open circle and open squares). The mean multiplicities of $K^*(892)^0$ mesons were obtained at $p_{beam} = 158$ GeV/c by the NA61/SHINE (in p+p collisions) and NA49 (p+p, C+C, Si+Si, and Pb+Pb [47] collisions) experiments. Closed star and cross symbols show the $\langle K^*(892)^0 \rangle$ divided by the HGM predictions for the Grand Canonical Ensemble formulation [104, 105]. N_W denotes the number of wounded nucleons taken from Ref. [47].

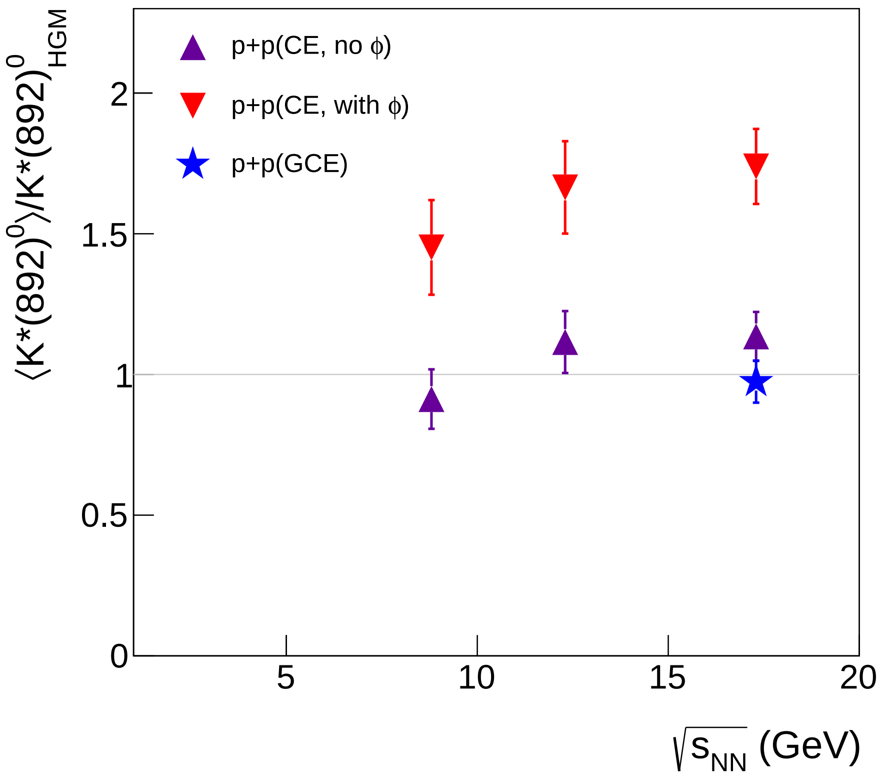

Figure 6.4: The $\langle K^*(892)^0 \rangle$ NA61/SHINE values, obtained from p+p interactions at p_{beam} = 40–158 GeV/c, divided by the HGM predictions [104] for the fit with ϕ included (upside down triangles) and the fit with ϕ excluded (triangles). Closed star shows the $\langle K^*(892)^0 \rangle$ divided by the HGM prediction for the Grand Canonical Ensemble [104, 105].

	$\langle K^*(892)^0 \rangle$ or $K^*(892)^0_{\mathrm{HGM}}$
p+p at 40 GeV/c	
NA61/SHINE, $\frac{dn}{dy}$ in wide p_T bin	$(34.4 \pm 1.2 \pm 3.8) \cdot 10^{-3}$
HGM, Canonical Ensemble (no ϕ) [104]	$37.7 \cdot 10^{-3}$
HGM, Canonical Ensemble (with ϕ) [104]	$23.7 \cdot 10^{-3}$
p+p at 80 GeV/c	
NA61/SHINE, $\frac{dn}{dy}$ in wide p_T bin	$(57.1 \pm 1.9 \pm 5.3) \cdot 10^{-3}$
HGM, Canonical Ensemble (no ϕ) [104]	$51.2 \cdot 10^{-3}$
HGM, Canonical Ensemble (with ϕ) [104]	$34.3 \cdot 10^{-3}$
p+p at 158 GeV/c	
NA61/SHINE, p_T-integrated and extrapolated $\frac{dn}{dy}$	$(78.44 \pm 0.38 \pm 6.0) \cdot 10^{-3}$
HGM, Canonical Ensemble, fit A (no ϕ) [29]	$74.1 \cdot 10^{-3}$
HGM, Canonical Ensemble, fit B (with ϕ) [29]	$56.3 \cdot 10^{-3}$
HGM, Canonical Ensemble (no ϕ) [104]	$69.1 \cdot 10^{-3}$
HGM, Canonical Ensemble (with ϕ) [104]	$45.1 \cdot 10^{-3}$
HGM, Grand Canonical Ensemble (with ϕ) [104, 105]	$80.5 \cdot 10^{-3}$

Table 6.2: The $K^*(892)^0$ mean multiplicities for inelastic p+p interactions at 40–158 GeV/c compared to the theoretical multiplicities of $K^*(892)^0$ mesons predicted by the HGM [29, 104, 105].

6.4 $\langle K^*(892)^0 \rangle$ over charged kaon ratios and time between freeze-outs

The time interval between chemical and kinetic freeze-outs in nucleus-nucleus collisions can be estimated by studying the ratios of the K^* to charged kaons. The K^* mesons have the same quark (anti-quark) content as K mesons, however, they have different masses and relative orientations of quark spins in comparison to K mesons. Thus, the $\langle K^*(892)^0 \rangle / \langle K^- \rangle$ and $\langle K^*(892)^0 \rangle / \langle K^+ \rangle$ ratios are considered as the least model dependent ratios for studying the K^* production properties as well as the freeze-out conditions.

The K^*/K ratios at the SPS, RHIC, and LHC energies are presented in Figs. 2.3, 2.4, 2.5, and 2.6. The system size dependence of the K^*/K ratio showed a strong decrease with increasing system size and/or multiplicity density (see Sec. 2.2 for a full list of references). The decrease of the K^*/K ratio with system size seems to be even stronger at SPS than at LHC and RHIC. A similar plot was prepared based on the NA49 and NA61/SHINE measurements at $p_{beam} = 158A$ GeV/c and is shown in Fig. 6.5. The numerical values are presented in Table 6.3.

Following Ref. [48], the time interval between chemical and kinetic freeze-outs can be estimated based on the NA61/SHINE $\langle K^*(892)^0 \rangle / \langle K^+ \rangle$ and $\langle K^*(892)^0 \rangle / \langle K^- \rangle$ yield ratios for p+p interactions and the corresponding ratios in central Pb+Pb collisions from the NA49 experiment at $p_{beam} = 158A$ GeV/c:

$$\frac{K^*}{K} \,|_{kinetic} = \frac{K^*}{K} \,|_{chemical} \cdot e^{-\frac{\Delta t}{\tau}}, \tag{6.1}$$

where:

- the ratio $\langle K^*(892)^0 \rangle / \langle K^{+/-} \rangle$ in inelastic p+p interactions can be treated as the one at chemical freeze-out,
- the ratio $\langle K^*(892)^0 \rangle / \langle K^{+/-} \rangle$ for central Pb+Pb (NA49) interactions can be used as the one at kinetic freeze-out,
- τ is the $K^*(892)^0$ lifetime of approximately 4.17 fm/c [11],
- Δt is the time interval between chemical and kinetic freeze-outs calculated in the $K^*(892)^0$ rest frame.

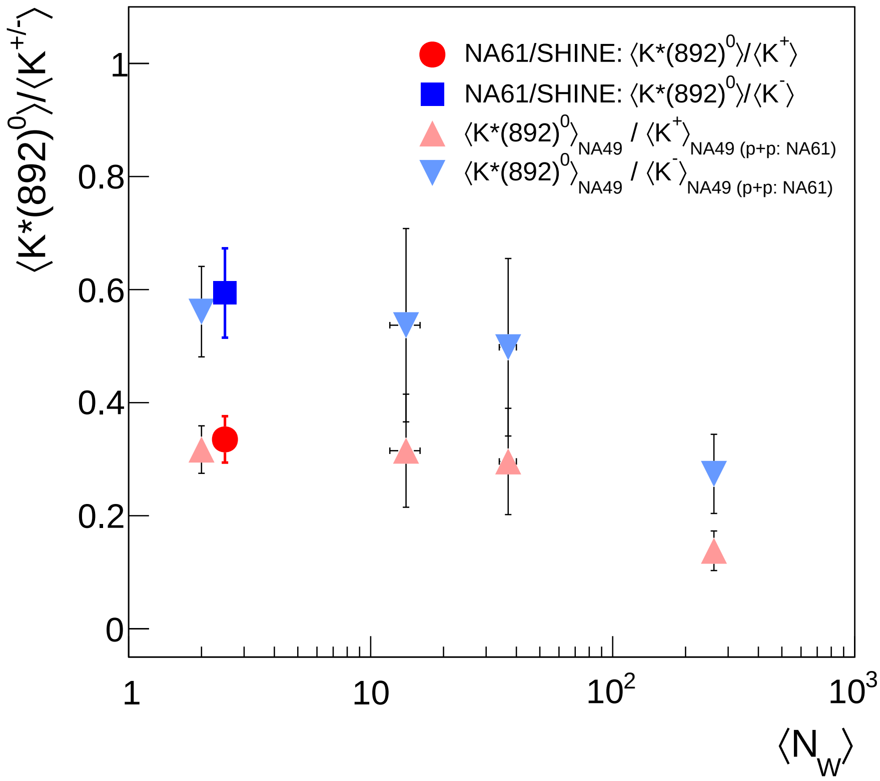

Figure 6.5: The $\langle K^{*}(892)^0\rangle/\langle K^+\rangle$ and $\langle K^{*}(892)^0\rangle/\langle K^-\rangle$ yield ratios as a function of the system size from p+p, C+C, Si+Si, and Pb+Pb collisions at 158A GeV/c. N_W denotes the number of wounded nucleons taken from Ref. [47]. The numerical values are given in Table 6.3. The NA61/SHINE points are shifted on the horizontal axis for better visibility.

	$\langle K^*(892)^0\rangle$	$\langle K^+\rangle$	$\langle K^-\rangle$	$\langle K^*(892)^0\rangle/\langle K^+\rangle$	$\langle K^*(892)^0\rangle/\langle K^-\rangle$
NA61/SHINE p+p, N_W=2	0.0784±0.0060	0.234±0.022 [35]	0.132±0.014 [35]	0.335±0.041	0.594±0.079
NA49 p+p, N_W=2	0.0741±0.0069 [47]	from NA61/SHINE	from NA61/SHINE	0.317±0.042	0.561±0.080
NA49 15.3% C+C, $\langle N_W\rangle$=14±2 [47]	0.80±0.24 [47]	2.54±0.25 [106]	1.49±0.16 [106]	0.31±0.10	0.54±0.17
NA49 12.2% Si+Si, $\langle N_W\rangle$=37±3 [47]	2.20±0.66 [47]	7.44±0.74 [106]	4.42±0.44 [106]	0.296±0.094	0.50±0.16
NA49 23.5% Pb+Pb, $\langle N_W\rangle$=262±6 [47]	10.3±2.5 [47]	74.5±5.1 (from scaling)	37.6±2.6 (from scaling)	0.138±0.035	0.274±0.070
NA49 5% Pb+Pb, $\langle N_W\rangle$=362±5 [56]	–	103.0±7.1 [56]	51.9±3.6 [56]	–	–

Table 6.3: The mean multiplicities of different particle species measured in nucleus-nucleus collisions at $p_{beam} = 158A$ GeV/c by the NA61/SHINE and NA49 experiments. The total uncertainties of $\langle K^*(892)^0\rangle$, $\langle K^+\rangle$, and $\langle K^-\rangle$ were calculated as the square roots of the sums of squares of statistical and systematic uncertainties. For NA49 p+p data, the $\langle K^+\rangle$ and $\langle K^-\rangle$ results include statistical uncertainties only ($\langle K^+\rangle = 0.2267 \pm 0.0006$ and $\langle K^-\rangle = 0.1303 \pm 0.0004$), whereas systematic uncertainties for total yields were not reported [57]. Therefore, NA61/SHINE $\langle K^+\rangle$ and $\langle K^-\rangle$ values were used in the $\langle K^*(892)^0\rangle/\langle K^+\rangle$ and $\langle K^*(892)^0\rangle/\langle K^-\rangle$ ratios. The numbers of $\langle K^+\rangle$ and $\langle K^-\rangle$ and their uncertainties for the 5% most central Pb+Pb collisions were multiplied by a factor 262/362 in order to estimate charged kaon multiplicities in the 23.5% most central Pb+Pb reactions.

The time interval between freeze-outs, in central Pb+Pb collisions at $158A$ GeV/c, was estimated as 3.7 ± 1.2 fm/c from the $\langle K^*(892)^0\rangle/\langle K^+\rangle$ ratio and 3.2 ± 1.2 fm/c from the $\langle K^*(892)^0\rangle/\langle K^-\rangle$ ratio. These calculations were made with an assumption that the losses of $K^*(892)^0$ mesons before kinetic freeze-out are due to rescattering effects only. The regeneration processes were neglected. The obtained time intervals between freeze-outs correspond to 23.5% of the most central Pb+Pb interactions. The similar values can be obtained using 5% of the most central events.

The calculated time between freeze-outs, in the $K^*(892)^0$ rest frame, can be transformed to the collision center-of-mass reference system using the multiplicative Lorentz factor [55]:

$$\gamma \approx \sqrt{1 + (\langle p_T\rangle/m_0 c)^2}, \tag{6.2}$$

where $\langle p_T\rangle$ can be used as an approximation for $K^*(892)^0$ total momentum for the measurements at mid-rapidity.

The NA49 transverse momentum spectrum for 23.5% most central Pb+Pb collisions was prepared in the rapidity range $0.43 < y < 1.78$ [47]. The mean transverse momentum can be obtained from the fitted exponential function in the range $0 < p_T < 4$ GeV/c. The average transverse momentum of $K^*(892)^0$ mesons was found to be 0.908 GeV/c, therefore, $\gamma \approx 1.42$. Finally, the Lorentz boosted time interval between chemical and kinetic freeze-outs can be estimated as 5.3 fm/c for the $\langle K^*(892)^0\rangle/\langle K^+\rangle$ ratio or 4.6 fm/c for the $\langle K^*(892)^0\rangle/\langle K^-\rangle$ ratio.

The time interval between freeze-outs can be calculated in the same way for the published RHIC ($\sqrt{s_{NN}} = 200$ GeV) and LHC ($\sqrt{s_{NN}} = 2760$ GeV) data. The STAR experiment at RHIC obtained the K^{*0}/K^- ratio for the 10% most central Au+Au collisions (0.20 ± 0.04) and for p+p interactions (0.34 ± 0.05) [50]. Based on these values, the time interval between chemical and kinetic freeze-outs, calculated in the K^{*0} rest frame, is equal to 2.2 ± 1.0 fm/c. Based on the average transverse momentum of K^{*0} mesons in Au+Au collisions at mid-rapidity ($|y| < 0.5$), equal 1.09 GeV/c [50], the Lorentz factor can be estimated as $\gamma \approx 1.57$. Therefore, the time interval between freeze-outs, in the collision center-of-mass reference system, can be estimated as 3.5 fm/c. This value is smaller than the ones obtained at SPS.

The ALICE experiment at LHC obtained the K^{*0}/K^- ratio for the 5% most central

	p+p at 40 GeV/c	p+p at 80 GeV/c
$\langle K^*(892)^0 \rangle$	0.0344 ± 0.0040	0.0571 ± 0.0056
$\langle K^+ \rangle$ [35]	0.170 ± 0.025	0.201 ± 0.014
$\langle K^- \rangle$ [35]	0.0840 ± 0.0067	0.0950 ± 0.0064
$\langle K^*(892)^0 \rangle / \langle K^+ \rangle$	0.202 ± 0.038	0.284 ± 0.034
$\langle K^*(892)^0 \rangle / \langle K^- \rangle$	0.410 ± 0.058	0.601 ± 0.072

Table 6.4: The mean multiplicities of different particle species measured in p+p interactions at $p_{beam} = 40$ and 80 GeV/c by the NA61/SHINE experiment. The total uncertainties of $\langle K^*(892)^0 \rangle$, $\langle K^+ \rangle$, and $\langle K^- \rangle$ were calculated as the square roots of the sums of squares of statistical and systematic uncertainties.

Pb+Pb collisions (0.180 ± 0.027) and for p+p interactions (0.307 ± 0.043) [53]. Therefore, the time interval between chemical and kinetic freeze-outs, calculated in the K^{*0} rest frame, is equal to 2.2 ± 0.9 fm/c. Based on the average transverse momentum of K^{*0} mesons in Pb+Pb collisions at mid-rapidity ($|y| < 0.5$), equal 1.310 GeV/c [53], the Lorentz factor can be estimated as $\gamma \approx 1.77$. Thus, the time interval between freeze-outs, in the collision center-of-mass reference system, can be estimated as 3.9 fm/c.

Both time intervals, from RHIC and LHC measurements, are smaller than the ones obtained at SPS. It can imply that the lifetime of the hadronic fireball, created in central heavy ion collisions, is longer at SPS than at RHIC and LHC energies. However, the calculations of these times were performed with an assumption that there are no regeneration processes of K^{*0} mesons before kinetic freeze-out. In fact, the K^{*0} regeneration processes may occur for all energies, so the obtained time interval values should be considered as lower limits of the time between chemical and kinetic freeze-outs.

The $\langle K^*(892)^0 \rangle / \langle K^+ \rangle$ and $\langle K^*(892)^0 \rangle / \langle K^- \rangle$ ratios were also calculated for p+p interactions at $p_{beam} = 40$–80 GeV/c. The results are shown in Fig. 6.6 and the numerical values are given in Table 6.4. The $K^*(892)^0$ mesons were not studied in Pb+Pb collisions at $p_{beam} = 40A$ and $80A$ GeV/c, but the calculated $\langle K^*(892)^0 \rangle / \langle K^+ \rangle$ and $\langle K^*(892)^0 \rangle / \langle K^- \rangle$ ratios from the NA61/SHINE p+p data can be used in future to calculate time intervals between freeze-outs for lower SPS energies.

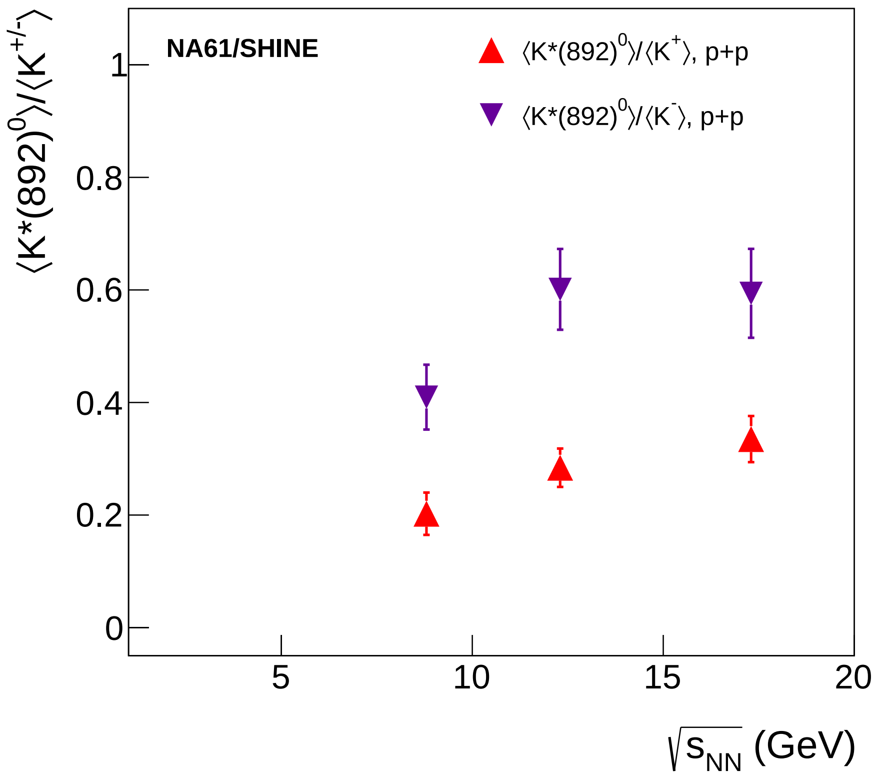

Figure 6.6: The $\langle K^*(892)^0\rangle/\langle K^+\rangle$ and $\langle K^*(892)^0\rangle/\langle K^-\rangle$ yield ratios obtained from p+p collisions at p_{beam} = 40–158 GeV/c. The numerical values are given in Table 6.4 (p+p at 40 and 80 GeV/c) and Table 6.3 (NA61/SHINE p+p data at 158 GeV/c).

Chapter 7

Summary and conclusions

In this thesis, the $K^*(892)^0$ mesons were studied via its $K^+\pi^-$ decay channel in inelastic p+p collisions at beam momenta 40–158 GeV/c measured by the NA61/SHINE experiment located at the CERN SPS. For the first time, the *template* method was used to extract the raw numbers of $K^*(892)^0$ mesons. In this method, the background is described by two templates. The first one represents the uncorrelated pairs created using the mixing event technique. The second template represents the correlated pairs coming from resonance decays, with exception of $K^*(892^0)$, based on the EPOS 1.99 model. This method gave a better background description, in invariant mass spectra of $K^+\pi^-$ candidates, than the *standard* method which relies on mixed events only.

The statistics of NA61/SHINE collected data for p+p interactions at $p_{beam} = 40$ and 80 GeV/c was too small to prepare the double-differential spectra. Therefore, the $K^*(892)^0$ spectra were prepared in the wide transverse momentum (or rapidity) bin, similarly to the NA49 studies. The prepared spectra allowed to determine mean multiplicities of $K^*(892)^0$ mesons (in $0 < p_T < 1.5$ GeV/c) as well as inverse slope parameters of transverse momentum spectra.

The high-statistics NA61/SHINE data for p+p interactions at $p_{beam} = 158$ GeV/c (52.5M events selected by the interaction trigger) allowed to obtain double-differential transverse momentum and rapidity spectra of $K^*(892)^0$ mesons. The full phase-space mean multiplicity of $K^*(892)^0$ mesons was obtained from the p_T-integrated and extrapolated rapidity distribution. The result agrees with the NA49 measurement obtained for the same system and beam momentum.

The prepared invariant mass spectra of $K^+\pi^-$ candidates allow to obtain the masses and widths of the $K^*(892)^0$ mesons peaks from the fit parameters. These values were studied for different transverse momentum bins. Within total uncertainties, for all three energies the widths of $K^*(892)^0$ mesons are consistent with the PDG value ($\Gamma_0 = 47.3$ MeV). The obtained masses of $K^*(892)^0$ mesons for p+p collisions at 40 GeV/c are also in agreement with the PDG value ($m_0 = 895.55$ MeV). However, the m_{K^*} for p+p collisions at 80 GeV/c are slightly below PDG. The mass of $K^*(892)^0$ mesons for p+p collisions at 158 GeV/c slightly increases with transverse momentum, however, within uncertainties these values are also consistent with PDG.

The obtained results on mean multiplicities of $K^*(892)^0$ mesons were compared with the values predicted by statistical Hadron Resonance Gas models in Canonical and Grand Canonical Ensemble formulations. The $\langle K^*(892)^0\rangle$ values can be described by the HGM CE predictions only when the ϕ meson is excluded from the fits. Surprisingly, the prediction prepared on the basis of the HGM GCE formulation gives a good description of $K^*(892)^0$ multiplicity in small p+p system at $\sqrt{s_{NN}} = 17.3$ GeV. The more predictions based on the HGM GCE formulation are needed for lower SPS energies ($\sqrt{s_{NN}} =$ 8.8–12.3 GeV).

According to the motivation of this thesis, the analysis of $K^*(892)^0$ was focused on the possibility of estimating the lower limit of the time interval between chemical and kinetic freeze-outs in nucleus-nucleus collisions. It was done using the $K^*(892)^0$ to charged kaons ratios from this analysis and from NA49 Pb+Pb data. The estimated lower limit of the time interval between freeze-outs at $\sqrt{s_{NN}} = 17.3$ GeV is larger than at RHIC and LHC what suggests that the lifetime of the hadronic fireball may be indeed longer at the SPS energies or the $K^*(892)^0$ regeneration effects start to play a significant role at higher collision energies. The $K^*(892)^0$ to charged kaons ratios were also studied for lower energies ($\sqrt{s_{NN}} = 8.8$ and 12.3 GeV) and, in future, they can be used to study the times between freeze-outs for those two energies. In principle, one may try to use Pb+Pb collisions at 40A GeV/c and 80A GeV/c beam momenta recorded by the NA49 experiment at the CERN SPS.

Bibliography

[1] D. Griffiths, “Introduction to elementary particles,” *Wiley-VCH*, 2004.

[2] E. Floratos, “Introduction to particle physics,” 3rd Annual Meeting Of Physics Greek Teachers, `https://indico.cern.ch/event/447008/contributions/1953687/attachments/1184942/1717323/ParticlePhysicsFOR_TEACHERS.pdf`, available at 10.01.2020.

[3] D. H. Perkins, “Introduction to high energy physics,” *University of Cambridge*, 2000.

[4] M. Merk, I. van Vulpen, and W. Hulsbergen, “Particle Physics 1,” 2019. Lectures notes for course, `https://www.nikhef.nl/~wouterh/teaching/PP1/LectureNotes.pdf`, available at 10.01.2020.

[5] F. Wilczek, “The Cosmic Asymmetry Between Matter And Antimatter,” *Sci. Am.*, vol. 243N6, pp. 60–68, 1980.

[6] L. Nanni, “Fermi’s theory of beta decay: a first attempt at electroweak unification,” *Adv. Stud. Theor. Phys.*, vol. 13, no. 5-8, pp. 281–293, 2019.

[7] M. Gell-Mann and Y. Ne’eman, “The Eightfold way: a review with a collection of reprints,” *W.A. Benjamin*, 1964.

[8] F. Halzen and A. D. Martin, “Quarks and leptons: An introductory course in modern particle physics,” *John Wiley & Sons*, 1984.

[9] `https://en.wikipedia.org/wiki/Baryon`, available at 10.01.2020.

[10] D. Lincoln ”The Quantum Frontier: the Large Hadron Collider,”, *The Johns Hopkins University Press*, 2009.

[11] M. Tanabashi *et al.*, “Review of Particle Physics,” *Phys. Rev.*, vol. D98, no. 3, p. 030001, 2018.

[12] G. Fantini, A. Gallo Rosso, F. Vissani, and V. Zema, “Introduction to the Formalism of Neutrino Oscillations,” *Adv. Ser. Direct. High Energy Phys.*, vol. 28, pp. 37–119, 2018.

[13] K. Grebieszkow, “Lectures on heavy ion physics,” 2019. `http://www.if.pw.edu.pl/~kperl/HIP/`.

[14] D. J. Gross and F. Wilczek, “Ultraviolet Behavior of Nonabelian Gauge Theories,” *Phys. Rev. Lett.*, vol. 30, pp. 1343–1346, 1973.

[15] G. Altarelli, “The QCD Running Coupling and its Measurement,” *PoS*, vol. Corfu2012, p. 002, 2013.

[16] M. Botje, “Lecture notes particle physics ii, quantum chromo dynamics, asymptotic freedom,” 2013. `https://www.nikhef.nl/~h24/qcdcourse/section-6.pdf`, available 10.01.2020.

[17] E. V. Shuryak, “Quark-Gluon Plasma and Hadronic Production of Leptons, Photons and Psions,” *Phys. Lett.*, vol. B78, p. 150, 1978.

[18] E. V. Shuryak, “Quantum Chromodynamics and the Theory of Superdense Matter,” *Phys. Rept.*, vol. 61, pp. 71–158, 1980.

[19] R. Sahoo, “Possible Formation of QGP-droplets in Proton-Proton Collisions at the CERN Large Hadron Collider,” *AAPPS Bull.*, vol. 29, no. 4, pp. 16–21, 2019.

[20] J. C. Collins and M. J. Perry, “Superdense Matter: Neutrons Or Asymptotically Free Quarks?,” *Phys. Rev. Lett.*, vol. 34, p. 1353, 1975.

[21] A. Bazavov *et al.* [HotQCD Collaboration], “Chiral crossover in QCD at zero and non-zero chemical potentials,” *Phys. Lett. B*, vol. 795, pp. 15–21, 2019.

[22] E. Iancu, “QCD in heavy ion collisions,” in *Proceedings, 2011 European School of High-Energy Physics (ESHEP 2011): Cheile Gradistei, Romania, September 7-20, 2011*, pp. 197–266, 2014. arXiv:1205.0579.

[23] H. Sazdjian, “Introduction to chiral symmetry in QCD,” *EPJ Web Conf.*, vol. 137, p. 02001, 2017.

[24] K. Fukushima, “Chiral Symmetry and Heavy-Ion Collisions,” *J. Phys.*, vol. G35, p. 104020, 2008.

[25] P. Castorina, R. V. Gavai, and H. Satz, “The QCD Phase Structure at High Baryon Density,” *Eur. Phys. J.*, vol. C69, pp. 169–178, 2010.

[26] S. Borsanyi, “Thermodynamics of the QCD transition from lattice,” *Nucl. Phys.*, vol. A904-905, pp. 270c–277c, 2013.

[27] M. A. Stephanov, K. Rajagopal, and E. V. Shuryak, “Event-by-event fluctuations in heavy ion collisions and the QCD critical point,” *Phys. Rev. D*, vol. 60, p. 114028, 1999.

[28] R. Stock, “The QCD Phase Diagram: Expectations and Challenges,” *PoS*, vol. CPOD2009, p. 001, 2009.

[29] F. Becattini, J. Manninen, and M. Gaździcki, “Energy and system size dependence of chemical freeze-out in relativistic nuclear collisions,” *Phys. Rev.*, vol. C73, p. 044905, 2006.

[30] A. Dainese, “Future facilities and experiments,” *the XXVIIIth International Conference on Ultra-relativistic Nucleus-Nucleus Collisions.* `https://indico.cern.ch/event/792436/contributions/3570592/attachments/1942038/3220505/Dainese_QM19_grey.pdf`, available at 10.01.2020.

[31] M. Gaździcki and M. I. Gorenstein, “On the early stage of nucleus-nucleus collisions,” *Acta Phys. Polon.*, vol. B30, p. 2705, 1999.

[32] M. Gaździcki, M. I. Gorenstein, and P. Seyboth, “Recent Developments in the Study of Deconfinement in Nucleus-Nucleus Collisions,” *Int. J. Mod. Phys.*, vol. E23, p. 1430008, 2014.

[33] C. Alt *et al.* [NA49 Collaboration], “Pion and kaon production in central Pb+Pb collisions at 20A and 30A GeV: Evidence for the onset of deconfinement,” *Phys. Rev.*, vol. C77, p. 024903, 2008.

[34] A. Aduszkiewicz [for NA61/SHINE Collaboration], "Recent results from NA61/SHINE," *Nucl. Phys.*, vol. A967, pp. 35–42, 2017.

[35] A. Aduszkiewicz *et al.* [NA61/SHINE Collaboration], "Measurements of $\pi^{\pm}$, $K^{\pm}$, p and $\bar{p}$ spectra in proton-proton interactions at 20, 31, 40, 80 and 158 GeV/c with the NA61/SHINE spectrometer at the CERN SPS," *Eur. Phys. J.*, vol. C77, no. 10, p. 671, 2017.

[36] S. Puławski [for NA61/SHINE Collaboration], "Energy dependence of hadron spectra and multiplicities in p+p interactions," *PoS*, vol. CPOD2014, p. 010, 2015.

[37] S. Kowalski and S. Puławski [for NA61/SHINE Collaboration], "Recent results from NA61/SHINE," *Acta Phys. Polon.*, vol. B50, pp. 1765–1770, 2019.

[38] B. Martin and G. Shaw, "Particle physics," *Wiley*, 2017.

[39] S. Braibant, G. Giacomelli and M. Spurio, "Particles and Fundamental Interactions. An Introduction to Particle Physics," *Springer*, 2012.

[40] R. N. Cahn and G. Goldhaber, "The experimental foundations of particle physics," *Cambridge University Press*, 1989.

[41] M. Alston, L. W. Alvarez, P. Eberhard, M. L. Good, W. Graziano, H. K. Ticho, and S. G. Wojcicki, "Resonance in the $K\pi$ System," *Phys. Rev. Lett.*, vol. 6, pp. 300–302, 1961.

[42] M. H. Alston, L. W. Alvarez, P. Eberhard, M. L. Good, W. Graziano, H. K. Ticho, and S. G. Wojcicki, "Study of Resonances of the Sigma-pi System," *Phys. Rev. Lett.*, vol. 6, pp. 698–702, 1961.

[43] P. J. Davis, S. E. Derenzo, S. M. Flatte, M. Alston-Garnjost, G. R. Lynch, and F. T. Solmitz, "Unsplit $K^{*'}$s," *Phys. Rev. Lett.*, vol. 23, p. 1071, 1969.

[44] L. Alvarez, "Recent Developments In Particle Physics," in *Evolution of particle physics: A volume dedicated to Edoardo Amaldi in his sixtieth birthday. Elsevier Publishing Company*, pp. 1–49, 1970.

[45] C. Markert, G. Torrieri, and J. Rafelski, "Strange Hadron Resonances: Freeze-Out Probes in Heavy-Ion Collisions," *AIP Conf. Proc.*, vol. 631, no. 1, p. 533, 2002.

[46] C. Blume, "Is There Life After Hadronization? An Experimental Overview," *Acta Phys. Polon.*, vol. B43, pp. 577–586, 2012.

[47] T. Anticic *et al.* [NA49 Collaboration], "$K^*(892)^0$ and $\overline{K^*}(892)^0$ production in central Pb+Pb, Si+Si, C+C and inelastic p+p collisions at 158A GeV," *Phys. Rev.*, vol. C84, p. 064909, 2011.

[48] J. Adams *et al.* [STAR Collaboration], "$K(892)^*$ resonance production in Au+Au and p+p collisions at $\sqrt{s_{NN}} = 200$ GeV at STAR," *Phys. Rev.*, vol. C71, p. 064902, 2005.

[49] B. I. Abelev *et al.* [STAR Collaboration], "Hadronic resonance production in d+Au collisions at $\sqrt{s_{NN}} = 200$ GeV at RHIC," *Phys. Rev.*, vol. C78, p. 044906, 2008.

[50] M. M. Aggarwal *et al.* [STAR Collaboration], "K^{*0} production in Cu+Cu and Au+Au collisions at $\sqrt{s_{NN}} = 62.4$ GeV and 200 GeV," *Phys. Rev.*, vol. C84, p. 034909, 2011.

[51] M. Nasim [for STAR Collaboration], "Probing QCD matter via $K^{*0}(892)$ and $\phi(1020)$ resonance production at RHIC," in *18th International Conference on Strangeness in Quark Matter (SQM 2019) Bari, Italy, June 10-15, 2019*, arXiv:1911.02270.

[52] B. B. Abelev *et al.* [ALICE Collaboration], "$K^*(892)^0$ and $\phi(1020)$ production in Pb-Pb collisions at $\sqrt{s_{NN}} = 2.76$ TeV," *Phys. Rev.*, vol. C91, p. 024609, 2015.

[53] J. Adam *et al.* [ALICE Collaboration], "$K^*(892)^0$ and $\phi(1020)$ meson production at high transverse momentum in pp and Pb-Pb collisions at $\sqrt{s_{NN}} = 2.76$ TeV," *Phys. Rev.*, vol. C95, no. 6, p. 064606, 2017.

[54] D. S. D. Albuquerque [for ALICE Collaboration], "Hadronic resonances, strange and multi-strange particle production in Xe-Xe and Pb-Pb collisions with ALICE at the LHC," *Nucl. Phys.*, vol. A982, pp. 823–826, 2019.

[55] S. Acharya *et al.* [ALICE Collaboration], "Evidence of rescattering effect in Pb-Pb collisions at the LHC through production of $K^*(892)^0$ and $\phi(1020)$ mesons," *Phys. Lett.*, vol. B802, p. 135225, 2020.

[56] S. V. Afanasiev *et al.* [NA49 Collaboration], "Energy dependence of pion and kaon production in central Pb+Pb collisions," *Phys. Rev.*, vol. C66, p. 054902, 2002.

[57] T. Anticic *et al.* [NA49 Collaboration], "Inclusive production of charged kaons in p+p collisions at 158 GeV/c beam momentum and a new evaluation of the energy dependence of kaon production up to collider energies," *Eur. Phys. J.*, vol. C68, pp. 1–73, 2010.

[58] B. Abelev *et al.* [ALICE Collaboration], "Production of $K^*(892)^0$ and $\phi(1020)$ in pp collisions at $\sqrt{s} = 7$ TeV," *Eur. Phys. J.*, vol. C72, p. 2183, 2012.

[59] S. Acharya *et al.* [ALICE Collaboration], "$K^*(892)^0$ and $\phi(1020)$ production at midrapidity in pp collisions at $\sqrt{s} = 8$ TeV," arXiv:1910.14410.

[60] A. K. Dash [for ALICE Collaboration], "Multiplicity dependence of strangeness and hadronic resonance production in pp and p-Pb collisions with ALICE at the LHC," *Nucl. Phys.*, vol. A982, pp. 467–470, 2019.

[61] S. Acharya *et al.* [ALICE Collaboration], "Multiplicity dependence of $K^*(892)^0$ and $\phi(1020)$ production in pp collisions at $\sqrt{s} = 13$ TeV," arXiv:1910.14397.

[62] A. G. Knospe, private communication.

[63] A. Adare *et al.* [PHENIX Collaboration], "Measurement of K^0_S and K^{*0} in p+p, d+Au, and Cu+Cu collisions at $\sqrt{s_{NN}} = 200$ GeV," *Phys. Rev.*, vol. C90, no. 5, p. 054905, 2014.

[64] S. Acharya *et al.* [ALICE Collaboration], "Multiplicity dependence of light-flavor hadron production in pp collisions at $\sqrt{s} = 7$ TeV," *Phys. Rev.*, vol. C99, no. 2, p. 024906, 2019.

[65] M. Aguilar-Benitez *et al.*, "Inclusive particle production in 400 GeV/c pp interactions," *Z. Phys.*, vol. C50, pp. 405–426, 1991.

[66] D. Drijard *et al.* [Annecy(LAPP)-CERN-College de France-Dortmund-Heidelberg-Warsaw Collaboration], "Production of Vector and Tensor Mesons in Proton Proton Collisions at $\sqrt{s} = 52.5$ GeV," *Z. Phys.*, vol. C9, p. 293, 1981.

[67] T. Akesson *et al.* [Axial Field Spectrometer Collaboration], "Inclusive Vector - Meson Production in the Central Region of pp Collisions at $\sqrt{s} = 63$ GeV," *Nucl. Phys.*, vol. B203, p. 27, 1982. [Erratum: Nucl. Phys. B229, 541 (1983)].

[68] R. D. Pisarski, "Phenomenology of the Chiral Phase Transition," *Phys. Lett. B*, vol. 110, pp. 155–158, 1982.

[69] G. Brown and M. Rho, "Scaling effective Lagrangians in a dense medium," *Phys. Rev. Lett.*, vol. 66, pp. 2720–2723, 1991.

[70] G. Brown and M. Rho, "Chiral restoration in hot and/or dense matter," *Phys. Rept.*, vol. 269, pp. 333–380, 1996.

[71] A. Milov, "Light Vector Mesons," *Eur. Phys. J. C*, vol. 61, pp. 721–728, 2009.

[72] NA61/SHINE webpage, `http://shine.web.cern.ch/`, available at 10.01.2020.

[73] NA61/SHINE library of pictures.

[74] M. Unger [for NA61/SHINE Collaboration], "Hadron Production at Fixed Target Energies and Extensive Air Showers," *PoS*, vol. ICHEP2010, p. 449, 2010.

[75] C. Strabel [for NA61/SHINE Collaboration], "Hadro-production measurements for T2K by NA61/SHINE at the CERN SPS," in *25th Lake Louise Winter Institute: Celebrating 25 years (LLWI 2010) Lake Louise, Alberta, Canada, February 15-20, 2010*, arXiv:1006.0767.

[76] S. R. Johnson [for US-NA61 Collaboration], "Hadron production measurements for fermilab neutrino beams," *CERN-SPSC-2014-032*, 2014.

[77] D. Larsen [for NA61/SHINE Collaboration], "Upgrade of the NA61/SHINE Facility beyond 2020 for an Expanded Physics Programme," *Universe*, vol. 5, no. 1, p. 24, 2019.

[78] J. Brzychczyk [for NA61/SHINE Collaboration], "NA61/SHINE experiment at CERN SPS: Recent results, current status and perspectives," *J. Phys. Conf. Ser.*, vol. 1390, no. 1, p. 012022, 2019.

[79] N. Abgrall *et al.* [NA61/SHINE Collaboration], "NA61/SHINE facility at the CERN SPS: beams and detector system," *J. Inst.*, vol. 9, p. P06005, 2014.

[80] `https://commons.wikimedia.org/wiki/File:Cern-accelerator-complex.svg`, available at 10.01.2020.

[81] C. Bovet, R. Maleyran, L. Piemontese, A. Placci, and M. Placidi, "The Cedar Counters for Particle Identification in the SPS Secondary Beams: A Description and an Operation Manual," *CERN-82-13, CERN-YELLOW-82-13*, 1982.

[82] C. Strabel, "Evaluation of Particle Yields in 30 GeV Proton-Carbon Inelastic Interactions for Estimating the T2K Neutrino Flux," PhD thesis, Frankfurt University, *CERN-THESIS-2011-295*, 2011.

[83] A. Marcinek, "ϕ meson production in proton-proton collisions in the NA61/SHINE experiment at CERN SPS," PhD thesis, Jagiellonian University, *CERN-THESIS-2016-176*, 2016.

[84] N. Abgrall *et al.* [NA61/SHINE Collaboration], "Measurement of negatively charged pion spectra in inelastic p+p interactions at p_{lab} = 20, 31, 40, 80 and 158 GeV/c," *Eur. Phys. J.*, vol. C74, no. 3, p. 2794, 2014.

[85] A. Aduszkiewicz *et al.* [NA61/SHINE Collaboration], "Multiplicity and transverse momentum fluctuations in inelastic proton–proton interactions at the CERN Super Proton Synchrotron," *Eur. Phys. J.*, vol. C76, no. 11, p. 635, 2016.

[86] A. Aduszkiewicz *et al.* [NA61/SHINE Collaboration], "Two-particle correlations in azimuthal angle and pseudorapidity in inelastic p+p interactions at the CERN Super Proton Synchrotron," *Eur. Phys. J.*, vol. C77, no. 2, p. 59, 2017.

[87] A. Aduszkiewicz *et al.* [NA61/SHINE Collaboration], "Measurement of meson resonance production in π^-+C interactions at SPS energies," *Eur. Phys. J.*, vol. C77, no. 9, p. 626, 2017.

[88] S. Acharya *et al.* [ALICE Collaboration], "Production of the $\rho(770)^0$ meson in pp and Pb-Pb collisions at $\sqrt{s_{NN}} = 2.76$ TeV," *Phys. Rev.*, vol. C99, no. 6, p. 064901, 2019.

[89] P. Fachini [for STAR Collaboration], "ρ^0 Production in Cu+Cu Collisions at $\sqrt{s_{NN}}$ = 200 GeV and 62.4 GeV in STAR," *Nucl. Phys.*, vol. A830, pp. 837C–840C, 2009.

[90] K. Werner, F.-M. Liu, and T. Pierog, "Parton ladder splitting and the rapidity dependence of transverse momentum spectra in deuteron-gold collisions at RHIC," *Phys. Rev.*, vol. C74, p. 044902, 2006.

[91] Web page of CRMC package, `https://web.ikp.kit.edu/rulrich/crmc.html`, available at 10.01.2020.

[92] A. Ilnicka, "Comparison of hadron production in Monte-Carlo models and experimental data in p+p interactions at the SPS energies," MSc thesis, University of Warsaw, *CERN-THESIS-2013-427*, 2013.

[93] N. Abgrall *et al.* [NA61/SHINE Collaboration], "Measurements of cross sections and charged pion spectra in proton-carbon interactions at 31 GeV/c," *Phys. Rev.*, vol. C84, p. 034604, 2011.

[94] M. Unger [for NA61/SHINE Collaboration], "Results from NA61/SHINE," *EPJ Web Conf.*, vol. 52, p. 01009, 2013.

[95] R. Brun, F. Carminati, and S. Giani, "Geant detector description and simulation tool," *CERN-W5013*, 1994.

[96] Web page of ROOT package, `https://root.cern.ch/`, available at 10.01.2020.

[97] C. Hohne, "System-Size Dependence of Strangeness Production in Heavy-Ion Collisions at 158 AGeV," PhD thesis, University of Marburg, 2003, `https://edms5.cern.ch/document/816035/1`.

[98] A. Aduszkiewicz, "Energy dependence of negatively charged pion production in proton-proton interactions at the CERN SPS," PhD thesis, Warsaw University, *CERN-THESIS-2016-010*, 2016.

[99] T. Pierog, private communication.

[100] A. Aduszkiewicz *et al.* [NA61/SHINE Collaboration], "$K^*(892)^0$ meson production in inelastic p+p interactions at 158 GeV/c beam momentum measured by NA61/SHINE at the CERN SPS," arXiv:2001.05370, accepted by *Eur. Phys. J. C.*

[101] A. Tefelska [for NA61/SHINE Collaboration], "$K^*(892)^0$ production in p+p interactions from NA61/SHINE," in *18th International Conference on Strangeness in Quark Matter (SQM 2019) Bari, Italy, June 10-15, 2019*, arXiv:1911.01818.

[102] N. Abgrall *et al.* [NA61/SHINE Collaboration]. "Calibration and analysis of the 2007 data," *CERN-SPSC-2008-018, CERN-SPSC-SR-033*, 2008.

[103] V. V. Begun, M. Gaździcki, and M. I. Gorenstein, "Hadron-resonance gas at freeze-out: Reminder on the importance of repulsive interactions," *Phys. Rev.*, vol. C88, no. 2, p. 024902, 2013.

[104] V. V. Begun, V. Vovchenko, M. I. Gorenstein, and H. Stoecker, "Statistical hadron-gas treatment of systems created in proton-proton interactions at energies available at the CERN Super Proton Synchrotron," *Phys. Rev.*, vol. C98, no. 5, p. 054909, 2018.

[105] V. V. Begun, private communication.

[106] C. Alt *et al.* [NA49 Collaboration], "System-size dependence of strangeness production in nucleus-nucleus collisions at $\sqrt{s_{NN}} = 17.3$ GeV," *Phys. Rev. Lett.*, vol. 94, p. 052301, 2005.

List of Figures

List of Tables